Medical Physics Unit
McGill University, Montreal

Modulated Electron Radiation Therapy: An Investigation On Fast Beam Models and Radiation-Tolerant Solutions For Automated Motion Control Of A Few Leaf Electron Collimator

MSc Thesis

Pavlos Papaconstadopoulos

A thesis submitted to the Faculty of Graduate Studies and Research of McGill University in partial fulfillment of the requirements of the degree of Master of Science in Medical Radiation Physics

December 2011

Contents

List of Figures

List of Tables

Abstract

The purpose of this study was to address two specific issues related with the clinical application of Modulated Electron Radiation Therapy (MERT). The first was to investigate radiation-tolerant solutions for automated motion control of a Few Leaf Electron Collimator. Secondly, we implemented a fast, Monte Carlo-based, parameterized beam model for characterization of the electron beam in modulated deliveries. Two approaches were investigated for the implementation of a radiation-tolerant position feedback system: (i) the use of CMOS-based optical encoders protected by a prototype shield and (ii) the use of an analog device, such as a potentiometer, whose radiation tolerance is significantly higher. The two approaches were implemented and their performance tested. Results indicated that the optical encoders could not be safely used under radiation even with the presence of a shield. The analog position feedback system showed to be a viable solution. Future work will be focused towards the direction of implementing an analog position feedback system suitable for clinical use. The MC-based, parameterized beam model is based on the idea of deriving the scattered electron beam characteristics directly on the exit plane of the linear accelerator by the use of source scatter fluence kernels. Primary beam characteristics are derived by fast Monte Carlo simulations. The novelty of the method is that arbitrary rectangular fields can be recreated fast by superposition of the appropriate source kernels directly on the output plane. Depth, profile dose distributions and dose output, were derived for three field sizes ($8 \times 8, 2 \times 2$ and $2 \times 8\ cm^2$) and energies of 6 MeV and 20 MeV electron beams by the beam model and compared with full Monte Carlo simulations. The primary beam showed excellent agreement in all cases. Scattered particles agreed well for the larger field sizes of $8 \times 8\ cm^2$ and $2 \times 8\ cm^2$, while discrepancies were encountered for scattered particles for the smaller field size of $2 \times 2\ cm^2$. Sources of errors were identified and future work will focus on the improvement of the beam model.

Résumé

L'objectif primaire du projet est d'explorer des solutions de radiation dures pour le contrôle dynamique d'un collimateur d'électrons à lames dans le contexte de la radiothérapie par modulation d'électrons. De plus, un modèle de faisceau paramétrique basé sur la méthode Monte-Carlo (MC) a été implémenté pour la caractérisation du faisceau d'électrons durant les traitements modulés. Deux approches ont été étudiées pour le développement d'un système de positionnement à boucle rétroactif pour la radiation dure : (i) des encodeurs optique CMOS protégés par un bouclier prototype (ii) et des composantes analogues telles que les potentiomètres avec une tolérance de radiation relativement élevée. La comparaison des deux méthodes montre que les encodeurs optiques ne peuvent subir de radiation, même en présence d'un bouclier adapté. De ce fait, pour l'utilisation clinique, les solutions basées sur les composantes analogues sont plus prometteuses et doivent être étudiées en détails à l'avenir. Le model MC de faisceau paramétrique vise la caractérisation du faisceau d'électrons diffusé directement sur la surface de sortie de l'accélérateur linéaire à l'aide de noyaux de fluence pour la diffusion des sources. Les caractéristiques primaires du faisceau sont obtenues par les méthodes de MC rapides. La nouveauté de la méthode réside dans la reproduction rapide de champs rectangulaires par la superposition de noyaux appropriés directement sur la surface de sortie. Profondeur, distribution dosimétrique de profil, et résultat de dose, sont calculés à partir de trois champs ($8 \times 8\ cm^2$, $2 \times 2\ cm^2$, $2 \times 8\ cm^2$) et des énergies de 6 MeV et 20 MeV, et sont comparés aux simulations MC. Le faisceau primaire montre une excellente cohérence dans tout les cas. Les résultats pour les particules diffusées étaient consistants pour les deux méthodes dans le cas de champs plus larges ($8 \times 8\ cm^2$ et $2 \times 8\ cm^2$) alors que des divergences ont été notées pour les petits champs ($2 \times 2\ cm^2$). Les sources d'erreurs ont été identifiées et la recherche ultérieure visera donc l'amélioration du modèle de faisceau.

Acknowledgements

First of all, I would like to express my gratitude to my supervisor, Dr. Jan Seuntjens, for his guidance, support and constant encouragement through this year. His vision for the field of Medical Physics keeps inspiring me. I would also like to thank Pierre Leger for sharing his expertise in electronics and for the significant time he spent on this project solving technical problems. His attention to detail was admirable.

Many thanks to my colleagues in this project, Andrew Alexander and Tanner Connell, for patiently answering numerous of questions about Monte Carlo simulations and radiation physics. Their feedback was always highly appreciated and improved significantly the quality of this work. Special thanks to Margery Knewstubb and Tatjana Nisic for patiently and efficiently taking care of many bureaucratic issues.

I would also like to acknowledge: Robin VanGils, for manufacturing the build-up caps and protective shield for the FLEC, Eunah Chung, for assisting me with measurements and Tanner Connell, for revising and correcting the manuscript of this Thesis.

It would be a dismiss if I did not express my gratefulness to Dr. Erwin Podgorsak, for teaching me the critical importance and responsibility of being a medical physicist in our society and to Dr. Giorgos Tsipolitis, my former supervisor from E.M.Polytechneio of Athens, Greece, for introducing me to research and encouraging me to pursue graduate studies at McGill University.

I would like to acknowledge the Alexander S. Onassis Public Benefit Foundation in Greece for funding my MSc in Medical Radiation Physics.

Introduction

Radiation therapy is concerned with the application of ionizing radiation for the treatment of cancer. In recent years, we have witnessed a rapid and exciting development in photon beam radiation therapy. Complicated radiotherapy techniques and sophisticated technologies, such as intensity modulated radiation therapy, volumetric arc therapy and stereotactic radiosurgery are already being used on an everyday basis in the clinic. Even though these techniques lead to a high target conformity, they have also been associated with an increased risk of secondary cancers due to the delivery of low doses in relatively large volumes of healthy tissues. Electron beams could potentially provide an alternative solution to the problem, mainly in the case of superficial tumours. Electron beam dose distribution characteristics, such as high surface dose, limited range and low exit dose can result in an improved clinical outcome for breast and head & neck cases. However, the use of electron beams still lags behind that of photons, since the existing treatment modalities have not been developed in the same extent.

Modulated Electron Radiation Therapy (MERT) is a new treatment modality which can extend the usability of electron beams in the clinic. In this technique the electron beam energy and intensity are modulated to enhance the target conformity and reduce the dose to surrounding critical structures and to the whole body. The above qualities will reduce the risk of second malignancies, a matter of particular interest for children and young adults.

At McGill University, a Few Leaf Electron Collimator (FLEC) has been developed for delivery of intensity and energy modulated electron beams. The FLEC is composed of two pairs of copper leaves which can form any rectangular size opening up to $8 \times 8\ cm^2$. The FLEC can be placed below the lower scraper of an existing electron applicator and serves as the final beam collimation device before incident on the patient's surface. An optimization

algorithm has been implemented for determining the leaf sequences for optimum beam delivery. Furthermore, a Monte Carlo treatment planning system has been developed for accurate treatment planning.

The present research project is focused in further developing the above work towards the goal of the clinical implementation of this treatment modality. It consists of two independent areas of study: (1) Development and testing of a reliable, radiation-tolerant electronic feedback device for motion control of the FLEC. (2) Implementation of a Monte Carlo-based, parameterized, beam model code for fast and accurate derivation of the electron and photon beam characteristics incident on the patient's surface. The two areas of study are presented through this thesis independently from each other.

Reliable motion control is an essential requirement for any automated collimation system used in radiation therapy. The location, speed and acceleration of the collimator leaves have to be constantly monitored through a position feedback device in order to achieve accurate radiation delivery. Furthermore, this device should be radiation tolerant for our purposes. This requirement excludes many commercially available position feedback devices and demands special solutions.

The second component of this project is focused on implementing a parameterized beam model for accurate characterization of modulated electron beams. Currently, Monte Carlo (MC) simulations are being used for treatment planning with modulated electron beams. MC simulations have proven to reproduce very accurately the beam characteristics (fluence, energy and angular distribution) at the exit plane of a linear accelerator. This information is crucial for deriving dosimetrically accurate treatment plans. However, MC simulations are time consuming, especially when they are part of an optimization process. An alternative way to derive the beam characteristics is through a parameterized beam model. In a parameterized beam model the linear accelerator is being modeled as a number of significant radiation sources. By deriving basic characteristics of these sources such as fluence, energy and angular distribution, the radiation beam can be reconstructed directly before the patient's surface by sampling these distributions. This technique has been applied in the past for conventional electron beams and has shown to reduce the calculation time by a factor of 10 to 100. However, there have been limited studies in parameterized beam models for modulated electron radiotherapy.

It is expected that in the future, advanced electron radiotherapy will involve the implementation of intensity and energy modulation of electron beams through an automated electron collimator system. This work aims to contribute towards that direction by addressing existing issues in this new treatment modality and suggesting possible solutions. Furthermore, it is hoped that this study will re-new the interest of the community in electron beam therapy and improve our understanding of the electron beam characteristics.

Chapter 1

Theory

1.1 Electron beam therapy

1.1.1 General

Electron beams have been used in radiotherapy for more than 50 years now, constituting an important component of cancer treatment by radiation. Several machines have been used in the past for the production of megavoltage electron beams such as betatrons, microtrons and linear accelerators. In modern radiotherapy, the linear accelerator is most commonly used and can provide electron beams in an energy range from 4 to 25 MeV. Electron beams are currently used in approximately 5% of all the cancer cases treated with radiation, mainly focused in superficial tumours (depth of 5 cm or less). Cancer sites where the use of electron beams has proven to be beneficial include breast, skin and certain head and neck cases. Also, a special technique exist for the treatment of skin malignancies, such as mycosis fungoides, reffered to as total skin electron irradiation.

1.1.2 Electron interactions with matter and dosimetric quantities

Electrons are charged particles and therefore interact with matter by Coulomb forces. The interactions that may occur can be classified into two main categories:

- *Inelastic collisions*: electrons experience a change in their direction and energy loss.
- *Elastic collisions*: electrons experience a change in their direction but no energy loss.

Inelastic collisions are of significant importance in radiotherapy, since they result in energy absorbed in the medium. The energy losses by inelastic collisions can be classified to two categories:

- *Collisional losses*: electrons interact with atomic electrons, resulting in ionization or excitation of the atom.
- *Radiative losses*: electrons interact with the atomic nucleus, resulting in the production of X rays (*Bremsstrahlung* photons).

In order to understand and describe the nature of electron interactions with matter we need to define some fundamental physical quantities first.

Useful quantities

Stopping power is defined as the kinetic energy loss of a charged particle dE per unit of path length dx in a medium of density ρ and atomic number Z:

$$S = \frac{dE}{dx} \quad \left[\frac{MeV}{cm}\right] \tag{1.1}$$

Dividing the stopping power with the density of the medium results in the *mass stopping power*:

$$\frac{S}{\rho} = \frac{1}{\rho}\frac{dE}{dx} \quad \left[\frac{MeV\dot{c}m^2}{g}\right] \tag{1.2}$$

The mass stopping power can be further sub-divided into two terms depending on the type of energy loss:

- *Collisional mass stopping power* $(\frac{S}{\rho})_{col}$. Electrons lose their energy by collisional losses. The collisional mass stopping power is a function of the electron kinetic energy and electron density of the medium. Higher atomic number materials have smaller electron density and therefore electrons will experience less collisional losses.
- *Radiative mass stopping power* $(\frac{S}{\rho})_{rad}$. Electrons lose their energy by radiative losses. The radiative mass stopping power is approximately proportional to the electron energy and atomic number of the material. Higher atomic number materials will result in a higher rate of X ray production (*Bremsstrahlung* photons).

The total stopping power can be defined as:

$$\left(\frac{S}{\rho}\right)_{tot} = \left(\frac{S}{\rho}\right)_{col} + \left(\frac{S}{\rho}\right)_{rad} \tag{1.3}$$

Probably the most important quantity in medical physics is *absorbed dose*. *Absorbed dose* is defined as the expectation value of the energy imparted by ionizing radiation to a finite volume V of mass m:

$$D = \frac{dE}{dm} \tag{1.4}$$

Absorbed dose unit is the Gray defined as:

$$1 \quad Gy = 1 \quad \frac{J}{Kg}$$

The energy imparted in a volume V is a direct result of collisional losses of charged particles (electrons or positrons) in matter. Uncharged particles, such as photons, will deposit dose *indirectly* by tranfering energy to charged particles. Another fundamental quantity is *particle fluence*. *Particle fluence* is defined as the average number of particles dN crossing a sphere of cross-sectional area da:

$$\phi = \frac{dN}{da} \quad [cm^{-2}] \tag{1.5}$$

The choice of a sphere is crucial in the definition of particle fluence, since in that way the quantity remains independent of the incident angle (particles always pass perpendicularly the cross-section of a sphere). If the particle's incident angle should be taken into account, *planar fluence* should be used. *Planar fluence* is defined as the number of particles crossing a surface plane per unit area. Absorbed dose can be related to the collisional stopping power and particle fluence by the following approximate expression:

$$D = \phi \left(\frac{S}{\rho}\right) \tag{1.6}$$

1.1.3 Dose distributions and beam characteristics

Figure 1.1 shows the percent depth dose in water for electron beams (a) and photon beams (b). Percent depth dose (PDD) is defined as the percent dose at depth z on the beam's central axis normalized to the maximum dose on the central axis:

$$PDD(z) = 100 \cdot \frac{D_z}{D_{max}} \tag{1.7}$$

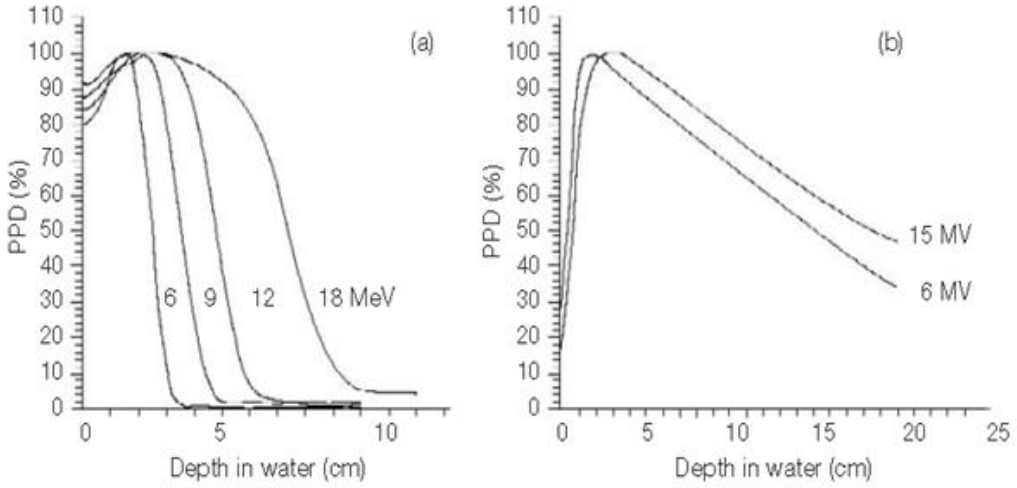

Figure 1.1: *Percent Depth Dose distributions (PDD) for* 10×10 cm^2 *field size and Source to Surface Distance (SSD) of 100 cm for: a) electron beams with energies 6 - 18 MeV and b) photon beams with energies 6 and 15 MeV (adapted from ref. [1])*

The following general observations can be made for the electron dose distribution characteristics:

- Electron beams exhibit a much higher surface dose than photons (75 % - 95 % of maximum dose compared to 10 % - 30 % for photon beams)
- The dose build-up from the surface to the point of maximum dose (z_{max}) is less pronounced than photons.
- The surface dose increases with energy for electron beams, while it decreases for photon beams.
- The depth of maximum dose does not follow a specific trend with energy.
- After z_{max} the dose drops more rapidly than for photons.
- The tail in the depth dose curve can be attributed to Bremsstrahlung photons produced in the accelerator head or patient body.

The above characteristics exhibit the main advantages of using electron beams for treating shallow tumors. Electron beams are capable of delivering high doses close to the surface, while sparing deep-seated normal tissues from excessive doses.

As an electron beam passes through matter, scattering events will occur easily due to Coulomb interactions with atomic electrons and nuclei. As a result an electron's original velocity will quickly be deflected on the lateral plane. Furthermore, secondary electrons may be produced by ionization events that will have enough energy to cause even further ionizations during their path ("hard" collisions). Therefore, electrons traversing a medium exhibit a "tree-like" trajectory, rather than a straight line.

The multiple scattering of electrons can be described by the mean square angle of scattering $\overline{\theta^2}$. The *mass angular scattering power* can then be defined, similarly to the stopping power definition:

$$\frac{T}{\rho} = \frac{1}{\rho}\frac{d\overline{\theta^2}}{dx} \tag{1.8}$$

The mass angular scattering power is approximately proportional to the square of the atomic number Z^2 and inverse proportional to the square of the kinetic energy $\frac{1}{E^2}$. Therefore, the variation of atomic numbers in heterogeneous materials will result in different electron scattering properties and consequently to a variation of absorbed dose in matter. This is a very important characteristic of electron beams since it results to hot or cold spots in the target. The phenomenon is more pronounced for lower energies and large variations of atomic numbers between different materials (such as between bone and soft tissue).

Electron range

As described previously, an electron will suffer multiple scattering events before all of its kinetic energy is lost. For each event a small or large fraction of the initial kinetic energy might be lost. If we assume that electrons lose small fractions of their energy at each interaction in a continuous manner, then an estimation of the electron range can be made by the use of the stopping power concept:

$$R_{CSDA} = \int_0^{E_0} [\frac{1}{S(E)/\rho}]dE \quad [\frac{g}{cm^2}] \tag{1.9}$$

The above quantity is referred to as the *Continuous Slowing Down Approximation* (CSDA) range. It should be noted that the CSDA range does not represent a valid indication of the depth of penetration, since electrons do not travel in straight lines in matter, or lose their energy in a continuous manner. Therefore the CSDA value will be an overestimation of the depth of penetration. Nevertheless, the quantity is very useful for quickly

calculating a range estimation, especially for shielding purposes. Other range concepts frequently used are:

- R_{90}, R_{80} *and* R_{50}: Depths on the PDD curve, where the PDD reaches values of 90%, 80% and 50% relative to the max dose (after z_{max}). R_{90} and R_{80} are commonly used by physicians for dose prescription purposes. A rough estimation of their values can be made by the following relationships as a function of the nominal electron beam energy:

$$R_{90} = \frac{E[MeV]}{3.2} \quad [cm] \tag{1.10}$$

$$R_{80} = \frac{E[MeV]}{2.8} \quad [cm] \tag{1.11}$$

  R_{50} is mainly used for calibration purposes.

- *Practical range* R_p: Defined as the depth at which the tangent plotted through the steepest section of the PDD curve (after z_{max}) meets the extrapolation line of the Bremsstrahlung tail.

Energy characterization

Characterizing the energy spectrum of a clinical electron beam on the exit plane of the linear accelerator or at depth z in water is a challenging problem. Several formulae have been proposed through the years, mainly based on calculated range values. Some of them are listed below:

- *Most probable energy at the phantom surface*:

$$E_{p,0} = 0.22 + 1.09R_p + 0.0025R_p^2, \tag{1.12}$$

  where $E_{p,0}$ is in MeV and R_p in cm.

- *Mean electron energy at the phantom surface*:

$$\overline{E}_0 = CR_{50} \tag{1.13}$$

  , where $C = 2.33MeV/cm$

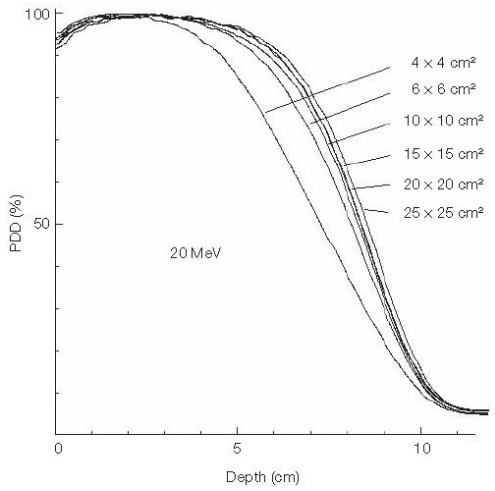

Figure 1.2: *PDDs for various fields for a 20 MeV electron beam at a SSD=100 cm . For electron field sizes larger than* 10×10 cm^2*, the PDD curves remain practically unchanged. Significant changes are observed for small fields.(adapted from ref. [1])*

- *Mean electron energy in depth z in a water phantom (Harder equation)*:

$$\overline{E}_z = \overline{E}_0(1 - \frac{z}{R_p}), \tag{1.14}$$

  where $\overline{E}_z$ is the mean energy in depth z and $\overline{E}_0$ is the mean energy on the phantom surface.

It should be noted that the above equations do not characterize accurately the energy spectrum. Monte Carlo simulations should be used for precise calculations.

1.1.4 Small electron fields and oblique incidence

If the distance between the central axis and the field edge is larger than the lateral range of the electrons, then *lateral scatter equilibrium* exist. Therefore, increasing the field size does not affect the PDD. *Lateral scatter equilibrium* can be defined, in a simple manner, as the condition where the number of electrons scattered from the edges of the field *in* the central axis is equal to those scatter from the central axis *out* of the field. As it can be seen in figure 1.2, for 20 MeV electron beams and fields larger than 10×10 cm^2, the condition holds and the PDDs remain unchanged. As the fields become smaller (less than 10×10 cm^2), the following observations can be made:

- The depth of maximum dose decreases with decreasing field size

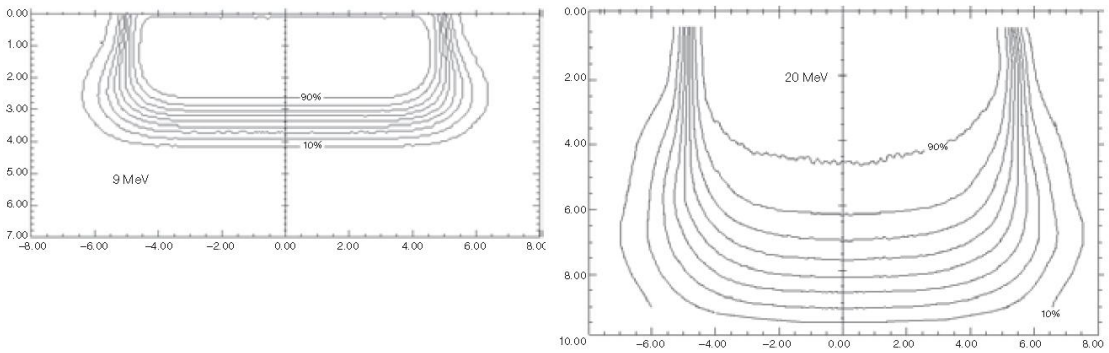

Figure 1.3: *Isodose distributions for 9 and 20 MeV electron beams. A bulging effect is observed for lower electron energies and low energy isodose lines. (adapted from ref. [1])*

- The surface dose increases with decreasing field size
- The R_p remains unchanged

Oblique incidence

For oblique beam incidences with angles exceeding 20 ° the following are observed:

- The depth of maximum dose decreases with increasing angle
- The surface dose increases with increasing angle
- For angles smaller than 60 °, the R_p remains unchanged. For angles larger than 60 °, the PDD curve losses its shape and the R_p definition losses its meaning.

1.1.5 Clinical aspects

Isodose distributions

Isodose distributions are lines connecting the points in a phantom or patient that receive the same amount of dose. Usually the normalization point is at z_{max}. For electron beams, the isodose lines tend to curve outwards especially closer to the field edge (Figure 1.3). The phenomenon is even more pronounced for low electron energies and low dose isodose lines. This bulging effect can be attributed to the increased electron scattering of low energy electrons. Consequently, the penumbra region for electrons is generally more pronounced than photons. This is an important issue to be addressed, especially when abutting electron fields are to be used.

Figure 1.4: *Electron applicator (field size:* $5 \times 5 \quad cm^2$*)*

Field shaping

Field shaping in electron radiation therapy is achieved by the use of specialized electron applicators (Figure 1.4). An electron applicator is usually composed by 2 or 3 scrapers and it is placed on the bottom of the linear accelerator head. The electron applicator serves as a field shaping device very close to the patient (approximately 5 cm from the skin). The scrapers are used to "cut-off" the air scattered electrons which would contribute to the penumbra region. Applicators exist for square field sizes of 5 x 5 cm^2 to 25 x 25 cm^2. In order to shape irregular field shapes according to the target, a customized cerrobend cut-out is inserted into the last scraper of the electron applicator.

Clinical use of electron beams

Electron beams are mainly used for the treatment of superficial tumours with the most common case being a boost treatment for breast cancer. Most commonly a single field size is applied, set at a SSD=100 cm, while the patient lies approximately 5 cm below the field shaping device. The patient surface needs to be as close as possible to the cerrobend cut-out, since electron air scattering will quickly alter the beam characteristics.

The dose prescribed by the physician is given at z_{max}, R_{80} or R_{90}. In any case the maximum dose to the patient should be also reported. The electron beam energy is selected so that the electron range (usually R_{80} or R_{90}) covers the distal margin of the tumour. Up to this moment, virtual electron beam treatment planning is not usually performed in

the clinic, even though accurate electron beam algorithms exist in all modern treatment planning systems.

Volume definitions and organs at risk

The following volume definitions quantify the target and critical structures for dose prescription and dose reporting purposes:

- *Gross tumour volume (GTV).* The GTV includes the visible extent and location of malignant growth, as it can be seen by diagnostic modalities and/or clinical examination.
- *Clinical target volume (CTV).* The CTV includes the GTV plus an additional margin to account for the existence of sub-clinical microscopic disease.
- *Internal target volume (ITV).* The ITV includes the CTV plus an additional margin to account for variations due to organ motions.
- *Planning target volume (PTV).* The PTV includes the ITV plus an additional margin to account for set-up uncertainties, machine tolerances and intra-treatment variations.

Organs at risk The organs at risk (OAR) are organs with no malignant disease present, but who may receive dose that reaches their radiation tolerance during the course of the treatment. In such case, the treatment plan has to be revised in order to protect these organs.

1.1.6 Electron beam dose calculations

There are two basic methods for electron beam dose calculations: the analytical method and the Monte Carlo method. In the following section, a brief description of each method is given.

Analytical method

Analytical methods usually refer to deterministic solutions to the electron transport problem which are applied to a *population* of particles rather than on a particle-by-particle

basis. The most commonly available analytical method for radiotherapy applications is the pencil beam algorithm. A pencil beam algorithm is based on the Fermi-Eyges charged particle scattering theory [2, 3]. According to this theory, if we assume a pencil beam of charged particles initially incident on a slab of a material, then the probability distribution for the location and direction of a particle as it exits the slab can be approximated by a Gaussian function. The theory assumes that there are no particle fluence loss and no large angular deflections, thus it is expected that the accuracy of the method is limited to low atomic number and density materials. For dose calculations in tissue, the total dose at a point can be calculated as the summation of the contribution at that point of each individual pencil beam. To account for tissue inhomogeneities, corrections can be applied that make use of stopping power ratios. The application of the Fermi-Eyges theory in radiotherapy has been described by Hogstrom [4]. Commercially available electron pencil beam algorithms have shown inaccuracies up to 10 % in inhomogeneous areas such as tissues including air cavities and bone structures [5]. However, these algorithms are still considered the only practical solution for performing electron dose calculations in the clinic due to their calculation speed.

Monte Carlo method

The most accurate way to calculate dose is by Monte Carlo (MC) simulations. The MC technique is based on the idea of random sampling the probability distributions that govern the physical processes that a particle can undergo as it traverses through a medium in order to attain values for quantities of interest. These quantities of interest may be, for example, the scattered angle or energy loss of the particle after an interaction. The sampling procedure is repeated for a statistically significant number of histories. Since the MC method mimics in a straightforward way the true physical interactions occurring in a material, the particle trajectory and dose deposition are predicted with very high accuracy. Furthermore, since we are tracking each individual particle we can derive accurate information about its history, such as the location that a secondary electron or bremsstrahlung photon was created.

For electron transport, it is not efficient to simulate each individual interaction that will occur along its path, since electrons undergo a very large number of interactions even

in short paths and low atomic number materials. Most of these interactions are elastic scattering events with nuclei or atomic electrons. Other interactions, which also occur frequently, are inelastic scattering events which can lead to the creation of low energy secondary electrons or bremsstrahlung photons. Events that result in the production of high energy secondary electrons or bremsstrahlung photons are not that frequent, but still important since they will result in large energy losses and/or angular deflections.

The most common method to make the electron transport calculation more efficient is the *condensed history* technique. In this technique, the path of each electron is broken into a series of discrete steps. In each step all the elastic scattering events are grouped together. Therefore one calculation is performed to account for the energy loss and the positional and angular deflection that the primary particle experienced along that step. Events that resulted in the production of secondary particles can be treated in two ways: (i) energy losses and angular deflections are grouped together for all events and the primary electron is not considered to be affected by the production of secondary particles (class I) and (ii) events that produced secondary particles above a treshold energy ("catastrophic" interactions) are treated independently and the rest of the interactions are grouped together (class II). Class II algorithms are more accurate than class I, even though in most applications these differences are negligable. A more detailed review of the Monte Carlo technique has been given by Rogers and Bielajew [7].

In radiotherapy, the MC method is usually applied in two independent steps:

- *MC simulation of the electron and photon transport in the linear accelerator.* The most commonly used codes for this part are the BEAMnrc/EGSnrc [8] and GEANT4 [9]. Both of these codes use the class II condensed history technique. In these codes, the treatment head of the linear accelerator is modeled faithfully according to its true physical representation. Specifically, each component is modeled based on the true geometrical and material information. Particles are transported through the treatment head and are collected on the specified exit plane. For each particle, the location, energy and direction among other parameters are saved in a file, commonly known as the *phase-space file*. The phase-space file can then be used as an input to the dose calculation engine.

- *MC simulation of electron and photon transport in the phantom/patient for dose calculations.* Using the derived phase-space file from the previous step as an input, a second MC simulation can start to derive the dose distribution in a patient. The patient's anatomical information is imported by CT data. Some of the most commonly used dose calculation codes for this part are the DOSXYZnrc code [10], the Voxel Monte Carlo code [11] and the Macro Monte Carlo (MMC) code [12].

The main drawback of the MC method has always been the computation time. In recent years the dose calculation time has significantly improved by the implementation of fast codes such as VMC and MMC. These codes have already been incorporated in several commercial treatment planning systems. However, explicit treatment head simulation with MC is still time consuming and therefore the MC method is not yet a realistic solution for routine use in the clinic. For this reason commercial clinical electron beam MC implementations have made use of *analytical, parameterized beam models* for deriving the phase-space information of the linear accelerator. Furthermore, since future advanced electron radiotherapy (such as energy and intensity modulated electron radiotherapy) will involve the delivery of a large number of beams with relatively small field sizes, it is expected that the need for fast electron beam models will be even greater. The implementation of *analytical, parameterized beam models* for deriving the phase-space information will be presented in section 1.4.

1.2 Modulated electron radiation therapy

1.2.1 General

In the last 15 years significant improvements have been made in radiotherapy with photon beams. Intensity modulated radiation therapy (IMRT) is a technique where the intensity of the photon beams are dynamically modulated by the use of a multileaf collimator in order to achieve highly conformal dose distributions to the target, while at the same time sparing healthy tissues and organs at risk (OAR) from receiving excessive doses. Furthermore, volumetric modulated arc therapy (VMAT) introduced an extra level of sophistication by allowing dynamic movements of the linac's gantry and couch during the delivery.

In these techniques the beam field sizes, gantry angles and couch position to be used for the delivery are selected according to an optimization procedure. The optimization algorithm, if described in a simple manner, determines the optimum settings that will minimize a *cost function*. The cost function is dependent on the weights of the various beam parameters (field size, gantry angle and couch position). The procedure starts with the planner setting criteria for the dose to the target and organs at risk. These criteria are restrictions to the system, such as maximum dose that can be received by a specific percent volume of an OAR. The optimization algorithm tries then to minimize the cost function and determines the weights of the parameters that will deliver a plan that respects the planner's criteria. The optimization procedure is not always successful and many times the planner will have to revise the restrictions. Areas where the planner did not set any criteria, are available for "dumping" dose. That means, the algorithm will preferably deliver as much dose as possible to these areas, since no restrictions were set, in order to respect the restrictions set to organs at risk and target. This dose "dumping" leads to an *increased volume* of healthy tissue receiving *low doses*. The above problem has been related with an increased risk of induced secondary cancers [13].

Modulated Electron Radiation Therapy (MERT) might contribute in the future to a possible solution to the above problem for specific cancer sites. The basic idea in MERT is the same as IMRT, only for electrons. The electron beam intensity and energy are modulated on the plane perpendicular to the central axis in order to deliver highly conformal plans to the target. The range of an electron is a function of its energy, therefore energy modulation leads to *depth dose conformity*, while intensity modulation will result in *lateral dose conformity*. As it can be seen in figure 1.1, electron beam characteristics exhibit a high surface dose, a rapid dose fall-off after z_{max} and a low exit dose. Therefore, the utilization of MERT for superficial tumors can potentially result in: (a) highly conformal plans (as in the case of IMRT), due to the energy and intensity modulation of the beam and (b) reduction of the low dose volume to healthy structures, due to the previously mentioned electron characteristics.

Energy and intensity modulation of electron beams has been used in the clinic for many years now, although not in an automated fashion. Modulation of the electron energy can be achieved by the use of a bolus, while modulation of electron beam intensity can be

achieved by the use of multiple abutted electron fields that are shaped by cerrobend cut-outs. However, the above techniques are time consuming and the accuracy of the delivery is questionable. Alternatively, an electron collimator can be used for modulating dynamically the energy and intensity of the electron beam in real time. In the following sections, existing and proposed techniques for modulation of electron beams will be presented. Different available prototypes of electron beam collimators will be presented for MERT, with special interest in the case of a Few Leaf Electron Collimator.

1.2.2 Bolus electron therapy

A bolus is a tissue equivalent material (usually wax) placed either in direct contact or close to the patient's surface. The goal is to provide energy degradation of the beam according to the PTV shape and fan beam direction. It's surface is specifically curved in such a way so that the R_{90} of the resulting electron dose distribution conforms to the PTV. Bolus can be manufactured with a thickness accuracy of 1 mm, which translates to an energy modulation step of approximately 0.2 MeV for megavoltage beams (considering that the stopping power in water is approximately constant to 2 MeV/cm). This energy resolution is the highest that can be achieved compared to any other energy modulation methods. However, two main drawbacks exist in the clinical use of bolus. First, significant time and effort is required for manufacturing a patient specific bolus. The time required can be estimated to 1 day, if specialized milling machines exist in the clinic [15]. Secondly, the homogeneity and the lateral conformity of the dose distribution in the PTV have proven to decrease significantly.

1.2.3 Segmented-field electron therapy

Segmented-field electron therapy can be defined as the use of multiple abutting electron fields, each with its own energy and weight, selected according to the PTV shape and depth. The varying field sizes can be defined by construction of different cerrobend cut-outs. The advantages of this approach are that there is no need for manufacturing a bolus and the lateral conformity is improved. However, this technique has proven to be difficult to deliver and usually the segmented fields do not match perfectly, resulting to overlapping penumbra

regions and hot and cold spots in the PTV.

1.2.4 Automated energy and intensity modulated electron therapy

Modulated electron radiation therapy can be defined as the utilization of multiple electron beams, each with it's own energy and intensity pattern. The main difference, compared to the previously mentioned techniques, is that in the case of MERT, an automated system is employed for the delivery of modulated electron beams. This requirement results in more efficient and accurate treatment deliveries than with the use of bolus and abutting fields. A disadvantage of MERT, compared to the use of a bolus, is that the available energy step is significantly larger depending on the restrictions of the machine employed (usually 3-5 MeV instead of 0.2 MeV).

Three possible approaches for the delivery of MERT have been proposed in the literature: (i) MERT using scanned electron beams, (ii) MERT using scattered electron beams collimated by a multileaf collimator and (iii) MERT using scattered electron beams collimated by a few leaf electron collimator.

Approach (i) has only been applied so far by using a Microtron Racetrack MM50 [17, 18]. The microtron MM50 is capable of producing pencil beam electrons up to energies of 50 MeV. The pencil beam is magnetically steered so that it can cover the whole PTV. All materials in the electron beam were minimized to reduce electron scattering as much as possible. These modifications include:

- He instead of air in the treatment head
- Thin exit window
- 31 cm of air between the treatment head and patient
- Scanned beams (no scattering foils)

Even though most of the above modifications could be applied to the linear accelerator as well, it would require re-design of the treatment machines by the manufacturers.

Approach (ii) can be applied by using the photon MLC to collimate electron beams as proposed by Klein et al [20] and Salguero et al [21, 22]. This approach could potentially

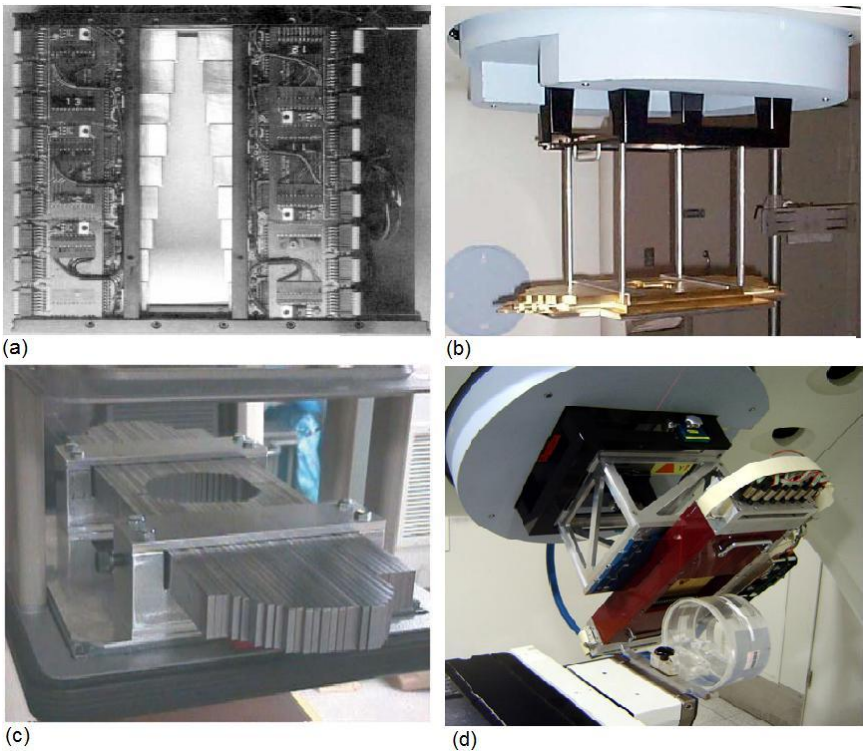

Figure 1.5: *Electron multileaf collimator prototypes: (a) Leavitt [25] , (b) Hogstrom [29] , (c) Ma [26] and (d) Gauer [34]*

be a practical way to implement a mixed IMRT-MERT therapy in the future. The main drawback of the method arises from the large air gap between the photon MLC and patient, which will lead to an unacceptable penumbra region. The problem can be minimized by replacing the air in the treatment head with helium [19] and/or reduce the SSD by moving the couch upstream. Klein et al [16] showed that a SSD of 70 cm results in clinical acceptable penumbra for Varian accelerators, while du Plessis et al [23] in a similar study showed that an SSD of 60 cm is necessary for Siemens accelerators. Lee et al [24] investigated the possibility of using a photon MLC for MERT with He in the treatment head and reduced SSD. He concluded that the penumbra width, even though reduced with these modifications, was still not better than using a dedicated electron MLC at the bottom of an existing applicator. In a standard air environment, a SSD of 65 cm would be needed in the case of using the photon MLC, in order to achieve similar results with an electron MLC. Furthermore, the use of an electron collimator showed to reproduce more faithfully irregular fields.

An alternative way to collimate electron beams is by implementing a dedicated electron

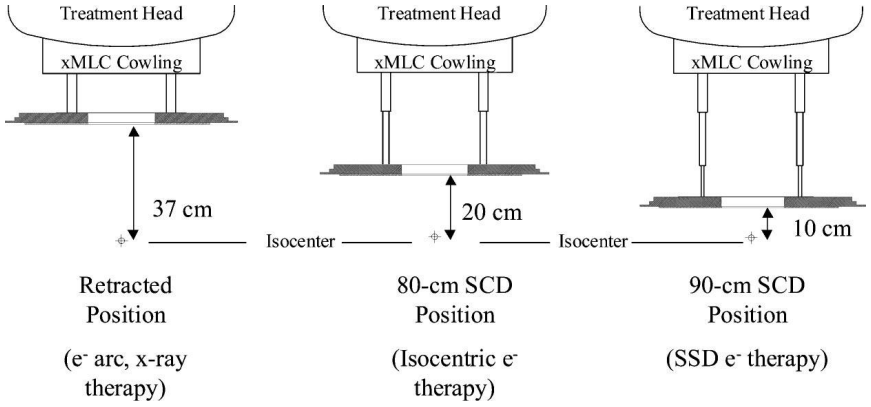

Figure 1.6: *Retractable electron applicator (adapted from ref. [29])*

multileaf collimator (eMLC). The eMLC can either be attached to the bottom of an existing electron applicator or to the bottom of a specialized applicator for delivery of modulated electron treatments. Up to present, various eMLC prototypes have been presented by Leavitt et al [25], Lee et al [24], Ma et al [26], Ravidran et al [27], Hogstrom et al [29], Gauer et al [28], Vatanen et al [33], Nassiri et al [30], Jin et al [31] and Eldib et al [32]. Figure 1.5 shows some of these prototypes.

A case of special interest was Leavitt's prototype (figure 1.5a) which was specifically designed for delivery of electron arc therapy. Modulated electron arc therapy is one of the possible future treatment modalities, where the gantry rotates during the delivery of the beam. Hogstrom et al [29] summarized the possible delivery techniques that could exist for MERT. He suggested the implementation of a retractable electron applicator for MERT (figure 1.6).

The proposed applicator could be set at a Source to Collimator Distance (SCD) of 90 cm (for fixed SSD treatments), 80 cm (for isocentric deliveries) and 63 cm (for electron arc therapies).

Gauer et al [28] summarized the technical requirements for a modern computer-controlled electron collimator to be used for MERT. The electron collimator should meet the following specifications:

- *The beam collimation should be computer-controlled to form sequenced electron beams with different shapes*
- *The source to collimator distance (SCD) should be such so that isocentric deliveries will be possible without the need for patient realignment during the gantry rotation*

- *The optimization of the SCD must cover the beam penumbra and the clinically required maximum field size*

- *The electron collimator must have a minimum weight to avoid gantry sagging*

Gauer et al [34] presented the dosimetric characteristics of their prototype eMLC. The eMLC is composed by 2×24 brass leaves with straight leaf ends (figure 1.5d) . To achieve isocentric deliveries, without patient realignments, the eMLC can be placed at 16 or 28 cm above the isocentre by the use of interchangeable holders. The eMLC weights 20 kg and the holder 10 kg. Compared to the use of a conventional electron applicator, the following were found for the use of the eMLC at a distance of 16 cm:

- The eMLC generates depth dose distributions with a larger build-up effect and lower surface dose.

- At lower energies, the beam penumbra is larger and the therapeutic field width smaller compared with those of a 10 x 10 cm^2 applicator.

- The isodose curves generated by the use of the eMLC exhibited a lower dose beyond the therapeutic range of 3-5% and a higher lateral dose beyond the therapeutic field width of 3-10%. The higher lateral dose can be attributed to the increased collimator - isocentre distance for isocentric deliveries, which results to increased electron scattering.

- Radiation leakage is increased, mainly due to the Bremsstrahlung photons additionally produced in the leaf material.

In their study they concluded that the accelerator jaws could potentially be used to reduce radiation leakage.

The collimation of electron beams by a multileaf collimator raises some practical questions. First, the total weight of the device might create problems with gantry sagging and field displacement. Considerable time might be required for inserting the device on the accelerator and for quality assurance procedures. Second, the presence of a large number of leaves increases the complexity of the delivery. Controlling the leaves in an efficient and safe way for clinical usage might be a challenge.

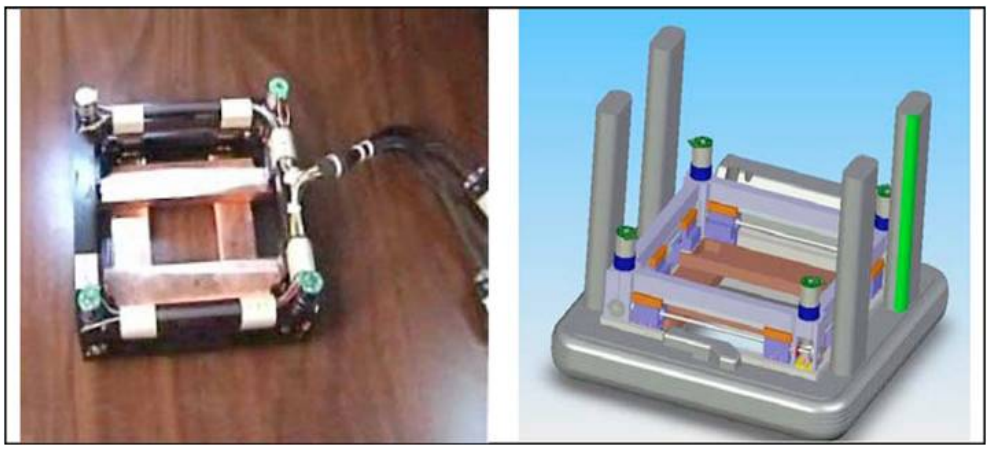

Figure 1.7: *FLEC prototype*

1.2.5 Few Leaf Electron Collimator (FLEC)

Al-Yahya et al ([35, 36, 37]) suggested an alternative approach for the delivery of energy and intensity modulated electron beams by using a Few Leaf Electron Collimator (FLEC) instead of a multileaf electron collimator. The FLEC is designed as an add-on device to an existing electron applicator and is composed by two pairs of trimmer bars that allow electron beam shaping using a combination of rectangular fields (figure 1.7). The photon jaws are also used as a back-up collimation device in order to reduce the leakage dose. The main advantages the FLEC offers compared to an eMLC are: (i) light weight, (ii) no requirements for radical changes to existing technology and (iii) small number of motors required. In the following sections the design, delivery and treatment planning of FLEC-based MERT will be further discussed.

Design and hardware characteristics

The FLEC leaves are made of Cu with thickness of 1.2 cm and width of 3 cm. The material was chosen as the most suitable for stopping high energy electrons, while minimizing the Bremsstrahlung yield, but without increasing significantly the total weight. The thickness was determined by the CSDA for 20 MeV electrons in Cu. Each leaf can move independently from each other and form any rectangular shaped field up to $8 \times 8\ cm^2$. For controlling the field sequence, each leaf is connected to a miniature stepper motor, microlimit switch and optical microencoder. A two-phase stepper motor with a four wire configuration was chosen to drive each leaf. The stepper motors have a weight of 3.3 g, a front shaft length

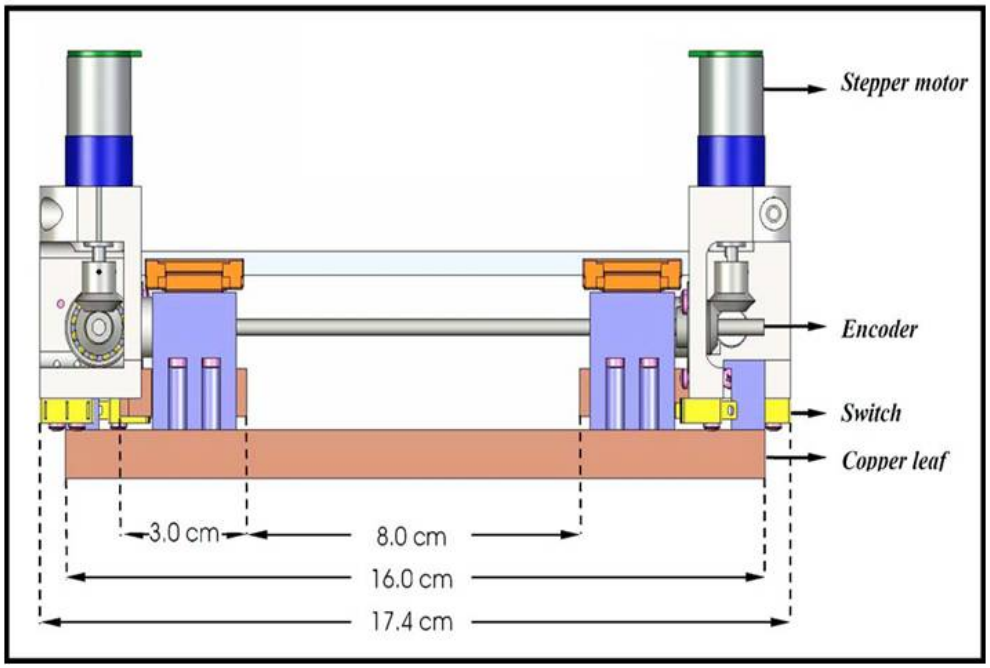

Figure 1.8: *Design characteristics of a Few Leaf Electron Collimator (FLEC). The leaves are made of Cu and have a width of 3 cm. Each leaf axis is connected with a stepper motor, optical encoder and switch for motion control.*

of 1.4 cm and can provide a torque of $1mN \cdot m$.

Automated movements of the FLEC leaves require the leaf positions to be verified by a position feedback device. The position feedback device is used in a closed loop operation and its purpose is to verify the leaf position after a movement has been executed by the motors. This is a crucial requirement for safe and accurate treatment delivery. Initially, CMOS-based optical encoders were chosen for that purpose, but since they do not have a high radiation tolerance, this approach will have to be reinvestigated. In section 1.3, different radiation-tolerant position sensing systems will be presented and discussed. Switches are also placed at the end of the leaf track to report any electronic/mechanical failure. Figure 1.8 shows a side view of the FLEC pointing out the dimensions and location of the various components.

The FLEC electronics are connected with an external controller using shielded, twisted pair cables. The controller is a delivery unit that is programmed to communicate with the optimization system to acquire the calculated optimum plan and then delivers the sequence to the FLEC and the linac console. At the end of the process, a file is produced containing the fieldlets to be used along with the beam energy and intensity (MUs). For

each fieldlet, 4 sets of parameters are determined: (i) The position of the FLEC leaves, (ii) the photon jaw settings, (iii) the beam nominal energy and (iv) the MU settings. The controller translates the file into commands that are send to the accelerator and FLEC. In that way a full treatment plan can be delivered in a remotely controlled fashion. The current design of the FLEC weights less than 2.5 kg.

Delivery techniques using the Few Leaf Electron Collimator

The FLEC was designed so that it would fit on the last scraper of an existing 15×15 cm^2 applicator, thus replacing the need for construction of cerrobend cut-outs. At that level the FLEC leaves define the field at a distance of 95 cm from the source. Thus, for a SSD of 100 cm the FLEC will be at 5 cm from the isocenter. The maximum possible field size opening with the current design is 8×8 cm^2 at 95 cm. Future designs for a 20×20 cm^2 and a 25×25 cm^2 applicator could provide a maximum field size of 13×13 cm^2 and 18×18 cm^2 respectively.

As mentioned previously, the photon jaws are also used during the delivery as a backup collimation device. Al Yahya et al [37] investigated the optimum settings for the jaw openings in order to reduce the leakage dose. He concluded that jaw openings that result in a projected to isocenter field size larger by 1 cm compared to the projected field size of the FLEC, exhibited the best compromise between dose penumbra 90/10 (width from the 90% to 10% isodose lines) and leakage dose peak. For example, if the FLEC projects to a 8×8 cm^2 at 100 cm then the jaws should project to a 9×9 cm^2 at 100 cm.

An important issue to be addressed is that the delivery of fields that are smaller than the maximum field size, results in unshielded open areas next to the leaves. Consequently, this will result to an increased leakage dose which especially for low energies might be unacceptably high for clinical use. Therefore it was recommended that the current design of the FLEC should not be used for a nominal electron energy of 6 MeV. Further investigation is required for reducing this effect.

Even though MERT is expected to reduce the dose to distal structures compared to conventional techniques, the target conformity and homogeneity might be degraded due to electron scattering. Al-Yahya et al [35] investigated the possibility of delivering FLEC-based MERT in conjunction with existing photon beam treatment modalities such as Intensity

Modulated Radiation Therapy (IMRT) and 3D Conformal Radiation Therapy (3D-CRT). They concluded that a mixed photon-electron beam therapy, namely MERT-IMRT, can reduce the dose to distal OAR and to the whole body, while preserving the target conformity and homogeneity.

Treatment planning-optimization procedure

The treatment planning process consists of 2 main phases, the planning phase and the optimization phase. After the optimization phase, the calculated optimum plan is being evaluated with the McGill Monte Carlo Treatment Planning software (MMCTP, Alexander et al [38]). If the plan does not pass the evaluation, then the process returns to the planning phase. A summary of the MERT treatment planning steps is given below. The procedure is described in more detail by Alexander et al [39].

- **Planning phase**

1. The DICOM data are imported in MMCTP. These include patient CT structures.
2. The target volume and external body contour are selected. An algorithm generates ideal, large field size, external beams based on the geometrical constraints. The algorithm determines the best possible beam positions based on target symmetry, projection width, depth and source to surface distance (SSD).
3. One or more of the previous beams are selected to cover the target volume.
4. The large beams selected in the previous step are broken down to smaller fieldlets. This improves the conformity of the beam shape with the target shape.
5. MC simulations of each selected fieldlet are executed using the BEAMnrc code for the transportation through the accelerator head. The resulting phase space file is then transported through the patient geometry (CT data structures) using DOSXYZnrc or VMC. The dose calculation results in a beamlet-specific dose distribution.

- **Optimization phase**

6. The objectives and constraints for the target volume and OAR are determined. These include a maximum dose, minimum dose, penalty value for the target, dose-volume constraint and a penalty value for the OAR.

7. According to the constraints set at the previous step, a dose-volume cost function is defined. The dose-volume cost function is a quantitative measure of the target and organ dose values, which fall outside the desired dose range. A gradient optimization algorithm determines the beam weights that minimize the cost function. Gradient algorithms may become "trapped" in local minima, thus not reaching the real optimum solution. In order to escape local minima, the results are then input to a stochastic algorithm to determine if further weight optimization is possible.

- **Evaluation phase**

8. The final plan, generated according to the calculated optimum combination of beam weights, is being evaluated within MMCTP. If the plan is not sufficient, the procedure returns to step (3) for a new selection of external beams.

The optimization procedure can be time consuming. Currently, the generation of an optimum treatment plan might require from a few hours to a few days, which is not clinically acceptable. The "bottleneck" of the procedure is the need for a full MC simulation of particles transporting through the accelerator head for every fieldlet. A faster approach would be the use of an *analytical, parameterized beam models* for the generation of the beam characteristics on the exit plane of the accelerator head.

1.3 Automated motion control in a radiation environment

Automated motion control of a collimator system is a crucial parameter for safe and accurate treatment delivery. For this purpose, a position feedback device has to be used to verify that the motor generated steps are being accurately translated in the corresponding leaf movements. This provides an extra level of confidence that field displacements and collisions will be avoided. In a high-radiation environment, such as the radiotherapy

treatment room, radiation tolerance is a necessary requirement for all the electronics used. Extensive research has been made in the past in reporting reference values of tolerance dose and dose rate of various electronic components commonly used in a radiation environment. As a reference point, standard electronics should be considered to start degrading at a dose of 10 Gy or more, while radiation-hardened electronics have proven to withstand up to 10 kGy. Below, the most common position feedback sensors are presented from the perspective of their radiation tolerance and performance.

- **Optical encoders** An optical encoder is an opto-coupler device attached directly on the axis of motion, which translates angular or linear movement to a sequence of pulses. An optocoupler consists of a light emitting diode (LED) on the input terminal and a photodiode on the output terminal. When a voltage is applied on the input terminal, the LED emits light which is then detected by the photodiode and turns on a transistor on the output terminal. The emitting light is interfered by the rotation axis which has a constant ratio of ticks/mm along it's periphery. As the axis rotates, the ticks will "cut-off" a number of photons according to the axis traveling. Consequently this will alter the number of pulses received by the photodiode and thus the output voltage. Optical encoders are one of the most reliable and accurate position sensors used in automated motion systems. However, the fact that CMOS-based transistors are almost exclusively used in modern optical encoders makes their radiation tolerance very poor. Thus, they are not recommended to be used in any radiation environment. Two solutions have been proposed to bypass this problem: (i) to "harden" the optocoupler or (ii) to remove the signal processing part from the radiation field. The first approach has been applied experimentally only in aerospace technology [41]. The second approach is feasible, but requires special design of the encoder.

- **Resolvers**: A resolver is much more reliable feedback device under radiation. However, their use in circuits requires more complex signal processing. Furthermore, the presence of coils close to the radiation field should probably be avoided.

- **Potentiometers:** Potentiometers have been used in the past in some nuclear environments. As the potentiometer turns with the rotation of the axis, it will change

Type of sensor	Total dose (MGy)	Dose rate (kGy/h)
Optical encoder (standard)	0.001	0.3
Optical encoder (hardened)	1	0.3
Optical encoder (fibre)	10	10
Resolvers	10	0.3
Potentiometer	0.1	N/A
Ultrasonic	10	10
Optical reflection	10	10
Electromagnetic (inductive)	20	10

Table 1.1: *Radiation dose and dose rate tolerance limits for various position feedback devices*

the resistance in an input circuit which will then alter a voltage on the output. If the output voltage is used as an input to the axis controller and the controller has been calibrated to maintain a constant voltage difference/mm ratio, the leaf position could be monitored in a reliable way. Problems associated with potentiometers include the relative high noise levels and high sensitivity to atmospheric conditions. The latter is the main reason why potentiometers are not commonly used in aerospace and nuclear reactor technology. Nevertheless, the environmental conditions in a radiotherapy treatment room are fairly stable and thus potentiometers could be a possible solution.

- **Non-contact position sensing devices:** This category includes ultrasonic, optical reflection, electromagnetic laser or video sensors. These are technologically more sophisticated solutions that increase the complexity of the system, without offering any advantage in precision.

Table 1.1 exhibits the radiation tolerance limits for some of the above position feedback sensors according to test results published by Decreton (1995) [40].

Since resolvers involve magnetic coils and non-contact position sensing devices probably are too complicated solutions, the only practical solutions left for use in a clinical high-radiation environment are the optical encoders and potentiometers. The former are very accurate, but present poor radiation tolerance and the latter present higher radiation tolerance but are more sensitive to environmental conditions. In chapter 2, two approaches

will be investigated for the implementation of a position feedback system for controlling an electron collimator: first, the use of optical encoders with protective shielding and second the use of an analog position feedback system with potentiometers.

1.4 Beam models

1.4.1 General

A beam model can be defined as

> *any algorithm that delivers the location, direction and energy of particles to the patient dose-calculating algorithm* (AAPM TG 105 [42])

As it was described in section 1.1.6, current MC patient dose calculation algorithms have reached the computation speed required for clinical implementation. In order to provide accurate dose calculations the need exist for accurate input in the above algorithms, hence the location, energy and direction of the incident particles should be *representative* of the real beam characteristics. One way to derive very accurately the beam characteristics is by full MC simulation of particle transport through the accelerator geometry. However, this approach results in time consuming calculations and large storage requirements, especially for dynamic deliveries and small fields. In general, three ways of deriving the incident beam characteristics can be identified: (i) *Full MC simulation of the accelerator head*, (ii) *Analytical/parameterized beam models based on pre-calculated MC simulations and/or analytical formulas* and (iii) *Analytical/parameterized beam models based on measurements*.

The procedure of implementing a beam model can be summarized in two basic steps: first, a *beam representation* has to be derived. The beam representation can be considered as a *mathematical description* of the beam characteristics, namely location, energy and direction of the particles on the exit plane of the accelerator. This mathematical description could be an analytical function or histogram derived by MC simulations (approach (ii)) or measurements (approach (iii)). The data storage requirements for the beam representation should be significantly smaller than that for a phase-space file, as derived by full MC simulations. The second step involves *beam reconstruction* of the phase-space data based on the beam representation. The phase-space data are reconstructed, particle-by-particle,

by the mathematical description of the beam and then used as an input into the dose calculation engine. The accuracy of the reconstructed beam depends on the assumptions made during the representation phase and have to be evaluated by full MC calculations or measurements.

Analytical/parameterized, MC-based beam models (approach (ii)) are based on the idea that particles exiting the linear accelerator can be grouped according to the location of last interaction in the accelerator's treatment head. Therefore a linac can be considered as a summation of *sub-sources*, each representing one or more of the major components of the treatment head. Particles coming from the same sub-source are assumed to share similar characteristics. For each sub-source, spatial and energy fluence distributions can be derived by full MC simulations on the exit plane. During the reconstruction phase, the distributions are sampled to derive the location, energy and direction of each particle. This approach has been proposed for conventional electron beams by Ebert and Hoban [44] and C-M Ma et al [45, 46]. In order to extend the validity of a beam model to any linear accelerator, Jiang et al [47] proposed that the sub-sources can be "adjusted", without redoing the simulations, so that they match measured depth-dose curves and dose profiles.

Analytical/parameterized measurement-driven models (approach (iii)) involve derivation of the beam characteristics from measurements instead of MC simulations. The beam representation may be developed from analytical models whose parameters are optimized based on minimizing the differences between calculations and measurements. The main advantage of this approach is that the accuracy of the model does not depend on the geometrical information of the accelerator's treatment head, since the beam characteristics are derived based entirely on measured dose distributions. Furthermore, the commissioning procedure can be more straightforward for a clinical physicist, since it does not require MC expertise. However, the energy distributions can not be derived as accurately as with MC and rigorous verification of the model's accuracy is needed to be performed in heterogeneous phantoms. Jansen et al [48] have described a purely measurement-driven model for deriving the beam characteristics in conventional electron beam treatments.

In the following sections, previous work in electron beam modeling will be presented with emphasis on analytical/parameterized MC-based models (approach (ii)).

1.4.2 The work by Ebert and Hoban

Ebert and Hoban [44] developed an analytical MC-based model to account for the scattered particles produced from an electron applicator. Their model is based on the idea of *superposition* and *sampling* of *scatter kernels* established for the different applicator scrapers and their corresponding edge elements. The scatter kernels are derived by full MC simulations. The result of the model is a phase-space file of applicator scattered particles which can be used as an input to a dose calculation engine.

In their work, they assume that each scrapper of an electron applicator can be decomposed to semi-infinitely long edge elements. Characteristics of scattered particles from each edge element are stored in a *scatter kernel*. A scatter kernel is a 2D Cartesian array of voxels representing the fluence of scattered particles beneath the edge relative to incident primary beam fluence. The energy distribution is also scored in each voxel. Different particle types are scored in separate kernels. The incident primary beam characteristics were determined by simulation of initially monoenergetic electrons passing through the scattering foils and air in combination with open beam measurements (no applicator present). The angular characteristics were derived by measurements of the beam penumbra.

In a follow-up study [43], Ebert and Hoban investigated the characteristics of applicator scattered particles. They concluded that most scattered electrons emerge from the vertical edge face of an edge element and their characteristics are highly depended on the incident beam angle. In order to account for the different incident angles, a library of scatter kernels was created for a set of discrete edge radii relative to the primary beam central axis. For different field sizes and applicator cut-outs the corresponding scatter kernels are loaded.

The reconstruction phase consists of the following steps: first, the requested applicator aperture is broken up into elements and the number of particles required in the phase space file is specified. Then this number is broken up into contributions from each aperture making up the applicator and then each element in each aperture. The final phase-space distribution can be derived as a *superposition* of all scatter kernels. For each aperture α and edge element k, a scatter kernel can be defined mathematically as: $R_\alpha^k(\phi, \psi, r_\alpha^k) \cdot \Omega_\alpha^E(i, j, r_{eff}^k)$. The factor $\Omega_\alpha^E(i, j, r_{eff}^k)$ corresponds to the relative fluence value of the i,j voxel of the scatter kernel for aperture type α at radius r for an electron beam incident energy E. r_{eff}^k is the effective radius of the edge element k. $R_\alpha^k(\phi, \psi, r_\alpha^k)$ is an operator

accounting for the source to aperture distance through the element position r_α^k, the angle of obliquity ψ and angle of incidence ϕ.

The primary beam fluence can be defined as: $\Phi^p(r) = \Phi_s^p(r)\Phi_{CA}^p$, where $\Phi_s^p(r)$ is a function describing the shape of the primary beam fluence profile and Φ_{CA}^p is the central axis primary beam fluence. In their study they assumed a uniform and symmetric primary electron beam fluence distribution with uniform energy spectrum.

The total fluence distribution can be defined as follows:

$$\frac{\Phi(x,y)}{\Phi_{CA}^p} = \sum_{\alpha}^{N^{apertures}} \sum_{k}^{N_k^{elements}} \sum_{i,j}^{kernel\ size} \Phi_s^p(r_\alpha^k) \cdot R_\alpha^k(\phi,\psi,r_\alpha^k) \cdot \Omega_\alpha^E(i,j,r_{eff}^k) \tag{1.15}$$

The model was then evaluated by comparing depth dose distributions and dose profiles with measured data for different field sizes (including a case of an irregular field). The results showed good agreement in areas where electronic equilibrium exists. Discrepancies of the order of 5-7% were mainly encountered in the build-up region. The authors attributed the discrepancies to one of the following assumptions:

- Open beam measurements (no applicator present) for representing the measured primary beam component
- Uniform spatial and energy fluence distribution for the simulated primary electron beam component
- Point source approximation for primary beam monoenergetic electrons
- No angular deviation in the establishment of scatter kernels
- Neglect of electron production in the applicator materials due to primary beam photons
- Common origin for particles scattered from a particular edge element

Even though the significance of the above assumptions in the encountered discrepancies was not investigated in their study, it is apparent that further improvement of the model should mainly improve the primary beam characteristics and the directional characteristics of air-scattered particles. Another useful observation the researchers made was that

scattered photons from the applicator and cut-out showed a negligible contribution to the final scatter dose distribution. Nevertheless, they point out that a photon component is in general necessary for electron beam modeling to ensure consistency in the Bremsstrahlung tail of the depth dose curve.

1.4.3 The work by Ma et al

Ma et al [45] (1997) presented a method for accurate characterization of clinical electron beams by using the BEAM and BEAMDP codes. Their method results in considerable memory and time savings, while preserving the accuracy of the model within clinically acceptable levels.

In their work, particles reaching the exit plane of a linear accelerator are considered to come from simplified sub-sources. Each sub-source mimics the geometrical dimensions of one or more components of the accelerator's treatment head. By performing MC simulations of the full accelerator model, the fluence and energy distributions are obtained for each sub-source. During the reconstruction phase the particle's energy and position are sampled from the known distributions and the direction is estimated by geometrical information.

The beam representation phase begins with a MC simulation of the full accelerator model with each component assigned to a different LATCH bit value. LATCH is a 32-bit variable that can be used in BEAM for monitoring a particle's history. Bit 30 is used for storing the particle's charge. Bits 1-23 of LATCH are used to record where the particle has interacted or passed through. Therefore the different components of an accelerator should be assigned a unique bit value during this phase. Particles reaching the exit plane will have a bit value of 1 for every region they interacted with. During the analysis of the LATCH variable for each particle the following assumptions are made: (i) For charged particles, the origin is considered to be the last non-air region where the particle interacted and (ii) for bremsstrahlung photons, the origin of a particle is considered to be the component in which it was generated or last scattered. According to these assumptions the sub-sources are defined and their relative intensity is calculated (number of particles from the sub-source/total number of particles). Sub-sources with relative intensity of less than 0.1% are considered non-significant and are ignored.

The next step is to derive the spatial fluence and energy distributions for each significant sub-source. These distributions will be used as probability distributions during the reconstruction phase. The spatial fluence distributions can be stored in bins of radial or square ring shape. In this way the scored area is larger and thus the statistics improved. A functional parameterization is also used to account for fluence variations in each bin. The energy distributions are binned according to the minimum and maximum energy and number of bins defined by the user. In general a bin size of 0.1 MeV was considered adequate. In-field, out-field spectra were considered separately.

The beam reconstruction phase begins by determining which sub-source will emit the next particle. This is done by sampling from the relative source intensity distributions. Afterwards, the energy and position of the particle are selected by sampling from the spatial and energy probability distributions derived during the representation phase for that sub-source. Finally, the particle's direction is calculated. A point on the sub-source origin surface plane is selected. By connecting the origin point with the location on the exit plane, an initial estimation of the particle's direction can be made. This straight line approximation is not very accurate for electrons and has to be corrected for air scattering. Therefore, a perturbation correction term was introduced to account for multiple scattering in air. The perturbation value is determined by sampling the angular distribution of direct electrons in air and and then scaled down according to the sub-source to exit plane distance. Later on, Jiang et al (2000) [47] introduced a more accurate correction for electron multiple scattering in air by the use of the Fermi-Eyges multiple scattering theory.

The final fluence distribution of the multiple-source model can be defined mathematically as follows:

$$\Phi(x, y, u, v, E) = \sum_{j=1}^{m} \phi_j \cdot f_j(E) \cdot g_j(x, y, x_s, y_s) \tag{1.16}$$

where: ϕ_j is the relative source intensity of sub-source j, f(E) is the energy fluence distribution, $g(x, y, x_s, y_s)$ is the spatial fluence distribution and x_s and y_s are the x- and y- coordinates on the origin plane.

The multiple-source model proposed by Ma, requires the storage of a few kBytes of data for the beam parameters (instead of hundreds of MBytes for a full phase-space file) and results to time savings of the order of 10 or 100 compared to a full Monte Carlo

simulation. It should be pointed out that the time savings are *not* a result of "*avoiding*" the particle transport calculations through the accelerator's treatment head; a *full MC simulation* of the accelerator head is *still required* for each field size to derive the beam model. However, the use of square-ring shaped bins for storing the fluence distributions results in an "averaging" effect, as well as provides a relative larger collecting area compared to a grid of square pixels. These two factors reduce the statistical fluctuations. Therefore, the total number of particles required to derive the same statistical accuracy with the full MC simulation can be *reduced* by one or two orders of magnitude and consequently the gain in calculation speed will be increased by a factor of 10 to 100. The drawback of this model is that it is limited to symmetric fields. Therefore, the effect of a cut-out shaped, irregular field size has to be incorporated in the patient's dose calculation phase. Detailed information about Ma's multiple-source model can be found in references [45, 46].

1.4.4 The work by Vatanen et al

Vatanen et al [49] presented a beam model for modulated electron radiation therapy with an eMLC. The eMLC prototype consisted of steel leaves mounted in an aluminum frame and placed beneath the last scraper of a 20×20 cm^2 applicator. The beam model was derived by the conventional electron beam model implemented in the Oncentra MasterPlan treatment planning system.

The beam model divides the electron beam into a direct electron component Φ_D, an indirect/scattered electron component Φ_I and a Bremsstrahlung photon energy fluence component Ψ_B that accounts mainly for Bremsstrahlung photons produced in the scattering foils. The beam model uses a combination of measured and MC simulated data to characterize the various beam components.

The beam characterization begins with the utilization of a source phase space after the secondary scattering foil. The source energy spectrum is derived by fitting weights of superimposed mono-energetic depth dose curves to a measured open field depth dose curve. The source spatial fluence distribution is derived by fitting measured air fluence profiles against simulated air fluence profiles. The source phase space is then propagated through all apertures down to the exit plane by a MC particle transport simulation. Electrons that hit any surface during their path are scored to a "leaf hit" file and then terminated. The

particles that will reach the exit plane (below the eMLC) represent the direct component Φ_D. Since all the collimating devices before the eMLC are static, the primary beam component should remain the same irrespectively of the field size. The particles are assigned an average direction $\overline{\theta}(r) = tan^{-1}(\frac{r}{z_{eff}(r)})$, where $r = \sqrt{x^2 + y^2}$ is the distance from the beam axis and z_{eff} is the distance to a virtual point source.

The indirect electron component Φ_I consists of direct electrons hitting a collimating aperture and scattered back into the field. The researchers considered the two upper applicator scrapers and the eMLC as the most significant sources of scattered particles. Scattered particles were further grouped into two cases: (i) grazing incidence on the front face and (ii) near perpendicular incidence on the inner edge surface of the scattering medium. A set of scatter kernels were then produced using the EGSnrc code. The scatter kernels were derived for specific cases of materials, geometry, energy, leaf thickness and incident angle.

The reconstruction phase begins with sampling the direct electron component Φ_D. The direct electrons are first generated in an open rectangular field. Then, each electron is backprojected to the upper surface of the eMLC and then ray-traced downwards according to their direction. It is then checked if the electron will hit any of the eMLC leaves, according to the specified field shape. If the electron does not hit any of the leaves, it is fed directly into the dose calculation engine. Therefore, the direct component dose is first calculated. Afterwards, the indirect component dose is calculated by reading particle-by-particle from the "leaf hit" file. The particle is then assigned a direction and energy from the scatter kernels and then fed into the dose calculation engine.

Comparison of calculated and measured dose distributions showed the following discrepancies: (i) calculated depth dose curves and dose profiles were underestimated up to 8% close to the surface, especially for high energies and small fields and (ii) Overestimation of calculated dose near the edge of the field, especially for the case of extended SSD. However, this study showed that an analytical/parameterized beam model for dynamically modulated electron fields is feasible and can provide the necessary time gain.

In chapter 2 the method for implementing a fast beam model, specifically designed for MERT deliveries with a Few Leaf Electron Collimator, will be presented. The proposed method promises to improve some of the issues encountered in the models previously presented, such as the capability of deriving the beam characteristics of assymetric field sizes

(Ma et al) and the capability of preserving the accuracy of the primary beam component (Ebert and Hoban, Vatanen et al).

Chapter 2

Materials and Methods

2.1 Beam model

2.1.1 General

The beam model developed in this work is a *analytical/parameterized, MC-based beam model* capable of reproducing the location, energy and direction of the particles on the exit plane of a linear accelerator. The applied method is significantly influenced by previous work in electron beam modeling (presented in section 1.4), but extended to handle FLEC-based dynamic deliveries. The model divides the beam into two separate components: (i) primary beam, consisting of all the particles (electrons and photons) that did not interact with any collimating devices and (ii) scatter beam, consisting of scattered particles from collimating devices.

The development of the beam model for the scatter beam can be summarized in the following steps:

1. *Beam characterization*: The BEAMnrc/EGSnrc code was used to simulate the accelerator head and electron applicator, including the FLEC. Phase space files (PH-SP) were generated on the output plane (back of the FLEC) by full Monte Carlo (MC) simulations. Figure 2.1b shows a sketch of the Varian Clinac 21EX accelerator head (including the FLEC). The validated BEAMnrc model used for the MC simulations is shown in figure 2.1a.

2. *Identify significant sources*: The PH-SP data were analyzed to identify the significant

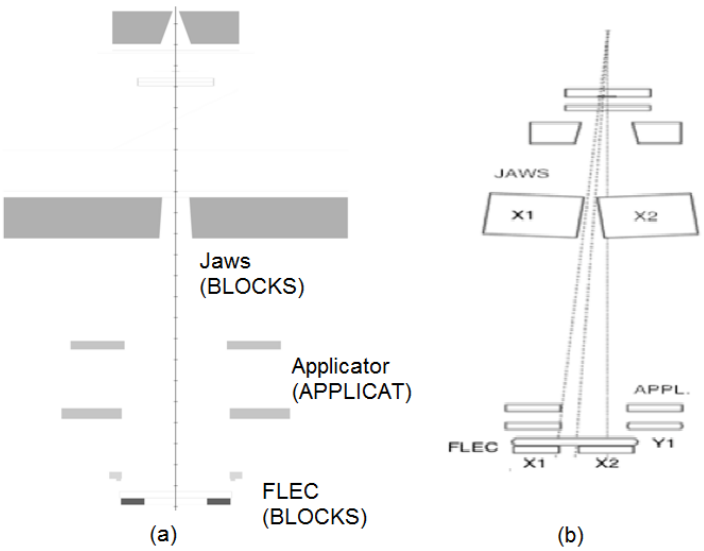

Figure 2.1: *(a) The BEAMnrc model for a Varian Clinac 21EX including the electron applicator and FLEC (b) Sketch of the accelerator head, including the FLEC. Jaws and FLEC are used as collimating devices.*

sources of radiation. Sources that did not contribute significantly (relative intensity less than 1%) were ignored.

3. *Decomposing the accelerator*: The collimating devices were decomposed to their independent leaf elements. "Virtual" beam models of the accelerator head were created, where each jaw and corresponding FLEC leaf were isolated from the rest of the leaves, which were replaced by air.

4. *Deriving the source scatter kernels*: Full MC simulations of the "virtual" beam models were performed for each jaw and FLEC leaf possible position. Particle spatial fluence and energy distributions for each sub-source were collected and saved as 2D histograms/scatter source kernels (SSK) on the output plane. In this work a SSK is defined as a 2D matrix of fluences on the output plane.

5. *Sampling and reconstruction*: For each field requested, the appropriate SSKs are first loaded. Each particle is assigned to a source randomly selected according to the relative source intensities. A leaf element for that source is randomly chosen and considered as the particle's origin. The location and energy of the particle are then derived by randomly sampling the fluence and energy distributions of the leaf's SSK. An estimation of the particle's direction is calculated based on the source's geomet-

rical information. By decomposing the collimating devices to their independent leaf elements the proposed method provides a way to re-generate *arbitrary rectangular fields* during the reconstruction time.

The primary beam is derived by a full MC simulation of the accelerator model using the BEAMnrc code. During the simulation, particles that reach the boundary of a collimating device are immediately rejected. Thus, particles reaching the exit plane have been transported only through air. Furthermore, the electron step algorithm and boundary crossing algorithm parameters were modified from their default values. These modifications resulted in a significant time gain for the generation of phase space files of the primary component (electrons and photons), without significant loss in accuracy.

In the following sections, the BEAMnrc/EGSnrc Monte Carlo code will be briefly presented and the proposed methodology for the FLEC-based beam model will be discussed step by step.

2.1.2 BEAMnrc

BEAMnrc [8] is a general purpose Monte Carlo code for simulating high energy electron and photon beams of radiotherapy units. BEAMnrc is based on the EGSnrc Monte Carlo system of radiation transport. BEAMnrc can be used to design an accelerator model by implementing a sequence of component modules (CM). A CM represents a specific component of the accelerator. The user defines the exact physical geometry and material composition of the CMs. Furthermore, each CM is independent of the rest, which provides the flexibility of modifying the accelerator model according to the specific physical characteristics of the linear accelerator. Some of the most commonly used CMs in this work were: SLABS, CONESTAK, FLATFILT, PYRAMIDS, JAWS and BLOCKS. There are several types of component modules available to the user that provide different structures and restrictions. Some CMs are more suitable than others for designing specific parts of the accelerator. However different CMs, if adjusted properly, should produce identical results. For example, it is possible to create the same geometry for collimating devices (such as the secondary collimator or FLEC) by using the JAWS or the BLOCKS CMs. While the former results in calculations that are almost twice as fast, only the latter can reproduce assymetric and

off-axis shapes. Therefore the user should decide which CM to use according to the type of simulation performed.

The therapy source is modeled with the z-axis placed on the central axis beam and the origin of the coordinate system on the center of the accelerator's vacuum. The user can define one or more scoring planes which are placed at the back of a CM. At these planes, the BEAMnrc code can store a file with *phase-space* data of the beam. The phase-space file contains the following information for each particle (in this order): LATCH (containing the particles charge and history information - described in section 1.4.3), E (energy), X (X-position), Y (Y-position), U (X-direction cosine), V (Y-direction cosine), WT (particle's weight). This information can then be used for deriving the spatial, energy and directional fluence distribution of the beam.

There are various source types that can be used for simulating the original electron beam as it exits the accelerator's vacuum. Some of the most common are: point source, parallel circular or rectangular beam and elliptical beam with Gaussian distributions in X and Y. There is also the option to use a phase-space file as an input. In that case, the user can first perform a full MC simulation of the field-independent part of the accelerator and save the phase space file (referred to as master phase space file). Field-dependent simulations can then start directly from that plane, without the need of repeating the simulation of the first part. For example, a master phase space file can be created for each beam energy just before the photon jaws (secondary collimator) and then used as an input for sub-sequent simulations.

Figure 2.1a exhibits the BEAMnrc model of a Varian Clinac 21EX accelerator head including a $15 \times 15\ cm^2$ electron applicator and the FLEC. In the figure, the collimating devices and the corresponding CM used for representing them are shown. It should be noted that the BLOCKS CM was chosen for representing the jaws and FLEC since it is the only CM that can represent off-axis and arbitrary rectangular field sizes. The BEAMnrc model has been previously validated with measurements and exhibited good agreement.

BEAMnrc/EGSnrc parameters

There are various BEAMnrc/EGSnrc parameters that control the way the electron transport calculation is performed during a BEAMnrc simulation. According to the values

assigned to these parameters the user can potentially increase the accuracy or the efficiency of the simulation. In the following, some of the most important parameters, that were modified in the frame of this study, are described.

- *Electron step algorithm:* determines the algorithm used to take into account lateral and longitudinal correlations in a condensed history step. There are two options available: PRESTA-I which is faster, but it has shown to underestimate lateral deflections, underestimate longitudinal straggling and to produce a singularity in the distribution describing the lateral spread of electrons in a single condensed history step. PRESTA-II is a more accurate algorithm developed for EGSnrc with the expense of being more time consuming.

- *Boundary Crossing Algorithm (BCA):* when an electron reaches close to an interface between different materials, a portion of it's curved path may be in a different material than that simulated, resulting in an erroneous trajectory. There are two options for the BCA: PRESTA and EXACT. According to PRESTA, when an electron reaches the boundary at a perpendicular distance smaller than a user specified value called *skin depth for BCA*, the lateral deflections are switched off and the electron is transported on a straight line to the boundary. The effect of multiple scattering is then introduced as a correction. According to EXACT, for perpendicular distances smaller than skin depth for BCA, the electron transport will switch to single scattering mode. The PRESTA algorithm has shown to overpredict dose in small air cavities surrounded by a dense material (such as in the case of an ionization chamber).

- *Skin depth for BCA (SDBCA):* Skin depth for BCA is defined as the perpendicular distance of an electron track to the next boundary after which the electron transport will switch to single scattering mode (EXACT) or PRESTA straight line transport. Its value is given in mean free paths (mfp). In general, a SDBCA value of 3 mfp has shown the best compromise between accuracy and efficiency. If BCA=PRESTA and SDBCA=0, then the simulation will run according to the original PRESTA algorithm. If BCA=PRESTA-I and SDBCA=large, then the entire simulation will run with no lateral deflections in the condensed history steps. If BCA=EXACT and SDBCA=large, the entire simulation will run in a single scattering mode.

- *Electron cutoff energy (ECUT):* defines the electron cutoff energy. If the electron's energy becomes smaller than ECUT, then the history is terminated and the particle deposits the residual energy locally. An ECUT value of 0.7 MeV is usually accurate enough for radiotherapy simulations.

- *Photon cutoff energy (PCUT):* same as ECUT, but for photons. A PCUT value of 0.01 MeV is commonly used.

- *Electron range rejection (ECUTRR):* Range rejection is a technique used to reduce the simulation time. The idea is that if an electron does not have enough energy to exit the current CM then it's history is immediately rejected. There are two options available: set ECUTRR, where range rejection is performed for each individual region and varying ECUTRR, where range rejection is performed according to whether the particle will reach the bottom of the accelerator (this case can only be used if there is only one scoring region at the bottom of the accelerator). However, terminating a particle's history will result in losing all the Bremsstrahlung photons that would have been created during the electron transport. The effect is more pronounced for higher energy photons. The variable ESAVE can be used to set an energy threshold value above which range rejection is no longer allowed. An ESAVE value of 2 MeV has shown to be adequate for most cases. Range rejection can increase the calculation speed by a factor of 2.

2.1.3 Beam characterization

Beam characterization consists of the study of the beam spatial fluence and energy distributions on the accelerator's exit plane as well as the identification of the accelerator's components that are significant sources of radiation. In BEAMnrc the LATCH variable can be used to track the particle's history. Since a particle would probably have been through many different components, there is no unique way to define the particle's origin. In this study the following assumptions are being made:

1. The origin of a charged particle (electron/positron) is the last (non-air) component that it has been to.

2. The origin of an uncharged particle (photon) is the last (non-air) component that an interaction occurred.

Figure 2.1a shows the BEAMnrc model of a Varian Clinac 2100EX accelerator including a 15×15 cm^2 applicator and the FLEC. During the delivery of modulated electron beams, the jaws (secondary collimator) are used as a back-up collimation device. Therefore, a master phase-space file was first created before the jaws for each energy. The master phase-space file was then used as a source for the field-dependent part of the accelerator. Different LATCH bits were assigned to each individual component. The beam was considered to consist of 7 main components, according to the particle's origin: Primary (consisting of all the particles whose origin was before the jaws), Jaws Y (scattered particles from the upper pair of leaves of the secondary collimator), Jaws X (scattered particles from the lower pair of leaves of the secondary collimator), Applicator (scattered particles from the applicator's scrapers), Al frame (scattered particles from the FLEC's Al frame), FLEC Y (scattered particles from the FLEC's upper pair leaves) and FLEC X (scattered particles from the FLEC's lower pair leaves).

Full MC simulations were performed for nominal energies of 6 MeV and 20 MeV and field sizes of 2×2 cm^2 and 8×8 cm^2. Phase-space files were collected on the exit plane (back of the FLEC) and the particles were classified according to their origin. Table 2.1 and 2.2 exhibit the electron and photon fluence output on the exit plane (normalized to maximum fluence output). The fluence outputs were calculated by the following formula:

$$Fluence\ Output = 100 \times \frac{N_{exit}^{source\ i}}{N_{incident}^{original\ source}}, \tag{2.1}$$

where $N_{exit}^{source\ i}$ is the number of particles from source i that were collected on the exit plane and $N_{incident}^{original\ source}$ is the number of incident particles from the original source.

From tables 2.1 and 2.2 the following can be deduced:

- The *primary* beam constitutes the *most significant* source of the electron beam (24.5 % - 77.2 %).
- The *applicator* constitutes the *least significant* source of the electron beam (less than 1.2 %).

	$8 \times 8\ cm^2$		$2 \times 2\ cm^2$	
Source	20 MeV (%)	6 MeV (%)	20 MeV (%)	6 MeV (%)
Total	100	100	100	100
Primary	77.2	77.2	55.5	24.5
Jaws Y	4.8	4.4	3.3	2.4
Jaws X	4.2	3.8	8.8	12.3
Applicator	1.1	0.6	0.1	0.3
Al frame	4.0	8.8	6	52.2
FLEC Y	4.8	2.5	9	3.6
FLEC X	4.8	2.2	16.3	4.6

Table 2.1: *Electron fluence output for energies of 6 and 20 MeV and field sizes of* 2×2 cm^2 *and* 8×8 cm^2.

	$8 \times 8\ cm^2$		$2 \times 2\ cm^2$	
Source	20 MeV (%)	6 MeV (%)	20 MeV (%)	6 MeV (%)
Total	100	100	100	100
Primary	52.3	60.3	43.7	49.5
Jaws Y	1.8	1.4	1.8	1.7
Jaws X	3.6	2.8	6	6.4
Applicator	0.5	1.2	0.2	0.4
Al frame	0.8	5.2	0.2	3.2
FLEC Y	22	15.4	23.3	18.4
FLEC X	18.8	13.6	24.3	20.4

Table 2.2: *Photon fluence output for energies of 6 and 20 MeV and field sizes of* 2×2 cm^2 *and* 8×8 cm^2.

- The jaws (secondary collimator) is a significant, non-negligible source for the electron beam (total: 8.2 % - 14.9 %).
- The FLEC is a significant, non-negligible source for the electron beam (total: 4.7 % - 25.3 %).
- The primary beam and the FLEC are the most significant sources for the photon beam (FLEC: 29% - 47.6 % and primary: 43.7 % - 60.3 %).
- The jaws contribution to the photon beam is less significant than it is for the electron beam.
- The Al frame is a non-negligible and some times very significant source of radiation.

Since electrons contribute more significantly to the dose distribution than photons (except in the Bremsstrahlung tail), the following discussion is mainly focused in deriving a beam model for the prediction of the electron beam character.

Figures 2.2 and 2.3 exhibit the electron spatial fluence and energy distributions for 20 MeV (A and B) and 6 MeV (C and D), for field sizes of $8\times8\ cm^2$ and $2\times2\ cm^2$ respectively, for all the significant sources. The following can be deduced:

- The primary beam fluence is more uniform for higher energies and more forward peaked for lower energies. The effect is more dominant for larger field sizes.
- The scattered beam from the jaws exhibits an almost uniform fluence distribution in the treatment field.
- The scattered beam from the FLEC exhibits an increased fluence closer to the edges of the treatment field. The effect is more dominant for larger field sizes.
- The scattered beam from the Al frame contributes almost exclusively out of the field. The effect is more dominant for smaller field sizes and lower energies.
- The energy spectra for the primary, jaws and Al frame scattered beam have similar shape. The distributions exhibit a peak for higher energies and much smaller contribution from lower energies.
- The FLEC scattered particles exhibit a more uniform energy spectrum.

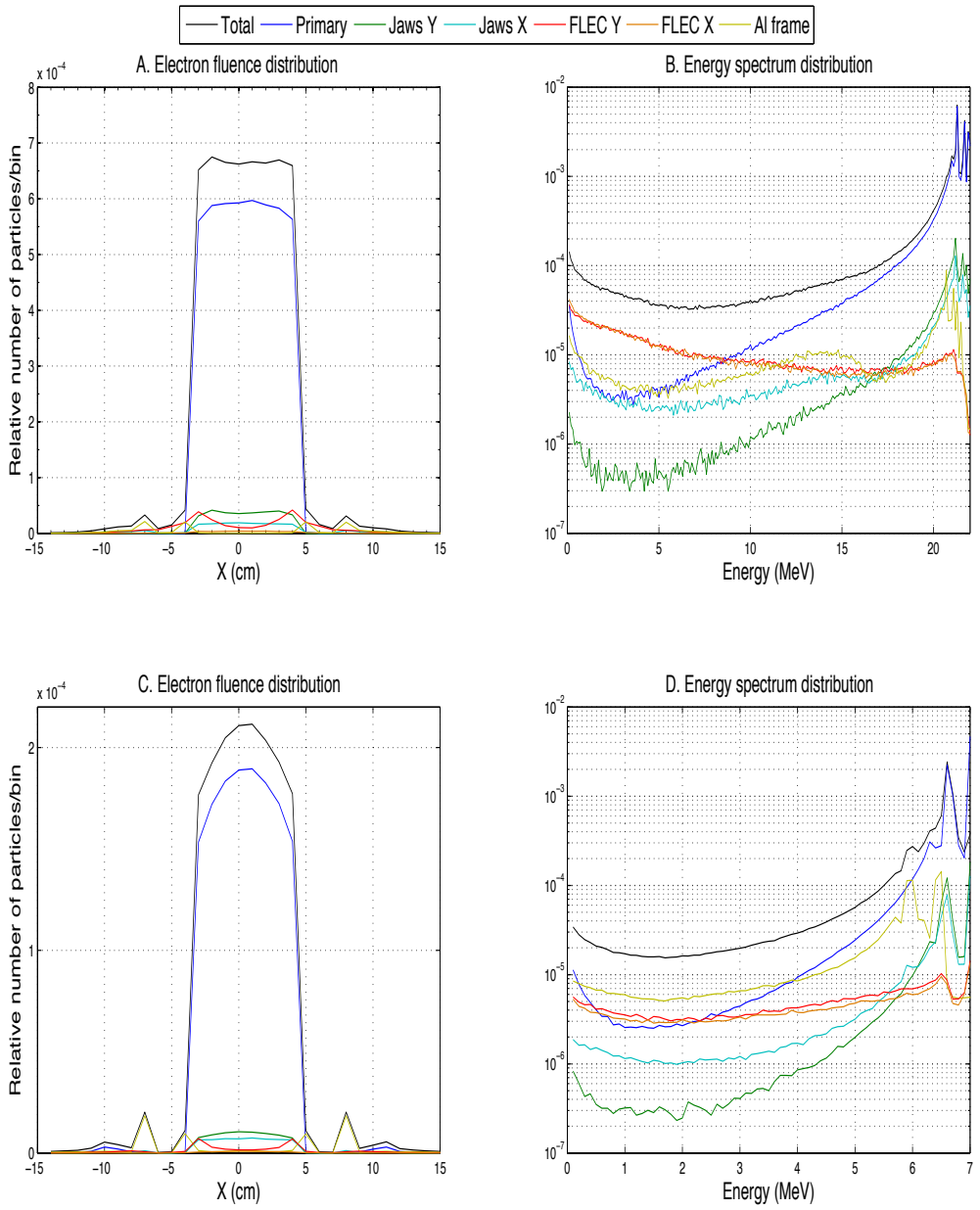

Figure 2.2: *Electron beam characteristics of significant radiation sources (field size:* 8×8 *cm^2). A. Spatial fluence distribution (20 MeV), B. Energy fluence distribution (20 MeV), C. Spatial fluence distribution (6 MeV) and D. Energy fluence distribution (6 MeV)*

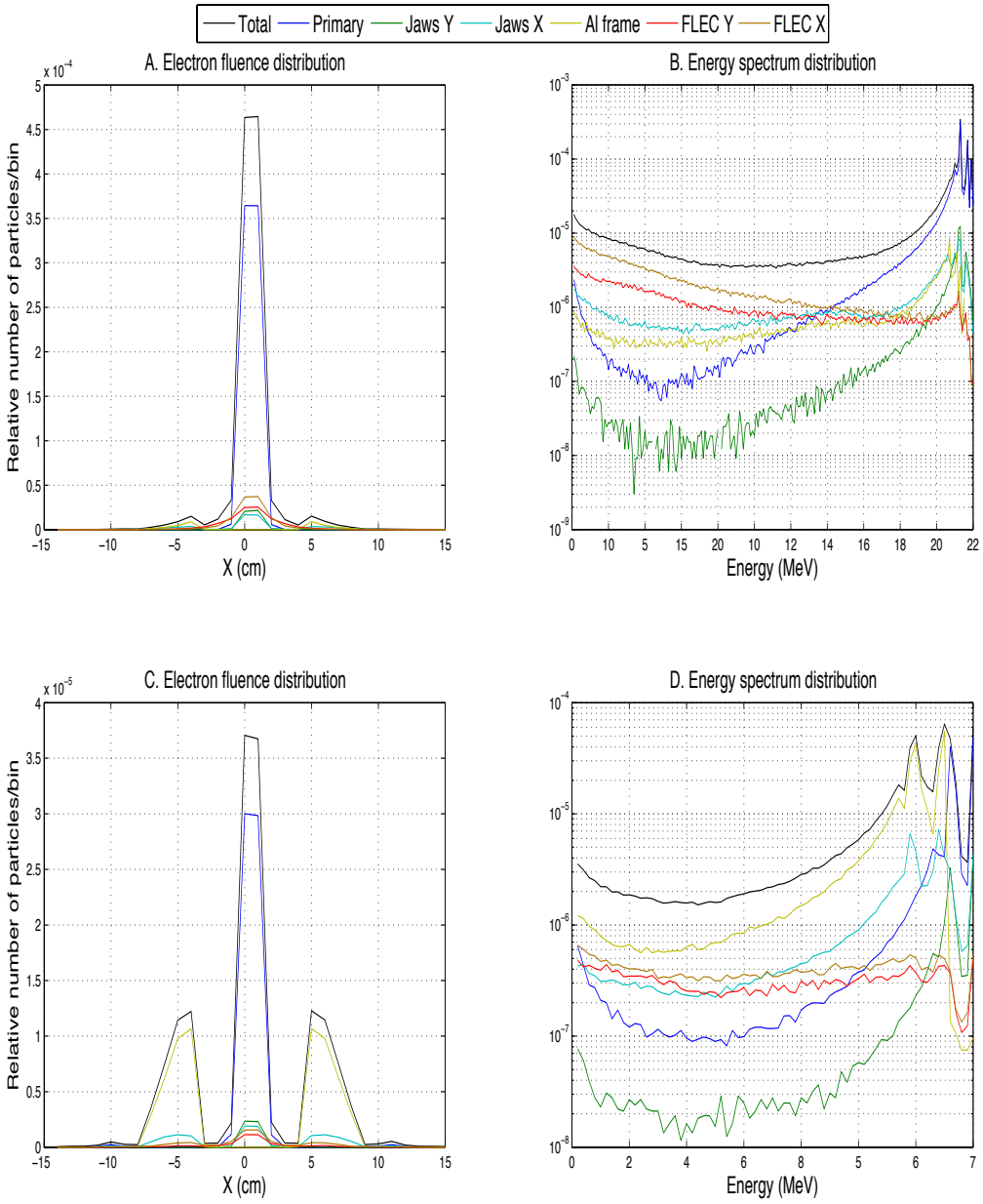

Figure 2.3: *Electron beam characteristics of significant radiation sources (field size:* 2×2 *cm^2). A. Spatial fluence distribution (20 MeV), B. Energy fluence distribution (20 MeV), C. Spatial fluence distribution (6 MeV) and D. Energy fluence distribution (6 MeV)*

- The individual leaf pairs (X and Y) for the jaws and FLEC exhibit similar energy spectra between each other.

The primary beam is the most significant source, therefore it is crucial to maintain the accuracy for this source as high as possible. Furthermore, the shape of the primary beam distribution is strongly depended of the collimation devices making challenging the prediction of the spatial fluence distribution's shape in an analytical fashion. As a consequence, the primary beam should be derived directly by a full Monte Carlo simulation. Since the primary beam consists of particles transporting only through air the MC simulation should be expected to be performed fast.

Electrons scattered from the FLEC's Al frame exhibit similar energy characteristics with the primary beam and jaws, but located mainly outside the treatment field in the penumbra region. Taking into consideration that the Al frame is a low atomic number material and its thickness relatively small (2-3 cm above the FLEC and 1 mm below the FLEC), it can be assumed that the scattered particles from this source can be included in the primary beam without significant loss in accuracy. This assumption reduces unnecessary complexity in the model.

Electrons scattered from the jaws or the FLEC are significant sources and exhibit unique fluence and energy characteristics. Therefore the jaws and the FLEC should be considered as individual radiation sources and modeled analytically.

In total, the electron beam consists of 3 significant sources: (i) primary , (ii) jaws and (iii) FLEC. For the photon beam, the most significant sources were: (i) primary and (ii) FLEC. Since the photon beam contribution to the dose distributions is mainly focused in the Bremsstrahlung tail it was assumed that deriving only the primary photon beam by a fast MC simulation will be adequate as a first approximation.

2.1.4 Primary beam representation

The primary beam consists of particles that originated in any of the components before the jaws and reached the exit plane without interacting with any of the collimating devices. Therefore air scattering is the only interaction occurring during the primary particle transport. Nevertheless, the primary beam fluence distribution shape *varies* according to

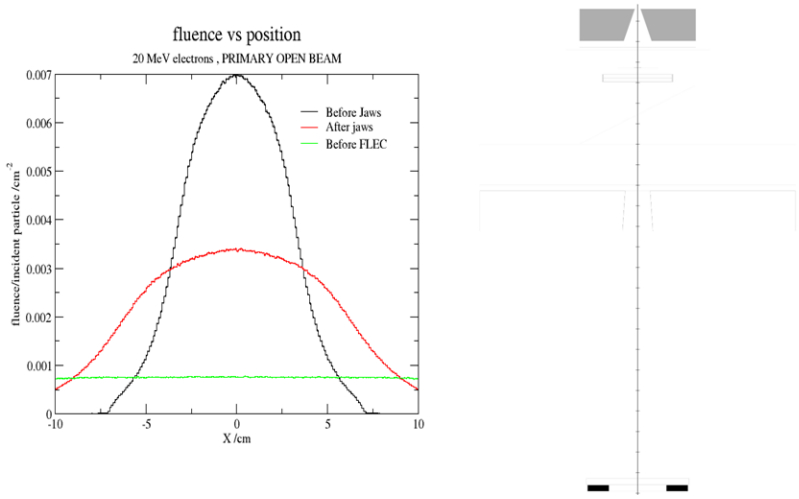

Figure 2.4: *Open electron primary beam: on the left the electron fluence distributions, as they were collected in different levels of the accelerator. On the right, the accelerator model used for the open beam simulations. Jaws and applicator are not present and the electrons are collected before the FLEC.*

the *field size* specified by the collimation devices. The reason for that can be described as follows: considering first the case of an open electron beam (no collimating devices present - figure 2.4) transporting through the accelerator's head, the electron fluence distribution has a gaussian shape at the level before the jaws. As the electrons continue their transportation through the accelerator, the gaussian distribution "opens up", due to air scattering, resulting to an almost completely uniform distribution at the level before the FLEC.

Considering now the case of a collimated open electron beam (only the jaws present - figure 2.5), the gaussian distribution before the level of the jaws is now "cut-off" by the jaws and only particles in the field continue their transport. The distribution will again "open up" due to air scattering, but now there are not enough particles outside the field to create a uniform fluence distribution before the FLEC. The final fluence distribution is uniform in the treatment field and has gaussian shaped "tails" out of the field. The width of these tails depend of the field's shape.

Having described the primary beam "behavior", it can be deduced that the primary beam *can not* be represented in a *field independent* fashion for FLEC-based dynamic deliveries, as long as the *jaws* are used as a *back-up collimation device*. However, since the primary electrons transport only through air, an alternative idea is to perform a *full MC simulation* for the primary beam only. This can be achieved in BEAMnrc by using as

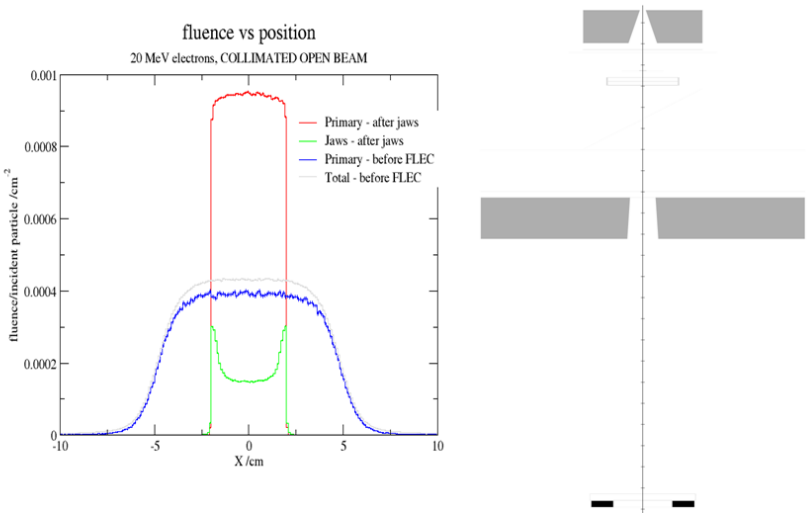

Figure 2.5: *Open collimated electron primary beam: on the left the electron fluence distributions as they were collected in different levels of the accelerator. On the right, the accelerator model used for the open beam collimated simulations. Only the jaws are present (defining a* 9×9 *cm*^{2}*) and the electrons are collected before the FLEC.*

an input ECUT and PCUT values higher than the electron nominal energy in all non-air regions after the secondary collimators (see section 2.1.1- *EGSnrc/BEAMnrc parameters*). Particles reaching a boundary of a collimating device will be immediately rejected and thus their trajectories will no longer be calculated. This is expected to increase significantly the calculation speed.

To increase even further the efficiency, different inputs for the electron algorithm parameters were tested. The objective was to find the optimum combination of the parameter values that will result in a significant increase in speed with only a moderate loss in accuracy. Switching the electron step algorithm from PRESTA-II to PRESTA-I might provide a significant time gain, but the accuracy of the simulations would have to be tested. Switching the Boundary Crossing Algorithm from EXACT to PRESTA would result in electrons transporting on a straight line when reaching a boundary and then introducing multiple scattering as a correction. Switching the Skin Depth for BCA from 3 mfp (default) to 0 mfp, will lead to the default PRESTA algorithm implementation when an electron reaches a boundary.

Another advantage of using a full MC simulation for deriving the primary beam is that the primary photon beam will also be directly reproduced. As it was described in section

2.1.2, photons mainly originate from the scattering foils and the FLEC and contribute to the electron beam dose distributions almost exclusively in the deeper regions. It has been shown from previous studies [44, 49] that simple photon sources are usually adequate for reproducing the Bremsstrahlung tail. Therefore, for this study it was decided to account for the primary photon beam only and neglect the contribution from collimating devices. This assumption reduces the complexity of the model.

The procedure for representing the primary beam can be summarized as follows: first, a fast MC simulation of the accelerator's BEAMnrc model is performed with: (i) electron transport not allowed in non-air regions and (ii) input parameters for the electron algorithms modified in order to increase speed performance. Secondly, the primary electron and photon beams are collected and used directly as an input to the dose calculation engine. The scatter beam contribution will be introduced independently.

2.1.5 Scatter beam representation

As it was discussed in section 2.1.2 and can be seen in Table 2.1, scattered electrons mainly originate from the jaws or the FLEC. The Al frame also contributes significantly but its effect to the beam characteristics in the treatment field can be considered minimal and particles can be included in the primary beam or jaws. A *parameterized scatter beam model* should be able to provide fast acquisition of the scatter beam characteristics, namely the location, energy and direction without significant loss in accuracy.

Two main problems arise in the development of a scatter beam model for modulated electron deliveries: (i) the *incident* beam characteristics on the collimating devices has to be well known. It has been shown in previous work [44], that lacking this information results in large errors in the scatter beam's character. (ii) The scattered beam characteristics have to be reproduced on the exit plane without *a priori* knowledge of the specific field size and shape. This requirement becomes a challenging problem considering that the incident beam on the collimating devices is *field dependent* and thus the scatter beam will also be field dependent.

The model investigated in this work for the scatter beam is based on the idea that each leaf of a collimator (jaws or FLEC) can be considered as an *independent sub-source* and be modeled separately from the rest. Thus, the accelerator is *decomposed* to its individual

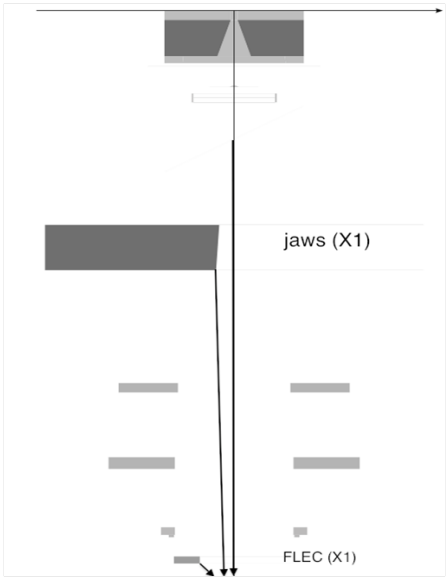

Figure 2.6: *BEAMnrc model with only jaw leaf X1 and FLEC leaf X1 present. The primary beam is properly collimated on the left side of the accelerator and incident on the leaf*

elements. Specifically, the collimators (jaws and FLEC) leaves will be "split" from each other to: Y1 (upper negative leaf), Y2 (upper positive leaf), X1 (lower negative leaf) and X2 (lower positive leaf).

For each independent sub-source/leaf, a full MC simulation is performed for *each* possible leaf *position* and *energy*. Scattered particles from the leaf are collected on the exit plane (back of the FLEC) and the spatial fluence and energy distributions are derived and saved as histograms. These histograms will be referred to as *source scatter kernels* (SSK) in this work.

Isolating elements of the accelerator will result in two problems: (i) the incident beam on each leaf will no longer be correct since it was not collimated properly and (ii) leaf scattered particles that would normally have hit a different leaf during their trajectory and stopped, will now be free to reach the exit plane and erroneously be accounted for in the histograms.

Problem (i) can partially be solved by keeping the corresponding jaw and FLEC leaves in place during the simulation. For example, to derive the SSK for the FLEC X1, the JAW X1 is also kept present during the simulation (figure 2.6). Incident particles on FLEC X1 will now have accurate characteristics since there were collimated properly on that side of the accelerator.

Problem (ii) can be accounted for during the reconstruction phase. Based on an initial estimation of the particle's direction, the particle can be rejected if it is expected to meet any of the rest of the leaves during it's path. Transferring problem (ii) to the reconstruction phase, results in a beam model which is *field independent* during the representation phase.

The general procedure for deriving the SSK can be summarized in the following steps:

1. BEAMnrc models are created with only the corresponding jaw and FLEC leaves present for each possible leaf position (from -4 cm to +4 cm with a step of 1 cm) and each nominal energy (from 6 MeV to 20 MeV). Taking advantage of the accelerator's symmetry, $8 \times 5 = 40$ phase space files are needed to cover all the cases.

2. Full MC simulations are performed for each case. Different LATCH bits are assigned to the jaws and FLEC components.

3. Particles are collected on a 2D fluence grid on the exit plane (back of the FLEC) for each case. The spatial fluence and energy distributions are saved as histograms on the exit plane for each sub-source/leaf (Source Scatter Kernels).

The novelty of the proposed method is that any *arbitrary rectangular* shape field size can be directly reconstructed on the exit plane, by a *superposition* of the corresponding SSKs.

For example, to reconstruct the spatial fluence distribution of the FLEC for an 8×8 cm^2, the following SSK are first loaded (figure 2.7): a. Y1=-4cm, b. Y2=+4cm , c. X1=-4cm and d. X2=+4cm. The superposition of the SSKs results to the reconstructed distribution 2.7e, which can be then compared with the real fluence distribution derived by MC simulation of the full BEAMnrc model 2.7f.

During the reconstruction phase the SSKs will be used as probability distributions for sampling values for the location and energy for the jaws and FLEC scattered particles.

2.1.6 Sampling and reconstruction

Relative Intensity

From the SSKs derived for each leaf a *fluence output factor* is calculated as: $\frac{N^{source\ i}}{N^{original\ source}}$, where $N^{source\ i}$ is the total number of particles counted from source i and $N^{original\ source}$

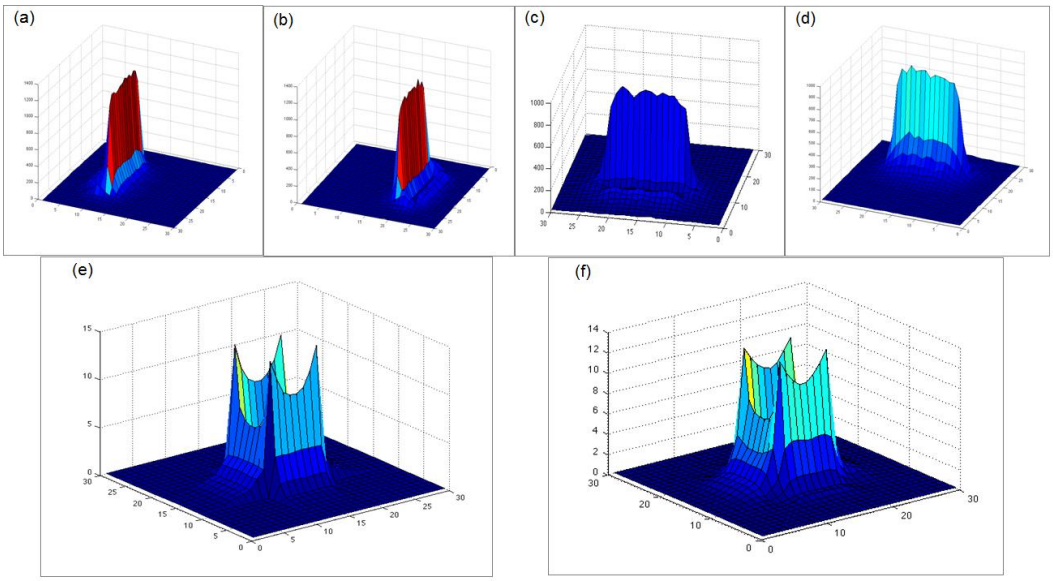

Figure 2.7: *Deriving the Source Scatter Kernels (SSKs) for an* 8×8 cm^2 *field size. FLEC scattered particles are collected on the exit plane for each individual leaf (a. Y1 = -4 cm, b. Y2 = +4 cm, c. X1 = - 4 cm, d. X2= + 4 cm). Superposition of the SSKs will result in a reconstructed fluence distribution (e) which can then directly be compared to the original phase space distribution (f)*

is the number of particles that started from the original source. These output factors are *not* the *correct* final values, since particles that should have been stopped by other leaves have been falsely counted. However, at this point of the reconstruction phase, these output factors are considered correct and later on particles will be rejected based on whether they hit a leaf or not. Based on these fluence output factors, the number of particles to be generated from each source is calculated as:

$$N_{particles} = \frac{N^{source\ i}}{N^{original\ source}} \cdot N_{hist}, \tag{2.2}$$

where N_{hist} is the number of histories asked by the user.

Location

After the number of particles needed from each source has been specified, the fluence distributions are normalized to the maximum value. The normalized fluence distributions are then used as probability distributions to sample the number of scattered particles from the FLEC (N^{FLEC}) and from the jaws (N^{JAWS}) and determine their location (X,Y) on the exit

plane. The sampling is done by a table look-up method. First, the normalized distributions are multiplied by 1000 and rounded to the closest integer. The integer represents the relative intensity of each pixel with an accuracy of 0.1%. An intensity map table is created where the pixel number is assigned to as many elements as the relative intensity integer. For example, if pixel 1 has a relative intensity of 152 (corresponding to 15.2%), then the first 152 elements of the intensity map are assigned the value 1. When a location has to be sampled for a specific particle, a random number is produced from a uniform distribution in the range of [1,length(intensity map)]. The value of the element that corresponds to the random number selected is the pixel which will emit the next particle. The pixel number selected is then converted to (X,Y) coordinates. The final position is selected by a uniform sampling within the pixel.

Energy

Energy distributions have been saved as histograms for each sub-source during the representation phase. The number of bins in each case is determined so that each bin has a width of 0.1 MeV. The table look-up method is used for sampling an energy bin. The final energy is selected by a uniform sampling within the energy bin.

Direction and leaf hits

In contrast with the location and energy, direction can not be sampled directly by known distributions. The main reason for that is that the particle's direction is strongly correlated with it's energy and location [45]. Therefore, the directional distributions have to be reconstructed based entirely on geometrical information. A first estimation of the direction can be made by connecting with a straight line the particle's original position with it's final position on the exit plane. As it has been shown in previous work [43], scattered electrons mainly originate on the leaf's side. Therefore in this study it is assumed that particles are emitted only from the side of a leaf.

The procedure followed can be summarized as follows: first, a uniform sampling on the z axis is performed within the leaf range, in order to determine the Z coordinate of the original position. According to the Z coordinate selected, the Y coordinate (or X coordinate) for the Y pair of leaves (or X correspondingly) is calculated based on the opening selected and

the divergence of the leaves. Then, a gaussian distribution is used for random sampling of the X position (or Y position) for the Y pair of leaves (or X pair of leaves correspondingly). The gaussian distributions have a mean value of 0 and standard deviation dependent on the leaf position. The above information was derived by MC simulations for each leaf position and data analysis of the spatial fluence distributions on the back of each leaf.

The original position is then connected by a straight line with the final position on the exit plane. This serves as an initial estimation of the particle's direction. At this point the *fluence output factors* can be corrected (see 2.1.6/Relative Intensity). If the straight line crosses any of the areas that a leaf would normally be present, then the particle is considered to suffer a *leaf hit*. In such a case the particle is *tagged* in a *leaf hit* table and will not be used as an input to the dose calculation algorithm. The procedure is repeated for all the particles. The *corrected fluence output factor* is given by the equation:

$$N_{particles}^{corrected} = \frac{N^{source\ i} - N_{leaf\ hit}^{source\ i}}{N^{original\ source}} \cdot N_{hist}, \tag{2.3}$$

where $N_{leaf\ hit}^{source\ i}$ is the number of particles from source i that were tagged as leaf hit particles.

The following assumptions are made for this part of the model:

- Electrons are considered to travel on *straight lines*. On the contrary, an electron's trajectory is very sensitive to air scattering. In future work the effect of air scattering should be included for more accurate calculations. The Fermi-Eyges multiple scattering theory can be used for that purpose as it has been described by Jiang et al. (2000) [47].

- Since the straight line approximation is not an accurate method for determining the direction, it is expected that the leaf hit table will not be accurate on a particle-by-particle basis. Nevertheless, the errors should cancel each other out for large samples. It is expected that the corrected output factors should be close to the real values.

2.1.7 Algorithm

The algorithm was implemented in MATLAB 7. The procedure starts with the user asking for N_{hist} histories for a field size F and energy E. The 2D SSKs and fluence output factors have been pre-calculated with MC simulations and saved for each source and leaf. The following pseudo-code describes the procedure as followed by the beam model:

```
For (every source)
 For (every leaf)
  load the fluence and energy SSKs and output factors for field F, energy E;
  Determine number of particles to sample (N_sample = Output * Nhist);
  For i=1:N_sample
   Sample the energy SSK to determine the particle's energy (e);
   Sample the 2D spatial fluence SSK to determine the particle's location (x,y);
   Sample original position on the leaf's edge;
   Connect original with final position to determine direction (u,v);
      if (leaf == JAWS)
        Back-trace the particle to the source;
        If (path == clear)
          return x,y,e,u,v;
        else
          Reject particle;
        end_if
      else_if (leaf == FLEC)
        Backproject the particle to leaf level;
        If (particle overlaps with FLEC leaf)
          Reject particle;
        else
          Return x,y,e,u,v;
        end_if
      end_if
    end_for
  end_for
end_for
```

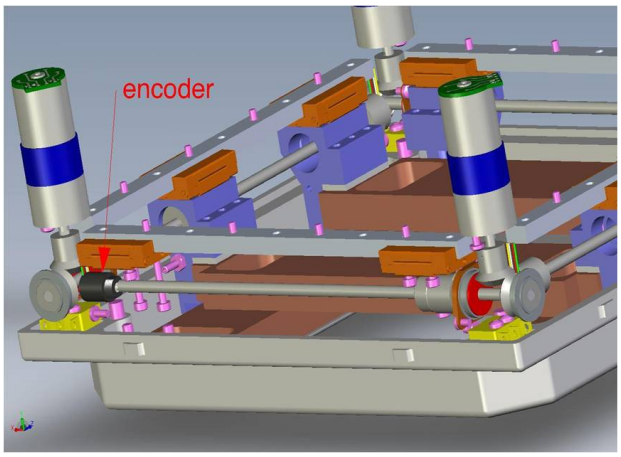

Figure 2.8: *Optical encoders placed directly on the rotation axis. The optical encoders verify that the leaf movement driven by the motors was accurate.*

2.2 Automated motion control: Radiation tolerant solutions for a position feedback device

2.2.1 General

As discussed in sections 1.2.5 and 1.3, the leaf sequence delivered by the FLEC is controlled by stepper motors and optical encoders. The two-phase stepper motor (ARSAPE, Switzerland) is placed on top of the FLEC and is connected to the leaf's rotation axis through a gear system. The motor drives each leaf independently in a series of discrete steps (figure 1.8). One full motor turn corresponds to 240 steps in an open loop operation. The final leaf movement is verified in real time by an optical encoder placed directly on the rotation axis (figure 2.8). Placing the encoders on the axis serves as a way to verify directly the real movement of the axis, irrespectively of the motor movement. 100 pulses produced by the encoder correspond to one full revolution of the axis. One full revolution of the axis corresponds to 1 mm displacement of the copper leaf. Therefore, if a move of 1 mm is asked by the controller, but the encoder produces a number of pulses different than 100, then an error occurs and the leaf sequence automatically stops.

Even though CMOS based optical encoders are very efficient position feedback devices, their radiation tolerance is very poor (Table 1.1). Therefore their use on an electron collimator exposed to high radiation doses during the beam delivery is not recommended. In this work two approaches were investigated for implementing a radiation tolerant position

Material	Atomic number (Z)	Thickness (cm)	CSDA ($\frac{gr}{cm^2}$)	CSDA (cm)
Polyethylene	5.3	9.6	9.157	9.95
Lucite Water	6.2	9.0 - 9.5	9.69	8.14
Al	13	4.5 - 5	10.56	3.91
Cu	29	1.5 - 2	10.43	1.17
W	74	1.5 - 2	9.78	0.51
Pb	82	1.5 - 2	9.339	0.82

Table 2.3: *Physical characteristics of the materials tested for shielding the optical encoders. CSDA ranges and atomic composition acquired by the National Institute of Standards and Technology.*

feedback system: (i) Introduce a protective shield over the area where the optical encoders reside and (ii) replace the optical encoders with an analog position feedback device which has a higher radiation dose tolerance. In the following sections the procedure followed in both approaches will be presented.

2.2.2 Shielding the optical encoders

As it can be seen in figure 2.8, the encoders reside on the rotation axis approximately 1 cm above the FLEC leaf and 7 cm away from the beam's central axis. In order to determine the optimum shielding design for the encoders, Monte Carlo simulations were performed using the BEAMnrc/EGSnrc code. The first objective was to determine the optimum material to be used for the shield. For that purpose, slabs of different materials were placed between the 2nd applicator scraper and the FLEC in the BEAMnrc model and full MC simulations were performed. The collective area was a linear strip of 1 cm width at the encoder's level. The materials tested, along with their atomic number, selected thickness and maximum CSDA range (for 20 MeV) are shown in table 2.3. Even though higher atomic number materials are commonly used for shielding purposes (since they limit the electron range) they also result to increased X-ray production. For that reason lower atomic number materials were also tested such as Polyethylene, Lucite Water (PMMA) and Al. The material thickness was chosen so that it would exceed at least the CSDA range and be easily manufactured. Polyethylene was the only case that the thickness could not reach the CSDA range, since

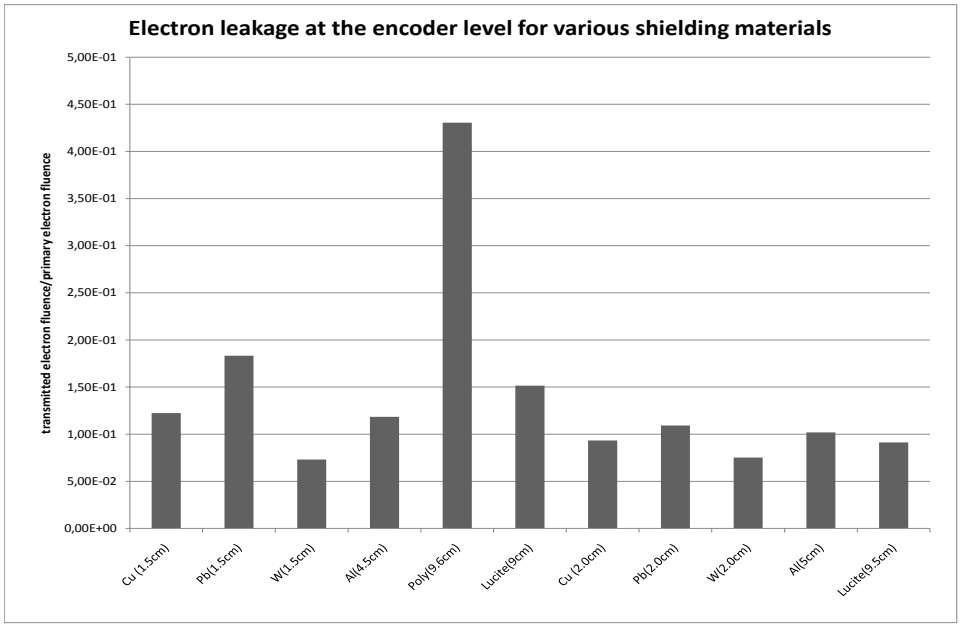

Figure 2.9: *Electron leakage fluence for various shielding materials. Slabs of the materials are placed on top of the FLEC frame to protect the optical encoders.*

the maximum available distance between the second scraper and the FLEC frame was 9.6 cm.

Figures 2.9 and 2.10 show the calculated transmitted electron and photon fluence through the shielding slab normalized to the incident fluence. From the results the following can be deduced:

- W was the best case showing the least amount of leakage radiation for both electron and photon fluences.
- Cu (2 cm) was the second best case for reducing the electron fluence leakage, but exhibited increased photon fluence leakage.
- Lucite water (9.5 cm) exhibits similar electron leakage with Cu, but with reduced photon leakage.
- Polyethylene (9.6 cm) exhibited very high electron leakage, since the thickness was less than the CSDA range.

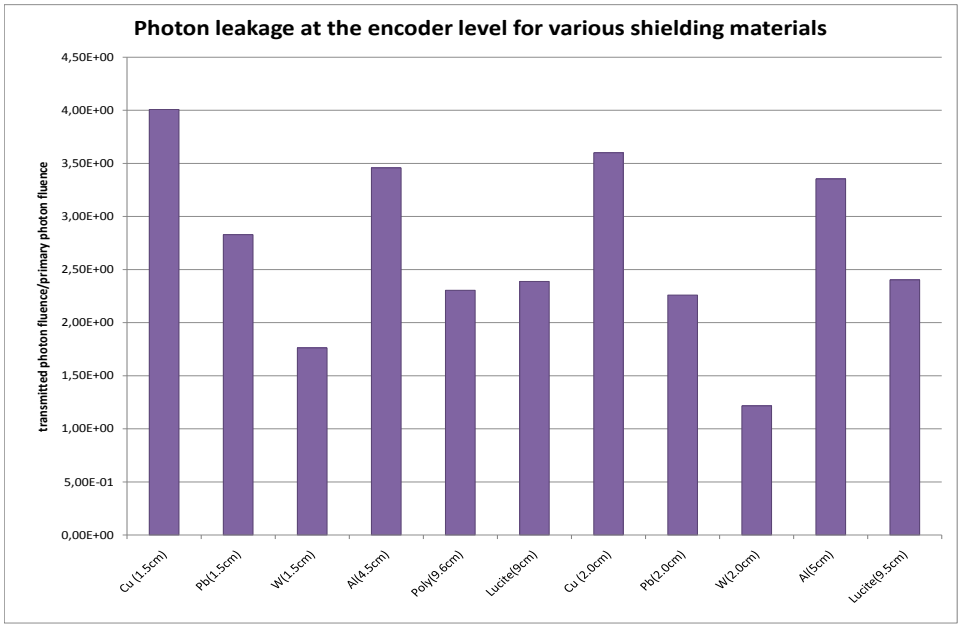

Figure 2.10: *Photon leakage fluence for various shielding materials. Slabs of the materials are placed on top of the FLEC frame to protect the optical encoders.*

- Al and Pb were intermediate cases.

While tungsten is the best choice for shielding purposes, it would also increase significantly the weight of the FLEC. Since reducing the electron leakage fluence is our major concern (dose deposited per electron travelling is three orders of magnitude higher compared to the dose per photon), Cu was chosen as the most appropriate material. Lucite water could have been an alternative, but the thickness of 9.5 cm would create practical problems and would cancel out the advantage of having an add-on device.

At the next step a more realistic model of the shield was implemented in BEAMnrc (figure 2.11). The shield was designed as an extra scraper placed on top of the FLEC frame (4 cm above the leaves). An extra side-shield was also introduced, to reduce the scattered lateral electron fluence to the encoders.

In order to determine the optimum face and side thickness for the shield, detailed Monte Carlo simulations of the model were performed with the shield present. The electron and photon fluences were recorded at the encoder site for thicknesses of 1.2 - 2.0 cm and energy of 20 MeV for the face part shield (worst case of transmission leakage) and for

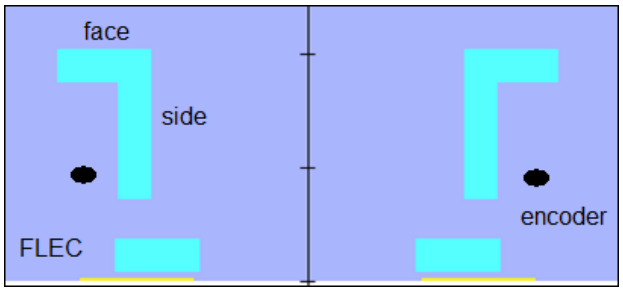

Figure 2.11: *The BEAMnrc model of the shield designed to protect the encoder site (black dot). The shield is placed as an extra scraper above the FLEC and consists of a face shield (for reducing direct transmitted electrons) and a side shield (for reducing lateral scattered electrons).*

.

thicknesses of 0.5 - 1.2 cm and energy of 6 MeV for the side part of the shield (worst case of lateral scattered leakage). Simulations were performed with 10^8 histories and field size set to maximum opening (8×8 cm^2). Figures 2.12 and 2.13 show the electron fluences as recorded at the encoder site.

From the results it can be seen that increasing the face thickness of the shield above 1.2 *cm* (CSDA range) *did not* result in any significant changes of the electron leakage fluence (figure 2.12) . However, increasing the side thickness from 0.5 to 1.2 cm, resulted in a reduction of 63% to the electron fluences (figure 2.13). Photon fluences were also reduced by up to 28%. Therefore, the final design of the shield had a thickness of 1.2 cm for both face and side thicknesses.

Figure 2.14 shows the prototype Cu shield that was manufactured at the Montreal General Hospital. Measurements were taken at the encoder's site with and without the shield. A Farmer type ionization chamber was used for the measurements. The purpose of the measurements was to verify whether the prototype shield would be adequate in significantly reducing the dose to the encoders.

Besides recording the dose at the encoder site with the shield, another matter of interest was what type of particles contribute more significantly to the dose at the encoder site when the shield is present. This could potentially indicate how to improve the shield design. In order to separate the electron from the photon contribution to the dose, an Al build-up cap was used on the ion chamber. The maximum electron energy at the encoder's site for

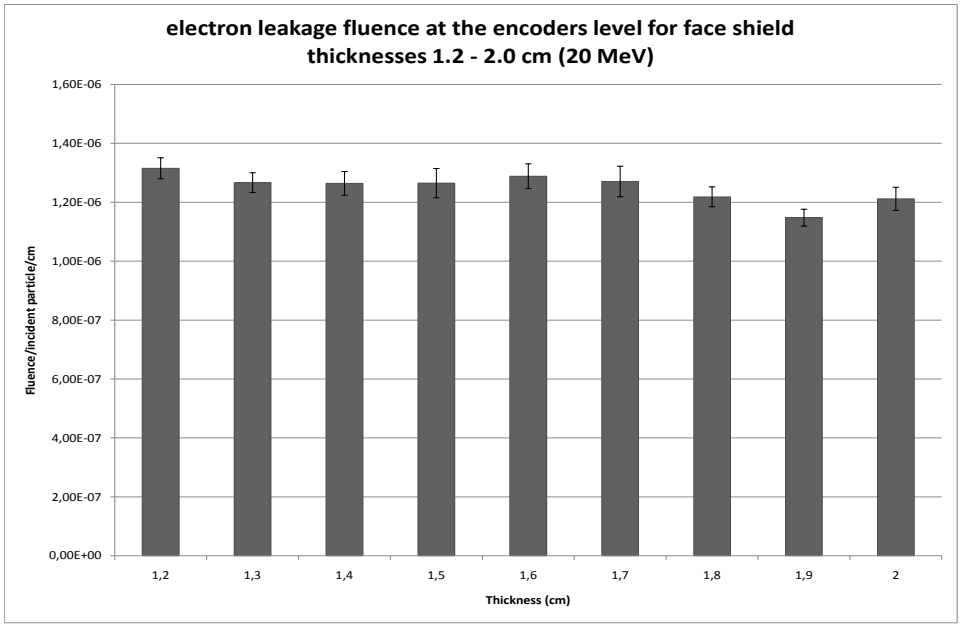

Figure 2.12: *Electron leakage fluence at the encoder site for 20 MeV electron beams. Extra scrapper shield was introduced and various face thicknesses were tested.*

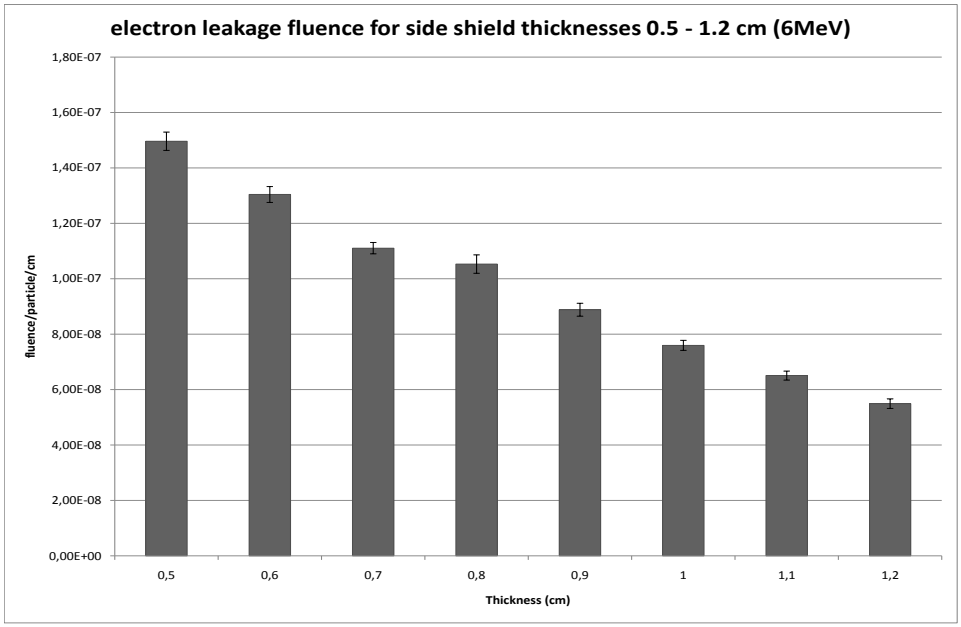

Figure 2.13: *Electron leakage fluence at the encoder site for 6 MeV electron beams. Extra scrapper shield was introduced and various side thicknesses were tested.*

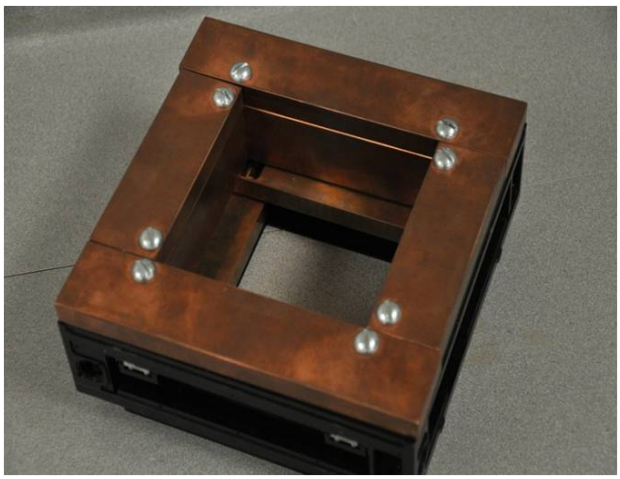

Figure 2.14: *Prototype shield for the FLEC.*

nominal energy of 20 MeV was found by MC simulations to be 6 MeV. Therefore the Al cap was build with a radius of 1.4 cm (CSDA range of 6 MeV electrons) in order to block all external electrons. Since Al has a low atomic number ($Z = 13$) and it's thickness is relatively small, it was assumed that the photon fluence should remain approximately the same. Thus, the measurement with the Al cap should indicate the approximate dose from the photon component of the beam. To investigate the possibility of reducing even further the dose at the encoder site, a Pb cap was manufactured with a radius of 2 cm to cut-off the residual photon beam component. The radius of 2 cm was chosen taking into account the space limitations at the site. In chapter 3 the results from the measurements will be presented and discussed.

2.2.3 Analog position feedback device

As it was discussed in sections 1.3 and 2.2 optical encoders fail to operate in a radiation environment due to the fact that they include CMOS type transistors in their circuits. An analog position feedback device, such as a potentiometer, could be an alternative solution since the radiation tolerance for such devices is significantly higher. Figure 2.15 is a sketch of a simple set-up using a potentiometer as a position feedback device. The encoder is also shown in the sketch to indicate the relative position of the potentiometer. In the actual set-up the encoders were not used.

The potentiometer is directly connected on the rotation axis (lead screw). When a leaf movement occurs, the axis rotates directly the potentiometer causing a voltage drop at the

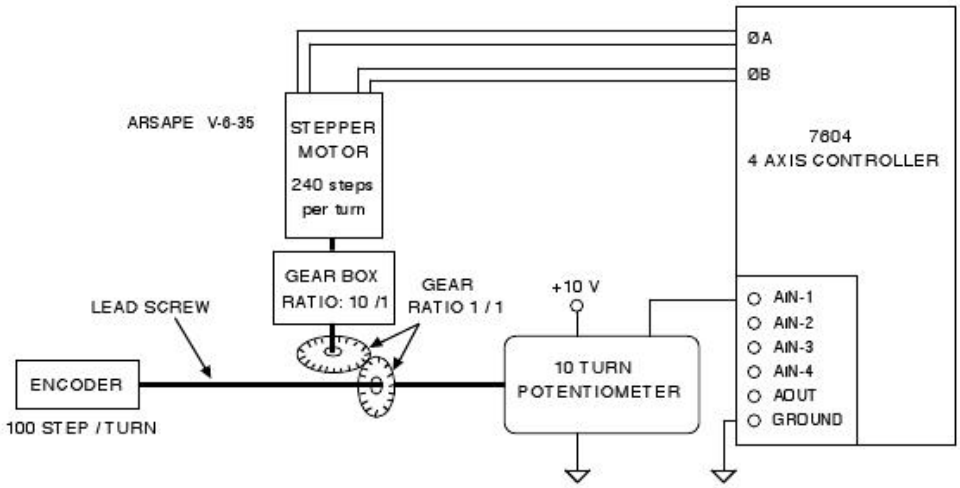

Figure 2.15: *Sketch of the operation of an analog position feedback*

output. The voltage drop is then used as an input to a 12-bit Analog to Digital Converter (ADC) that resides in the controller. The ADC converts the voltage drop to a number of discrete states. For a 12-bit ADC, $2^{12} = 4096$ discrete states exist.

Lets assume that the potentiometer is set to a reference voltage of 10 V (which means that it can provide 0-10 V range) and each full turn corresponds to 1 V change. That means that the 4096 states (0-4095) are distributed across a 10 V range giving approximately 409 ADC steps/volt. A 1 mm leaf movement will then correspond to 1 full revolution or 1 V change of the potentiometer which will be translated to a change of 409 discrete states to the ADC.

The user has to specify to the controller the number of ADC steps and motor steps that correspond to one full revolution. The selection serves as a calibration of the controller to associate the ADC value to the real axis movement. Furthermore, the ADC steps/revolution depends of the voltage to revolution ratio which can be seen as the system's resolution. Since the voltage range is limited (usually up to 10 V), the longer the distance to be covered, the worse the resolution will be and consequently the worse the performance of the feedback device. This is one of the main reason why optical encoders are usually preferred as feedback devices. In chapter 3 the performance of such a system will be presented for the needs of controlling the FLEC leaves.

Chapter 3

Results

3.1 Beam model

3.1.1 General

In this section the parameterized, MC-based beam model for FLEC-based MERT deliveries will be tested against full MC simulations of the validated BEAMnrc accelerator model. The primary and scatter beam depth and profile dose distributions will be compared and discrepancies will be discussed. In order to validate fully the beam model, the results will be presented for the largest (8×8 cm^2) and smallest (2×2 cm^2) field openings, as well as for the highest (20 MeV) and lowest (6 MeV) nominal energies. A rectangular field size of 2×8 cm^2 will also be presented to validate the capability of the model to reproduce arbitrary rectangular field sizes. Furthermore, the performance of the model in calculation speed, fluence and dose output prediction will be presented. The following should be noted regarding the parameters set at the MC simulations:

- The number of histories varied from $7 \cdot 10^8$ up to 10^9. In each case the number of histories was selected so that the depth and profile dose distributions for the total beam will have an accuracy of 1% or better.

- Unless otherwise stated in the following sections, the electron step algorithm was set to PRESTA - II, the Boundary Crossing Algorithm (BCA) was set to EXACT, the Skin Depth for BCA parameter was set to 3 mean free paths and the electron and photon cut-off values were set to ECUT=0.7 MeV and PCUT=0.01 MeV respectively

(see section 2.1.1/BEAMnrc/EGSnrc parameters).

- Varying electron range rejection (ECUTRR) was used in all cases with ESAVE=2 MeV (see section 2.1.1/BEAMnrc/EGSnrc parameters). No other variance reduction technique was used for the full MC simulations.

- The dose distributions were calculated using the DOSXYZnrc code in a homogeneous water phantom with a voxel size of $5 \times 5 \times 5\ mm^3$.

3.1.2 Primary beam

As it was described in section 2.1.4, the primary beam component is derived by a fast, full MC simulation of the electron beam transporting only through air in the accelerator. To achieve that the electron cut-off value (ECUT) was set to a higher value than the maximum particle energy for all non-air regions. Thus, all the electrons reaching a boundary of a non-air region are immediately rejected. The photon beam cut-off value (PCUT) was kept to its default value (PCUT=0.01 MeV) so that all the Bremsstrahlung photons are included to the primary beam. Furthermore, the following EGSnrc parameters were modified from their default values to increase the speed of the calculations: Boundary Crossing Algorithm (BCA) from EXACT to PRESTA and Skin Depth for BCA (SD) from 3 mfp to 0 mfp. In total 3 new fast models were created for deriving the primary beam characteristics on the exit plane of the linear accelerator:

- *Fast model 1 (HighECUT):* Full model with BCA=EXACT, SD=3 mfp and ECUT higher than the maximum particle's energy.

- *Fast model 2 (PRESTA-I & SD=3):* Same as previous, but with BCA=PRESTA-I.

- *Fast model 3 (PRESTA-I & SD=0):* Same as previous, but with SD=0.

It should be noted that changing the electron step algorithm from PRESTA-II to PRESTA-I *did not* show any significant change in the calculation speed. Therefore it was not considered as an option, since it would lead to unnecessary loss of accuracy.

Figures 3.1 and 3.2 show the primary beam dose distributions for 6 MeV and 20 MeV and field sizes of 8×8 and $2 \times 2\ cm^2$ for the full Monte Carlo and for the fast models.

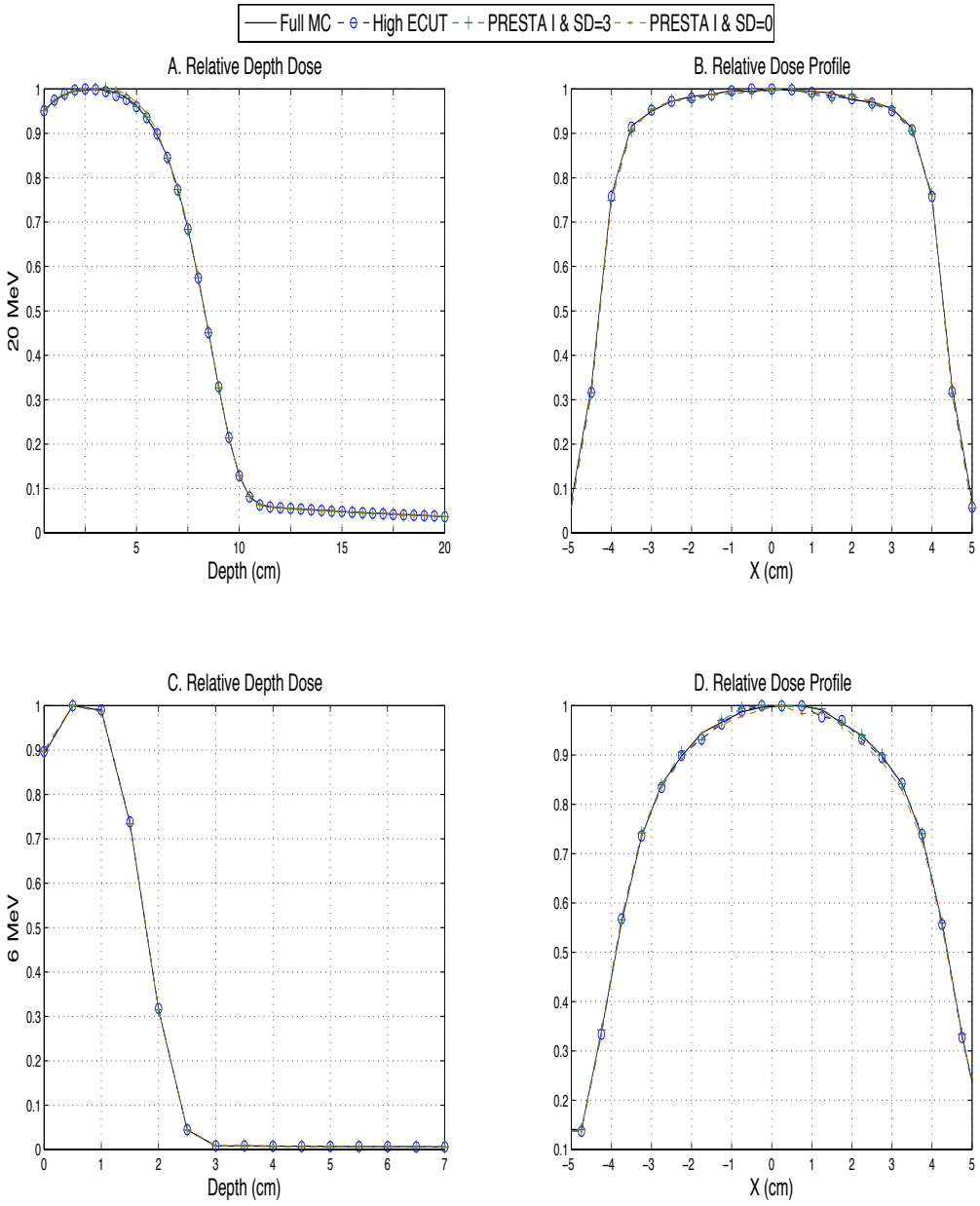

Figure 3.1: *Primary beam depth and profile dose distributions for energies of 20 MeV (A and B) and 6 MeV (C and D) and field size of* 8×8 cm^2. *4 models are tested: Full Monte Carlo (black solid line), Fast model 1 - High ECUT (circle/blue line), Fast model 2 - PRESTA I (cross/green line) and Fast model 3 - PRESTA I and SD=0 (dot/orange line)*

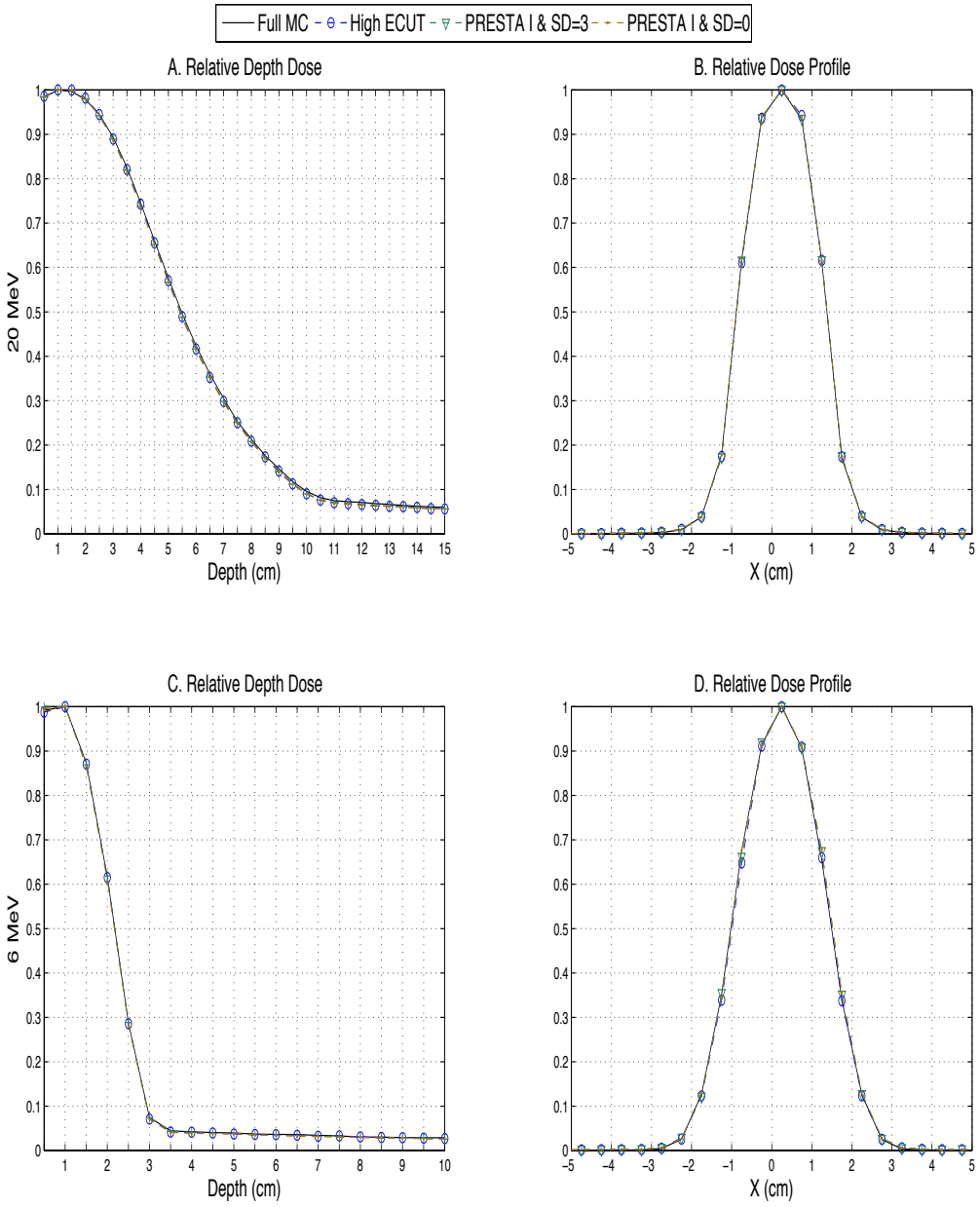

Figure 3.2: *Primary beam depth and profile dose distributions for energies of 20 MeV (A and B) and 6 MeV (C and D) and field size of* 2×2 *cm*^{2}. *4 models are tested: Full Monte Carlo (black solid line), Fast model 1 - High ECUT (circle/blue line), Fast model 2 - PRESTA I (cross/green line) and Fast model 3 - PRESTA I and SD=0 (dot/orange line)*

	$8 \times 8\ cm^2$		$2 \times 2\ cm^2$	
Model	20 MeV	6 MeV	20 MeV	6 MeV
Full MC	1	1	1	1
High ECUT	×4.1	×4.6	×9.9	×9.4
PRESTA I and SD=3	×6.8	×7.2	×14.3	×13.2
PRESTA I and SD=0	×19.6	×16	×22.6	×16.1

Table 3.1: *Relative speed performance (number of times faster) for the primary beam using different models. Normalization to the full Monte Carlo model.*

Excellent agreement is shown between the full MC and the fast models with a mean error of less than 0.5% and max error in a voxel less than 1% in every case. Switching the BCA from EXACT to PRESTA I and the SD from 3 to 0 did not show any significant discrepancies, even for the smallest field size and energy.

Table 3.1 shows the relative calculation time (number of times faster) for each model compared to the full MC simulation. Fast model 1 (High ECUT) presented an increase to speed up to an order of magnitude. Fast model 2 (BCA=PRESTA-I) was up to 14.3 times faster than the full MC simulation. Switching the Skin depth for BCA parameter to 0 mfp (fast model 3) resulted to a time gain up to a factor of 22.6.

3.1.3 Scatter beam

The method is based on decomposing the accelerator's collimating devices to it's individual leaf components and consider them as independent sub-sources. For each sub-source, scatter fluence and energy kernels are derived on the exit plane of the accelerator. The output fluence is also derived for each sub-source. The source scatter kernels (SSKs) are then sampled for deriving a location and energy for each particle. Direction is estimated by a straight line approximation between the original and final position. According to the estimated direction, a particle is rejected if it can be seen that it would experience a leaf hit at some point during it's trajectory. Thus, a corrected output fluence can be derived after the leaf hit correction. At the end of the procedure a phase-space file is created with the location (X,Y), energy (E) and direction (U,V) of each particle. This reconstructed phase-space file can then be used directly as an input to a dose calculation engine and derive dose

Scatter fluence output= $\frac{N^{sub-source}}{N^{original\quad source}}$ ($\times 10^{-4}$)

Source	Full MC		No correction		After correction	
	20 MeV	6 MeV	20 MeV	6 MeV	20 MeV	6 MeV
$8 \times 8 \quad cm^2$						
JAWS	45	12	78	35	44	14
FLEC	48	6.7	112	15.1	52	8.1
$2 \times 2 \quad cm^2$						
JAWS	3.7	1.3	64	28	5.9	2.4
FLEC	7.2	0.54	79	14.3	12	2.8

Table 3.2: *Scatter fluence output factors (on the exit plane) for field sizes of* 8×8 cm^2 *and* 2×2 cm^2 *and energies of 20 MeV and 6 MeV. The output of each sub-source is presented as derived by full MC (column 2), beam model with no leaf hit correction (column 3) and beam model after applying the leaf hit correction (column 4).*

distributions for that specific sub-source. The procedure for deriving and reconstructing the scatter beam component has been described in detail in sections 2.1.4/*Scatter beam representation* and 2.1.5/*Sampling and reconstruction.*

Scatter output fluence

Table 3.2 presents the output fluence ($\frac{N^{sub-source}}{N^{original\quad source}}$) for each sub-source as predicted by full MC simulations and by the beam model without and with the leaf hit correction. If no correction is applied to the scatter kernels the output factors are significantly overestimated. For the largest field size (8×8 cm^2), the output was overestimated by the beam model up to 2.3 times of the MC calculated value. For the smallest field size (2×2 cm^2) the discrepancy was even more significant, with the worst case (field size: 2×2 cm^2, energy: 6 MeV) being up to 29 times higher than the full MC calculation. After the leaf hit correction algorithm is applied, the fluence output factors reach a better agreement with the MC calculated values. For the largest field size, the fluence output is overestimated up to 0.17 times of the MC value, while for the smallest field size an overestimation up to 4.18 times was noticed for the lowest energy. In all cases, the lowest energies and field sizes exhibited the most severe discrepancies, while the FLEC was the sub-source that showed the most difficulty

Mean energy, $\bar{E}$(MeV)								
	$8 \times 8 \quad cm^2$				$2 \times 2 \quad cm^2$			
	Full MC		Source Model		full MC		Source Model	
Sources	20 MeV	6 MeV	20 MeV	6 MeV	20 MeV	6 MeV	20 MeV	6 MeV
JAWS	18.2	6.2	16.9	5.7	16.5	5.6	16.7	5.6
FLEC	8.7	4.4	8.8	4.1	7.5	3.8	8.2	4.0

Table 3.3: *Mean particle energy as predicted by the full MC simulation and by the source model for the sub-sources JAWS and FLEC and energies of 20 MeV and 6 MeV*

in matching with MC calculated values.

Figures 3.3 and 3.4 exhibit the spatial fluence profiles of the sub-sources JAWS and FLEC as they appear on the exit plane of the linear accelerator, on the back of the FLEC, for field sizes of 8×8 and 2×2 cm^2 as they are predicted by the full MC simulations and the beam model. The beam model exhibits excellent agreement with the full MC case in the treatment field. Taking into account the relative intensities of the sub-sources (see Table 2.1), the accuracy is better than 1% in all cases. As we move to the penumbra area the dicrepancies become more significant. Specifically in the region next to the FLEC leaves, an overestimation of the particle fluence is apparent in almost all cases by the beam model. The effect is more dominant for the lowest energy (6 MeV) where it reaches a maximum difference of 35.7% for the JAWS and of 31% for the FLEC. However, relative to the total intensity of the beam, these maximum deviations end up to be 2.5% and 3.8% respectively.

Mean energy

Table 3.3 shows the mean particle energy for each sub-source as predicted by the full MC simulation and by the source model. For the largest field size (8×8 cm^2) the source model tends to underestimate the mean energy up to 1.3 MeV (sub-source: JAWS, energy: 20 MeV) compared to the full MC case. For the smallest field size (2×2 cm^2) the opposite effect is observed with an overestimation of the mean energy up to 0.7 MeV (sub-source: FLEC, energy: 20 MeV). In general, higher beam energies exhibit larger discrepancies than lower energies. Sub-source JAWS exhibits the larger deviations for a field size of 8×8 cm^2,

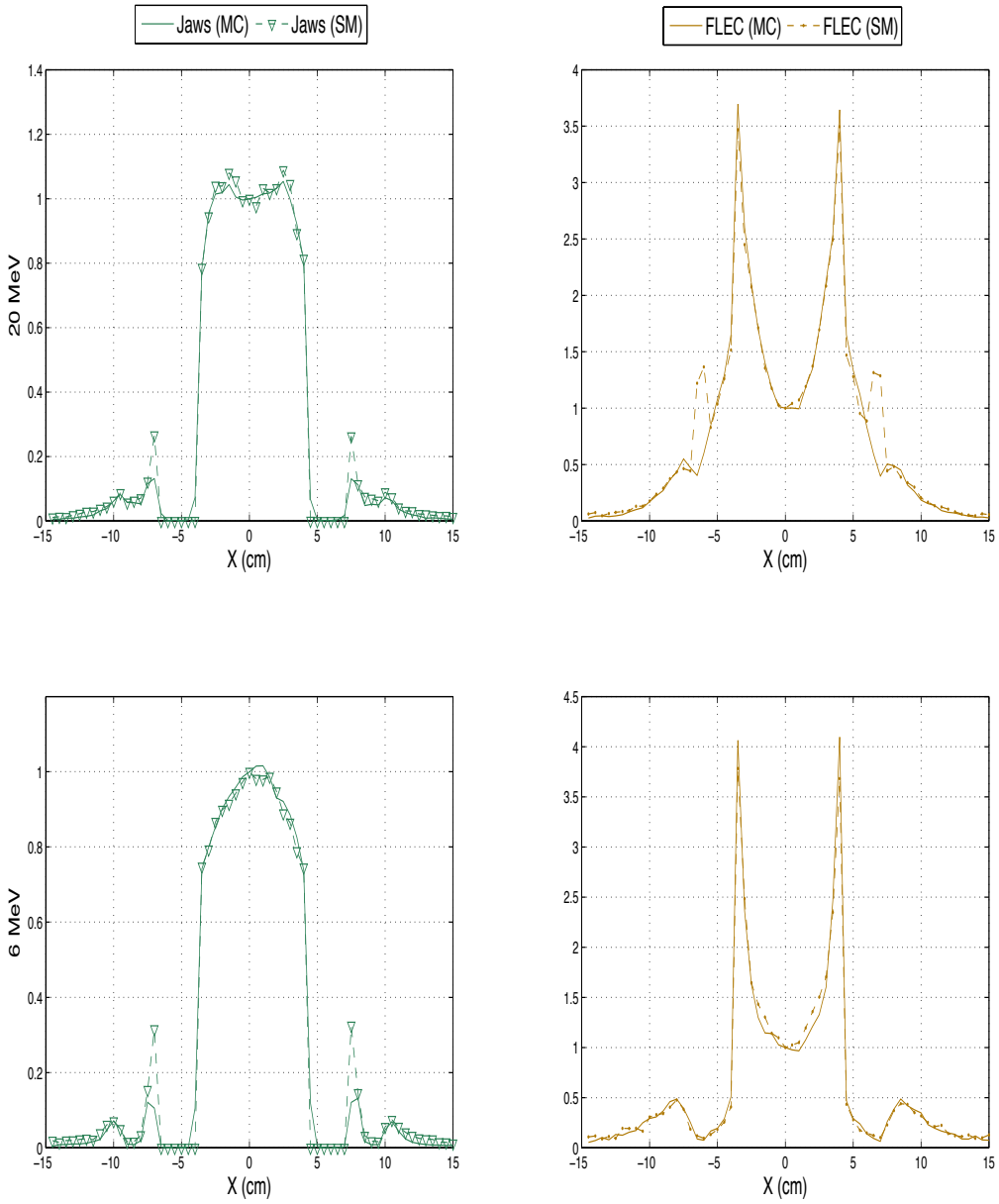

Figure 3.3: *Scatter source fluence profiles, as they appear on the exit plane of the accelerator, for field sizes of* 8×8 cm^2 *and energies of 20 MeV and 6 MeV. Full MC calculations (solid lines) are compared with the source model calculations (dotted lines) and normalized to the central axis. JAWS are represented by the green lines/triangles and FLEC by the orange line/dots*

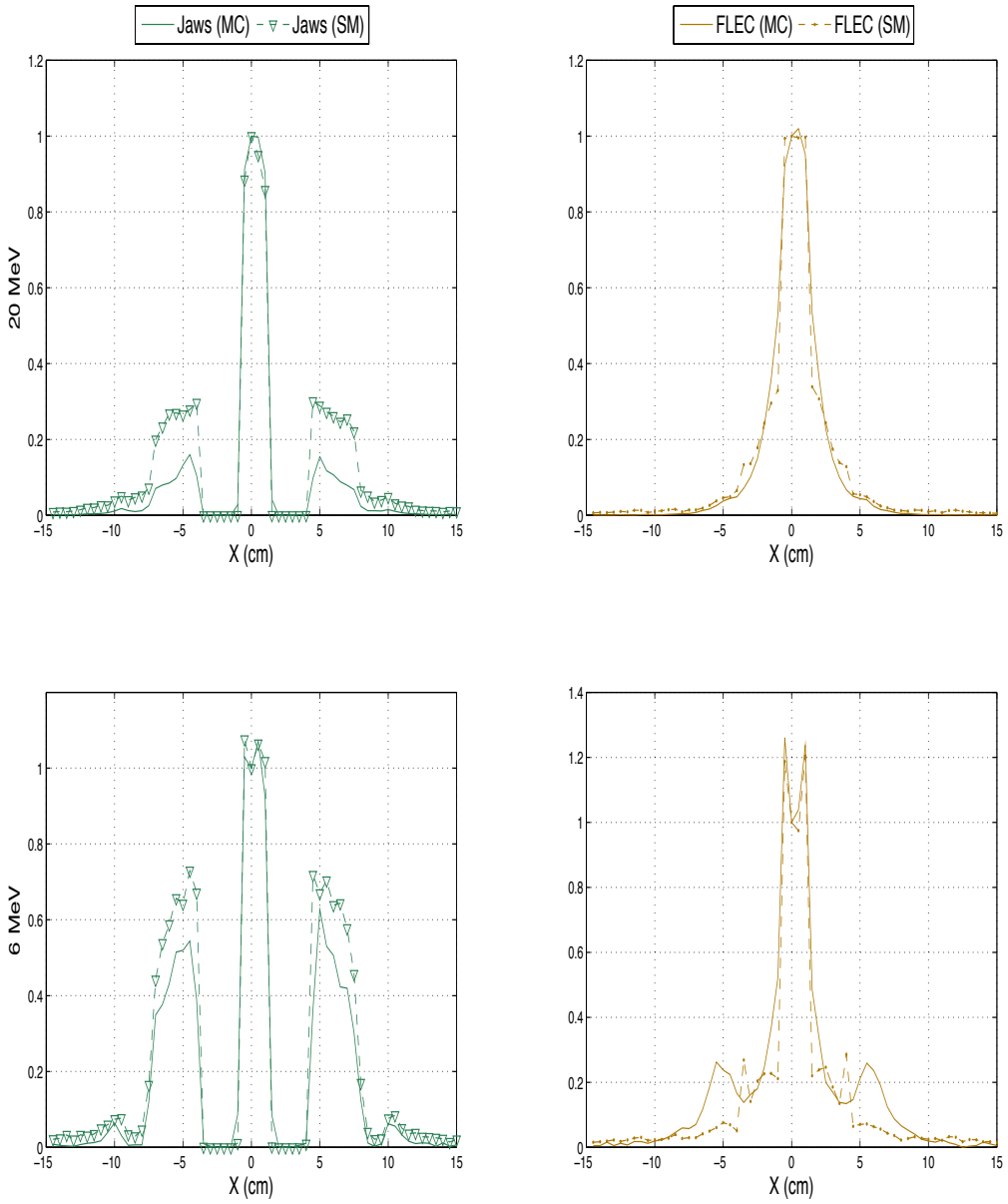

Figure 3.4: *Scatter source fluence profiles, as they appear on the exit plane of the accelerator, for field sizes of* 2×2 cm^2 *and energies of 20 MeV and 6 MeV. Full MC calculations (solid lines) are compared with the source model calculations (dotted lines) and normalized to the central axis. JAWS are represented by the green lines/triangles and FLEC by the orange line/dots*

while sub-source FLEC showed larger discrepancies for a field size of 2×2 cm^2.

3.1.4 Dose distributions

In this section the primary and scatter depth and profile dose distributions are presented for energies of 20 MeV and 6 MeV and field sizes of 8×8 cm^2, 2×2 cm^2 and 2×8 cm^2. The sub-sources dose distributions are summed together and normalized to the maximum dose to show the predicted normalized depth and profile dose distribution of the total beam. In the same manner, the MC derived dose distributions are presented in the same graph. Solid lines correspond to the full MC simulations and dotted lines/symbols to the source model. The primary beam component for the source model was derived according to the method presented in section 3.1.2, which had shown an accuracy better than 0.5% with the MC simulation. Therefore, discrepancies seen in the primary beam dose distributions are exclusively based on variations of the scatter component which affect the normalization to the total dose.

Largest field size (8×8 cm^2)

Figure 3.5 exhibits the dose distributions for the largest field size of 8×8 cm^2. From the results the following can be deduced:

- The FLEC sub-source exhibits good agreement with the full MC simulation reproducing the dose distributions shape in both the surface and the deeper regions.
- The JAWS sub-source reproduced the dose distributions shape, but the relative contribution is *underestimated* compared to the full MC.
- The total depth dose distribution exhibits very good agreement with a mean error less than 1% for both 20 MeV and 6 MeV. The maximum error encountered in a voxel was 2.1% (for 20 MeV) and 2.1% (for 6 MeV).
- The total profile dose distribution exhibits a mean error of less than 1% for both 20 MeV and 6 MeV. The maximum error encountered in a voxel was 2.4% (for 20 MeV) and 2.0% (for 6 MeV).

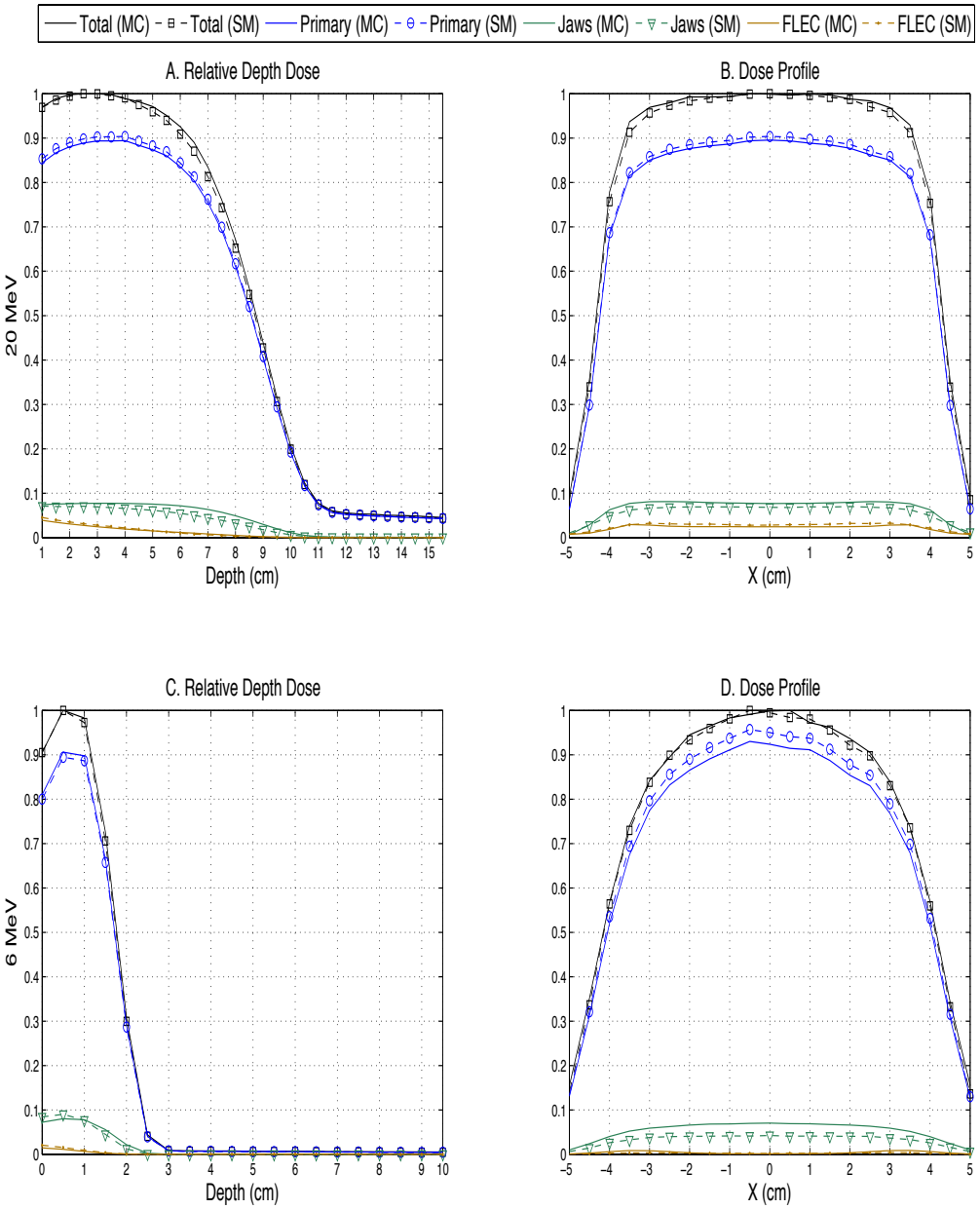

Figure 3.5: *Depth and profile dose distributions for a field size of* 8×8 cm^2 *and energies of 20 MeV (A and B) and 6 MeV (C and D). Solid lines represent the full MC simulation results, while dotted lines/symbols represent the source model predictions.*

Smallest field size ($2 \times 2\ cm^2$)

Figure 3.6 exhibits the dose distributions for the smallest field size of $2 \times 2\ cm^2$. From the results the following can be deduced:

- The FLEC sub-source exhibits discrepancies especially in the build up region. The relative dose is *overestimated* by the source model.
- The JAWS sub-source reproduces the distribution shape, but underestimates the relative dose. The effect is more pronounced for the lowest energy of 6 MeV.
- The total depth dose distribution exhibits a mean error of less than 1% for both 20 MeV and 6 MeV. The maximum error encountered in a voxel was 2.1% (for 20 MeV) and 6% (for 6 MeV).
- The total profile dose distribution exhibits a mean error of less than 1% for both 20 MeV and 6 MeV. The maximum error encountered in a voxel was 3% (for 20 MeV) and 1.6% (for 6 MeV).

Irregular field size ($2 \times 8\ cm^2$)

Figure 3.7 exhibits the dose distributions for the smallest field size of $2 \times 8\ cm^2$. From the results the following can be deduced:

- The FLEC sub-source exhibits an *overestimation* of the relative dose in the build up region such as in the case of a $2 \times 2\ cm^2$. The effect is more pronounced for 6 MeV.
- The JAWS sub-source exhibits an *underestimation* of the relative dose, especially for the lowest energy.
- The total depth dose distribution exhibits a mean error of less than 1% for both 20 and 6 MeV. The maximum error encountered in a voxel was 2.5% (for 20 MeV) and 3.6% (for 6 MeV).
- The total profile dose distribution exhibits a mean error of less than 1.3% for both 20 MeV and 6 MeV. The maximum error encountered in a voxel was 1.6% (for 20 MeV) and 4% (for 6 MeV)

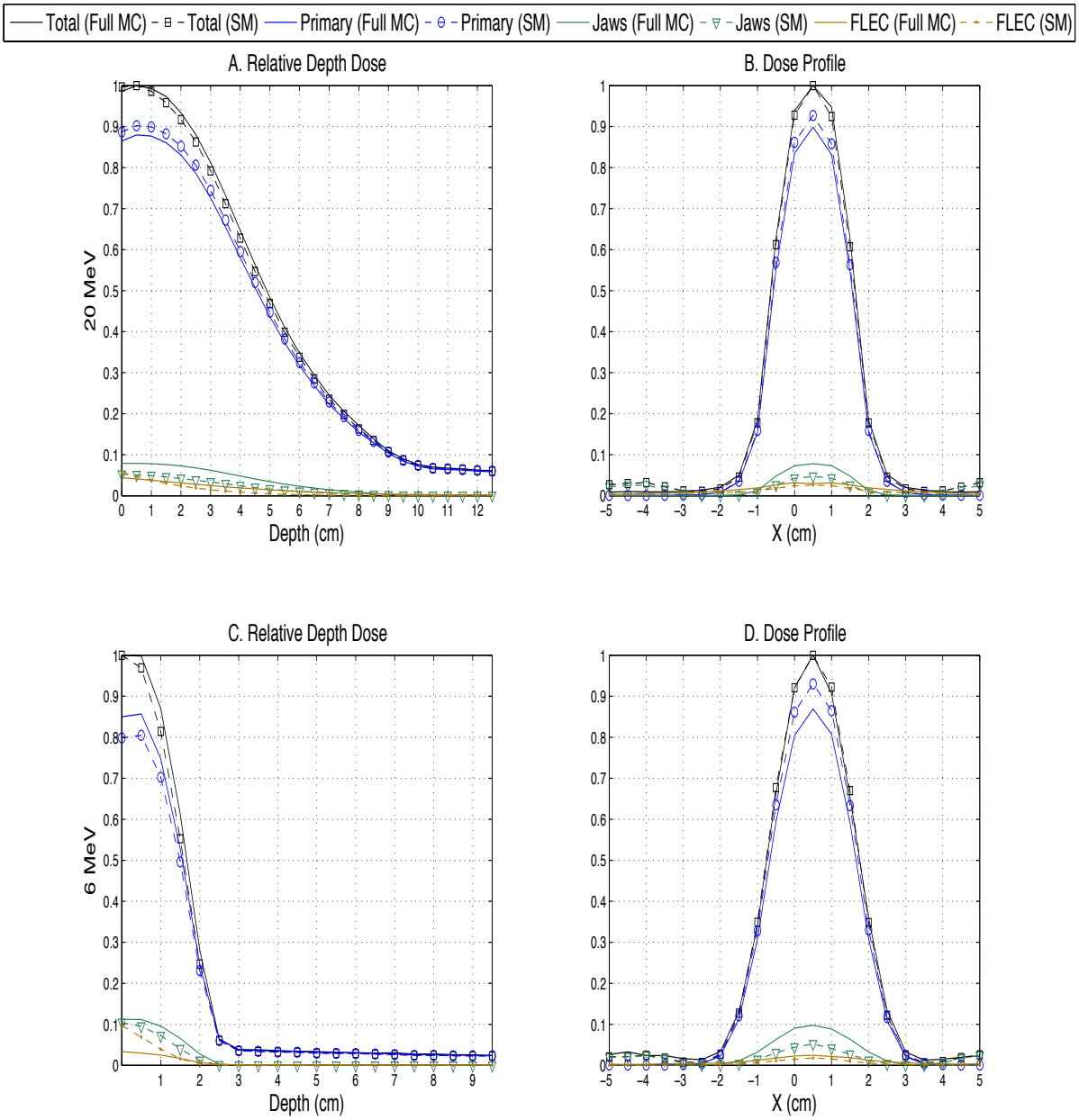

Figure 3.6: *Depth and profile dose distributions for a field size of* 2×2 cm^2 *and energies of 20 MeV (A and B) and 6 MeV (C and D). Solid lines represent the full MC simulation results, while dotted lines/symbols represent the source model predictions.*

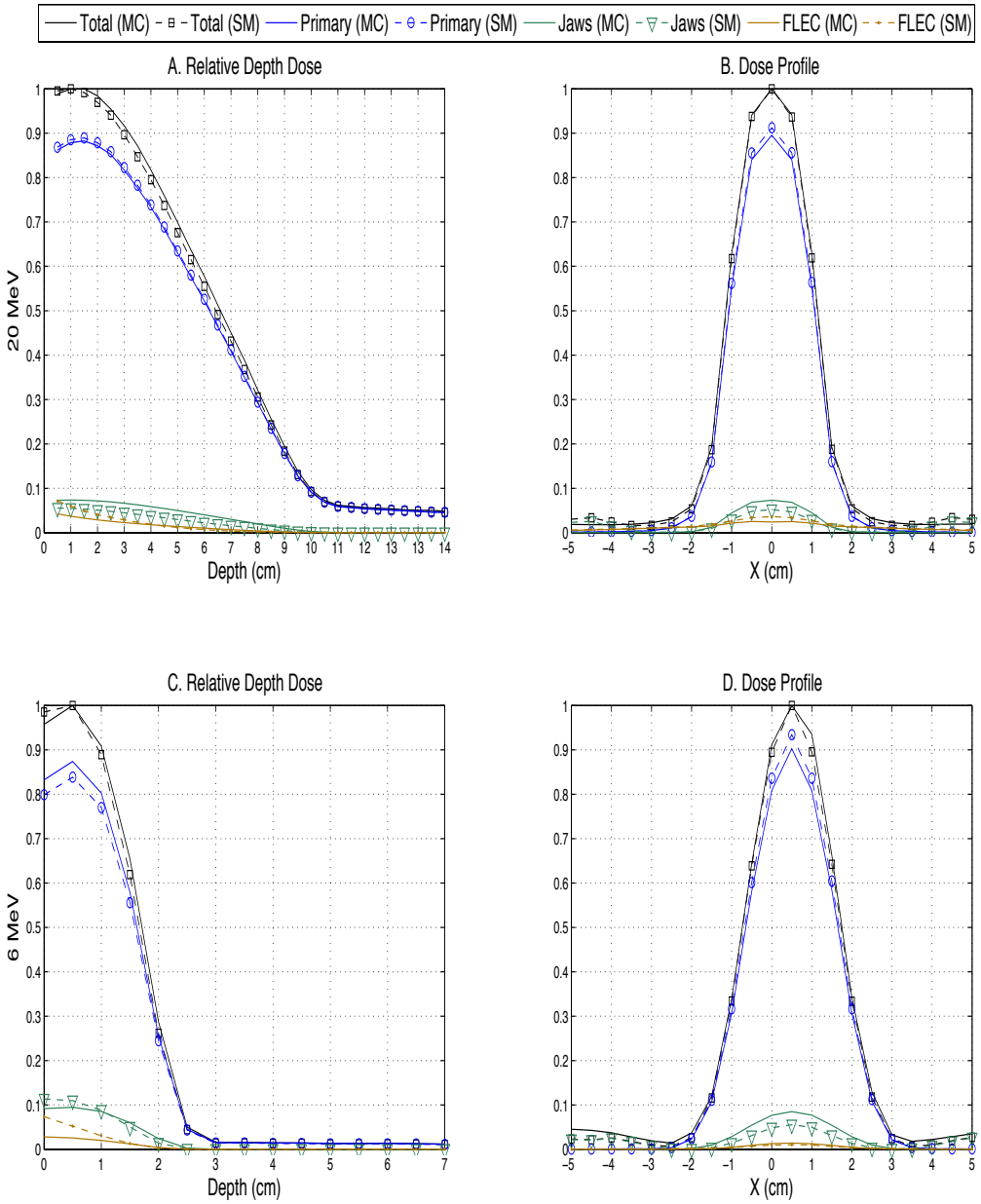

Figure 3.7: *Depth and profile dose distributions for a field size of* 2×8 cm^2 *and energies of 20 MeV (A and B) and 6 MeV (C and D). Solid lines represent the full MC simulation results, while dotted lines/symbols represent the source model predictions.*

Dose output = $D_{max}(field \quad size)/D_{max}(8 \times 8 \quad cm^2)$

	$8 \times 8 \quad cm^2$		$2 \times 2 \quad cm^2$		$2 \times 8 \quad cm^2$	
Energy (MeV)	MC	SM	MC	SM	MC	SM
20	1	1	0.603	0.629	0.796	0.794
6	1	1	0.151	0.144	0.404	0.392

Table 3.4: *Dose output at z_{max} as predicted by the full MC simulation and by the source model for field sizes of 8×8 cm^2, 2×2 cm^2, 2×8 cm^2 and energies of 20 MeV and 6 MeV. The output is normalized to the maximum dose of the 8×8 cm^2 field size for each energy and for each model independently.*

3.1.5 Dose output

Table 3.4 exhibits the dose output at the depth of maximum dose (z_{max}) as predicted by the beam model and by the full MC simulation for field sizes of 8×8 cm^2, 2×2 cm^2 and 2×8 cm^2. The 8×8 cm^2 field size was set as the reference field size for the dose output normalization for each energy. Thus, the dose output was calculated according to the following formula:

$$Output = \frac{D_{max}(field \quad size)}{D_{max}(8 \times 8 \quad cm^2)}$$

From the results the following can be deduced:

- For 20 MeV and 2×2 cm^2 the dose output is *overestimated* by the source model by 4.3%
- For 20 MeV and 2×8 cm^2 the dose output is *underestimated* by the source model by 0.25%
- For 6 MeV and 2×2 cm^2 the dose output is *underestimated* by the source model by 4.6%
- For 6 MeV and 2×8 cm^2 the dose output is *underestimated* by the source model by 2.9%

The discrepancies were enhanced as the field size or the energy was reduced. The agreement between the source model and the full MC was within 5% in all cases. For the rectangular field size of 2×8 cm^2 the agreement was within 3%.

In chapter 4 the performance of the source model, as presented by the results in this section, will be analyzed and discussed. Furthermore, potential sources of errors will be identified to explain the discrepancies that were encountered and future work will be proposed.

3.2 Automated motion control

3.2.1 General

In section 2.2 two approaches were presented for implementation of a radiation tolerant position feedback system for the FLEC: (i) shielding the optical encoders and (ii) using potentiometers as an analog feedback device. For the first approach, a prototype Cu shield was manufactured which could be placed on top of the FLEC and provide face and side protection of the encoder's site (figure 2.14) . The shielding material and thickness were determined by detailed Monte Carlo simulations. The second approach suggested the replacement of the optical encoders by an analog position feedback device, such as a potentiometer. Potentiometers are known to withstand higher radiation dose than the optical encoders (Table 1.1). In this section the results of the investigation for the two approaches will be presented.

3.2.2 Measurements at the encoder site

Measurements were performed with a Farmer type ionization chamber placed at the encoder's site with and without the shield. For the measurements, the electron beam energy was set to 16 MeV, the field size at 8×8 cm^2 and the dose rate to 400 MU/min. The measurements were performed by giving 2200 MUs each time. A polyethylene base was used for the measurements to mimic the FLEC's dimensions. Table 3.5 exhibits the results of the experiment. The dose received at the encoders site was reduced to 5.4% of the unshielded dose, from 19.7 Gy (no shield) to 1.07 Gy (with shield). Figure 3.8 shows the experimental setup for the measurements.

At the next step an Al cap (radius=1.2 cm) was placed on the ion chamber to cut-off the electron component of the beam. The measurements were repeated with the same settings

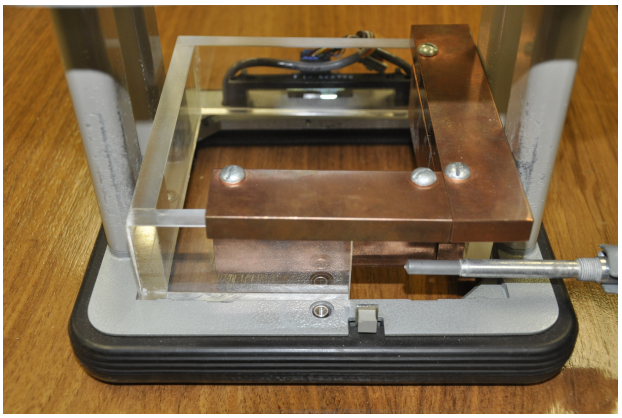

Figure 3.8: *Experimental setup for dose measurements at the encoders site with a prototype Cu shield.*

	No shield	With shield	With Al cap	With Pb cap
Dose (Gy)	19.7	1.07	1.02	0.3

Table 3.5: *Total dose received at the encoder site with and without the shield for 2200 MUs and dose rate of 400 MU/min.The dose received with the use of an Al cap and a Pb cap on the chamber is also presented*

and the Cu shield in place. The measured dose was found to be 1.02 Gy, only 4.7% lower than the measurements without the Al cap. The result indicates that the majority of the dose to the encoders site, when the Cu shield is used, can be attributed to the photon beam component. The electron beam component was succesfully removed from the beam with the use of the Cu shield. Figure 3.9 shows the experimental setup for the measurements with the Al cap.

A Pb cap (radius=2 cm) was then manufactured to remove the residual photon component of the beam. The method can now be seen as as a *dual shielding* system: first, the Cu shield would cut-off the majority of incident electrons and then the Pb shield would cut-off the remaining photons. The experiment can be conceived as our limit practical case to protect the encoders on their site. The measured dose was found to be 0.3 Gy, a reduction by 72% compared to the dose received with only the Cu shield present.

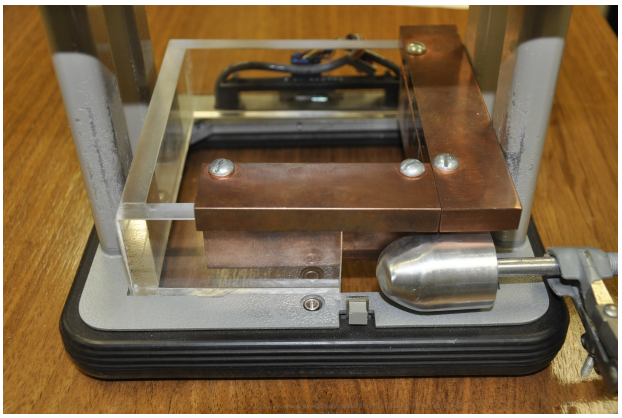

Figure 3.9: *Al cap used on top of the ion chamber to isolate the photon from the electron component*

3.2.3 Analog position feedback for the FLEC

In section 2.2.3, a simple analog position feedback system was presented. In this section a prototype of the system will be presented and its performance will be evaluated. Figure 3.10 shows the prototype electronic circuit setup for the position feedback device.

In the setup, the potentiometer can be seen directly connected to the rotation axis. The reference voltage was set at 10 V, thus allowing a voltage range from 0-10 V. For a 12-bit Analog-to-Digital Converter there are 4096 available discrete steps, thus 4096/10V=409 steps/volt. Each axis revolution was set to correspond to a voltage drop of 1 V. To calibrate the system, the stepper steps per revolution had to be found first. To achieve that, the motor was turned manually until a drop of 1 V was observed. The stepper steps corresponding to the movement were monitored by the controller's software, while at the same time the output voltage change was monitored independently with a voltmeter. The procedure was

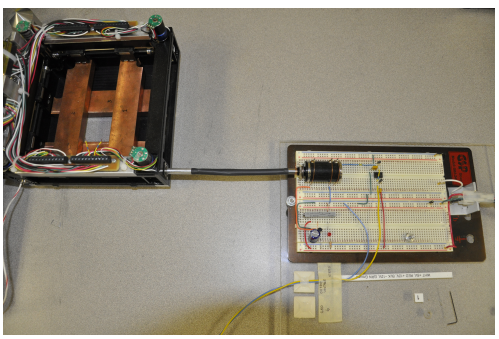

Figure 3.10: *Prototype electronic circuit setup for the analog position feedback system to be used with the FLEC.*

Voltage (V)	ΔV (V)	Stepper motor steps	ADC steps	$\Delta(ADC)$
	0.28		114	
0.987	1.27	616	513	399
1.01	2.28	632	921	408
1.01	3.29	633	1331	410
1.01	4.31	633	1740	409
1.01	5.32	638	2152	412
1.02	6.34	638	2564	412
1.01	7.35	635	2974	410
1.02	8.37	637	3385	411
1.01	9.38	637	3797	412

Table 3.6: *Analog position feedback performance*

repeated for the full range of available voltages. It was found that 635 motor stepper steps correspond to 1 V change in all cases. This value was then set in the controller's software as the stepper steps/revolution input.

At the next step the system's performance in reading the voltage drop and translating it to the correct number of ADC steps was evaluated. Ideally, the procedure should be performed as follows:

1. The ADC steps/revolution are set to 409 steps/revolution.
2. The user asks for 635 motor steps from the controller (corresponding to 1 axis revolution). The controller sends a signal to the stepper motor to perform 635 steps.
3. The axis starts to rotate and the potentiometer starts sending an output voltage back to the controller.
4. The controller reads the voltage change and the Analog-to-Digital Converter translates it to a number of discrete steps.
5. If 409 discrete steps have been performed the controller orders to stop the move.

The above procedure was tested experimentally in order to verify if the controller actually stops the movement at the correct number of ADC steps. The ADC steps were

monitored directly from the controller, rather than through the software, to validate independently the system's performance. Table 3.6 exhibits the results of the investigation.

For 635 stepper steps asked, the average voltage change by the potentiometer was 1.01 V (standard deviation = 0.0098V), while the average number of ADC steps read directly from the controller were 409.2 (standard deviation = 4.08). This corresponds to an accuracy of 1% which will result to a leaf movement error of approximately 0.01 mm.

In chapter 4, the performance of the shielding prototype and the analog position feedback system will be analyzed and future work will be discussed.

Chapter 4

Conclusions

4.1 Beam model

In chapter 2, a method was proposed for a parameterized, MC-based beam model for modulated electron radiation therapy deliveries. In chapter 3, the beam model was tested and compared with full Monte Carlo (MC) simulations for the largest (8×8 cm^2) and smallest field size (2×2 cm^2), as well as for a rectangular field size (2×8 cm^2) and for the highest (20 MeV) and lowest (6 MeV) nominal electron beam energy. From the results the following conclusions can be made:

- The fast primary beam models (presented in section 2.1.4 and 3.1.2) exhibited excellent agreement in all cases with the full MC simulations. The fastest model was *fast model 3* (PRESTA I & SD=0) for which the following parameters were changed:

    1. ECUT value was set higher than the maximum electron beam energy in the collimating components. Thus, all the electrons reaching a non-air region were immediately rejected.
    2. Boundary Crossing Algorithm (BCA) was changed from EXACT to PRESTA-I.
    3. Skin Depth for BCA was changed from 3 mfp to 0 mfp.

    The above changes did not result in any discrepancies compared to the full MC simulations (mean error less than 0.5%) of the primary component, while they increased the calculation speed in some cases by more than 22 times. Since the primary beam consists of particles transporting only through air, switching the BCA to the default

PRESTA behavior when an electron reaches a boundary, does not affect significantly the end result, namely the depth and profile dose distributions. However, it should be noted that the above conclusion applies only in the case of the primary beam. For the scattered beam it is crucial to maintain the EXACT BCA algorithm, since the beam characteristics would otherwise be signifcantly changed.

The primary beam component is the main component of the electron beam with a relative intensity of greater than 75% of the total beam in some cases. Therefore, truthfully maintaining the primary beam characteristics is crucial for the derivation of an accurate electron beam model. This has been reported in previous work on electron beam modeling [43, 49], where discrepancies in the total beam distributions were mainly attributed to the lack of predicting with good accuracy the primary beam component. Having established a high level of confidence for the primary beam, any discrepancies encountered in the total beam distributions can now be attributed to the scatter beam sources and studied independently.

- The method for deriving the scatter beam component was presented in sections 2.1.5 and 3.1.3. From the results the following can be deduced:

    1. The fluence output (see Table 3.2) was heavily *overestimated* if no correction were to be applied to the algorithm. This is due to the fact that the scatter source kernels were derived for each leaf component independently, while the rest of the leaves were not present. Applying a correction to account for the missed leaf hits improved the results significantly. However, even after the leaf-hit correction, discrepancies were observed especially for the smallest field size. For the case of a field size of 2×2 cm^2 and an energy of 6 MeV the fluence output was overestimated by more than 4 times. The discrepancies can be attributed to the following approximations: (i) electron multiple scattering in air was not included in the model, (ii) the presence of the Al frame was neglected and (iii) Gaussian sampling of the particle's original position on each leaf. The effect of multiple scattering in air should be considered as the most important contributing factor to the above discrepancies, since the largest discrepancies were encountered for the lowest energies (where the mass angular scattering power is higher).

2. The normalized scatter fluence distributions showed good agreement in the treatment field, but discrepancies were encountered in the penumbra region. The discrepancies can be attributed again to the lack of a correction for multiple scattering in air (since some directions were not rejected) and the absence of the Al frame in the model (which resides outside the treatment field). Nevertheless, the fluence outside the treatment field is low, thus these discrepancies are not expected to significantly affect the dose distributions.

3. The relative intensities of the sub-sources were altered by the beam model compared to the MC calculated. For example, if we consider the ratio $\frac{Output(JAWS)}{Output(FLEC)}$ (from table 3.2) for an energy of 6 MeV and field size of 2×2 cm^2, the full MC simulation predicts a value of 2.4, while the beam model predicts a value of 0.85. For an energy of 6 MeV and field size of 8×8 cm^2 the predicted relative intensities were 0.51 and 0.49 respectively. Thus, the leaf-hit correction algorithm does not correct the *output fluence* in the same manner for the different sub-sources as the field size *decreases*.

4. The mean particle energy as predicted by the beam model showed good agreement with the full MC simulation in most of the cases (Table 3.3). For a field size of 8×8 cm^2 an *underestimation* of the mean energy by 1.3 MeV is observed for the sub-source JAWS, for the energy of 20 MeV. This implies that the leaf-hit correction algorithm does not reject the correct number of particles in the low energy region. This effect can again be attributed to the lack of a multiple scattering correction.

- The final dose distributions as predicted by the beam model and by the full MC simulations are shown in graphs 3.5, 3.6 and 3.7 for field sizes of 8×8 cm^2, 2×2 cm^2 and 2×8 cm^2 respectively. The following conclusions can be made:

  1. The largest field size (8×8 cm^2) exhibited excellent agreement for all energies with a maximum error in a voxel being less than 2.5% in all cases. The only discrepancy encountered was an underestimation of the dose from the sub-source JAWS in deeper regions. This effect can be attributed to an underestimation of the mean energy for the sub-source JAWS for the field size of 8×8 cm^2 by the

beam model. The surface doses are well predicted for all energies, a result that agrees with the relative good prediction of the sub-sources relative intensities for this field size, as it was described previously.

2. The smallest field size (2×2 cm^2) exhibited discrepancies for the sub-source JAWS and FLEC with a maximum error of 6%. The FLEC dose distribution was significantly *overestimated* in the build-up region for 6 MeV. This effect can be attributed to the significant overestimation (more than 4 times) of the scatter output fluence by the beam model for the energy of 6 MeV for the FLEC, as it can be seen in table 3.2. This results to an erroneous prediction of the relative sub-sources intensities, as it was described previously.

   A possible explanation of the significant discrepancies appearing for the small field size and for the FLEC could be the following: during the derivation of each FLEC-source scatter kernels, only the corresponding jaw leaf was present. This have allowed particles, that would have otherwise been stopped earlier at another jaw leaf, to erroneously be incident on the FLEC leaf. If the *incident* beam on a FLEC leaf is *inaccurate* then the *scattered* particles from it will also be *inaccurate*. As the field size decreases, the jaw and FLEC leaves approach closer to each other and closer to the central axis as well, thus the effect is expected to be more significant. It should be noted that this effect *is not* accounted for in the leaf-hit correction algorithm, since after a particle is generated from a source, its previous history is completely unknown.

3. The irregular, rectangular field size of 2×8 cm^2 exhibited similar behavior with the field size of 2×2 cm^2, but the discrepancies were less severe. Thus, the limitations of the beam model seem to be focused mainly on the *field size* than the *field shape*.

- The overall dose output as predicted by the beam model showed reasonable agreement within 5% in all cases. The main discrepancies were exhibited again for the smallest field size (2×2 cm^2) and can be attributed to the problems that the leaf-hit correction algorithm has shown in correcting accurately the fluence output for small fields. For a rectangular field size of 2×8 cm^2, the dose output shows very good agreement,

even for the lowest energy, within 3%.

Overall, the *parameterized, MC-based beam model* presented in this work showed very good agreement with full MC simulations, both in the relative dose distributions and dose output for relative large field sizes (8×8 cm^2 and 2×8 cm^2) for the highest and lowest energy. This proves that the methodology applied in this work is promising and is a step in the correct direction towards the implementation of a fast and accurate beam model for modulated electron beam deliveries. Discrepancies were encountered almost exclusively for the smallest field size (2×2 cm^2), that were enhanced in the case of low energies. The main sources of errors that were identified can be mainly attributed to the following two approximations:

- *The straight line approximation* between original position on each leaf and final position on the exit plane for deriving the particle's direction. Leaf-hit correction algorithm corrected the fluence output based on this simplistic estimation of direction to account for particles that would have been stopped at a leaf. *Multiple scattering* in air was ignored at this step.

- *The incident beam* on each FLEC leaf was not an accurate representation of the real incident beam, since not all of the leaves were present during the derivation of the scatter source kernels. This resulted to an *overestimation* of the scatter fluence output by the beam model, which could not be accounted for by the leaf-hit correction algorithm.

The beam model presented a significant time gain compared to performing a full Monte Carlo simulation for each field size and energy. Deriving the primary beam component showed a time gain up to almost 23 times faster than the full MC. The scatter beam component could be derived in almost negligible amount of time. For 10^9 histories asked by the user (that would provide an accuracy of 1% or better to the dose distributions in all cases) the scatter beam component calculation time for all the sub-sources was less than 5 min. The calculation time can be further improved by applying parallel computing techniques or re-writing the code in a faster programming language. However, even with the current implementation, the calculation time was considered adequately fast, thus there was no need for making these changes at this point.

Future work

Future work will be focused in improving the two main sources of errors identified previously: The direction estimation should be significantly improved if the electron multiple scattering effect is included. This correction will at the same time improve the accuracy of the leaf hit correction algorithm. The Fermi-Eyges scattering theory could be applied for that purpose, which has shown to reproduce accurately the electron angular distribution in previous work in electron beam modeling [47]. The incident beam on the FLEC leaves could reach closer to a truthful representation, if there was a *leaf-hit tag* for each particle. The leaf-hit tag would basically be the position of a particle when it was still at the level of the jaws. During reconstruction the particle will be rejected if the leaf-hit tag indicates that this particle *should not* have been incident on the FLEC in the first place.

4.2 Automated motion control

In section 2.2, two approaches were presented for implementing a radiation tolerant position feedback device to be used with the FLEC: (i) using CMOS-based optical encoders with a protective Cu shield and (ii) replacing the optical encoders with an analog position feedback system. In section 3.2, the results of the investigation were presented for both approaches. From the results the following conclusions can be made:

- The use of a protective Cu shield reduced significantly the dose to the encoder site, but not enough to suggest a permanent and safe solution for treatment deliveries. Specifically, for 2200 MUs and and a dose rate of 400 MU/min, the dose to the optical encoder site was reduced from 19.7 Gy to 1.07 Gy. Based on the estimated dose limit values presented in table 1.1, non-hardened optical encoders can withstand doses up to approximately 1 kGy. Thus, the presented Cu shield would only protect the encoders for a limited number of treatments. As it was identified by the measurements with the Al cap, the majority of this dose results from photons rather than the electrons. To this effect the Cu shield probably contributes itself to the problem by the production of Bremsstrahlung photons as the electron beam is incident on the shield. The use of a high Z material (such as Pb) could possibly help reducing the photon component,

but the required thickness to achieve a noticeable reduction to the dose would exceed the space (and possibly weight) limitations of the device.

- The use of an analog position feedback device such as a potentiometer was investigated as an alternative. A prototype electronic circuit was designed and it's performance was tested in section 3.2.3. It was shown that the system performed with adequate accuracy in the full voltage range. Potentiometers are known to withstand at least two orders of magnitude higher doses than optical encoders (see Table 1.1). However, the main drawback of any analog system is the increased level of noise. From the investigation performed for this study, the spatial resolution of the prototype analog feedback system was found to be 0.01 mm. The result indicates that noise is not going to reduce significantly the performance of the system. It should be noted, however, that the performance of such a system might degrade with time and increased usage as well. Therefore, further investigation should be performed before introducing such a position feedback system in the clinic.

Future work

Future work will be focused in the implementation of a permanent analog position feedback system using potentiometers for FLEC-based MERT deliveries. The system has to be implemented in a compact size to fit the FLEC frame. Mechanical issues have to be also resolved, such as determining the grid ratio between the rotation axis and the potentiometer. Furthermore, the system has to be tested under radiation to establish its dose tolerance limit and consequently its life span. Possible increase in noise with usage has to be reported.

Bibliography

[1] E. B. Podgorsak (Technical editor), *Radiation Oncology Physics: A handbook for teachers and students*, Vienna, International Atomic Energy Agency, ISBN 92-0-107304-6 (2005).

[2] B. Rossi and K. Greisen, *Cosmic-ray theory*, Rev. Mod. Phys. **13**, 240 (1940); Fermi's work is given on pp. 265-268.

[3] L. Eyges, *Multiple scattering with energy loss*, Phys. Rev. **74**, 1534 (1948).

[4] K.R.Hogstrom, M.D. Mills and P.R. Almond, *Electron beam dose calculations*, Phys. Med. Biol. **26**, 445-459 (1981).

[5] J. Cygler, J.J. Battista, J. W. Scrimger, E. Mah and J. Antolak, *Electron dose distributions in experimental phantoms: a comparison with 2D pencil beam calculations*, Phys. Med. Biol. **32**, 1073-1086 (1987).

[6] M.J. Berger, *Monte Carlo calculation of the penetration and diffusion of fast charged particles*, Methods Comput. Phys. **1**, 135-215 (1963).

[7] D.W.O. Rogers and A.F. Bielajew, *The Dosimetry of Ionizing Radiation: Monte Carlo techniques of electron and photon transport for radiation dosimetry*, chap **5**, Vol. **3**, National Research Council of Canada, Ottawa, Canada (1990).

[8] D.W.O. Rogers, B.A. Faddegon, G. X. Ding, C.-M. Ma, J. S. Wei, *BEAM: A Monte Carlo code to simulated radiotherapy treatment units*, Phys. Med. Biol. **22**, 503-525 (1995).

[9] S. Agostinelli, *GEANT4–A simulation toolkit*, Nucl. Instrum. Methods Phys. Res. A **506**. 250-303 (2003).

[10] B.R.B. Walters and D.W.O. Rogers, *DOSXYZnrc User's Manual*, NRC Report PIRS **794**, (rev B) (2004).

[11] I. Kawrakow, M. Fippel and K. Friedrich , *3D electron dose calculation using a voxel based Monte Carlo algorithm (VMC)*, Med. Phys. **23**, 445-57 (1996).

[12] H. Neuenschwander and E. J. Born, *A macro Monte Carlo method for electron beam dose calculations*, Phys. Med. Biol. **37**, 107-25 (1992).

[13] E. Hall and C-S Wuu, *Radiation-induced second cancers: the impact of 3D-CRT and IMRT*, Int. J. Radiation Oncology Biol. Phys **56**, No 1, pp 83-88 (2003).

[14] K.R.Hogstrom,John A. Antolak,R.J. Kudchadker, C-M Ma, Dennis D. Leavitt, *Modulated electron therapy*, AAPM Summer school, (2003).

[15] E. R. Jr. Bawiec, *The effects of Accuracy in Milling of Electron Bolus on Dose Delivery*,The University of Texas Health Science Center at Houston (M.Sc. thesis)(1994).

[16] E. E. Klein, *Modulated electron beams using multi-segmented multileaf collimation* Radiother. Oncol. **48**, 307-311 (1998).

[17] M. Karlsson, H. Nystrom and H. Svensson, *Electron beam characteristics of the 50-MeV racetrack microtron* Med. Phys. **19**,No 2,(1992).

[18] M. G. Karlsson, M. Karlsson and B. Zackrisson, *Intensity modulation with electrons: calculations, measurements and clinical applications* Phys. Med. Biol. **43**. 1159-1169 (1999)

[19] M. G. Karlsson, M. Karlsson and C-M Ma, *Treatment head design for multileaf collimated high energy electrons* Med. Phys. **26**, No 10, (Oct 1999)

[20] E. E. Klein, M. Mamalui-Hunter and D. A. Low, *Delivery of modulated electron beams with conventional photon multi-leaf collimators* Phys. Med. Biol. **54**. 327-339 (2009)

[21] F. J. Salguero, R. Arrans, B. A. Palma and A. Leal1, *Intensity- and energy-modulated electron radiotherapy by means of an xMLC for head and neck shallow tumors* Phys. Med. Biol. **55**. 1413-1427 (2010)

[22] F. J. Salguero, B. Palma, R. Arrans, J. Rosello, *Modulated electron radiotherapy treatment planning using a photon multileaf collimator for post-mastectomized chest walls* Radiother. Oncol. **93**, No 3,625-632 (2009)

[23] F. C. du Plessis, *Characterization of megavoltage electron beams delivered through a photon multi-leaf collimator* Phys. Med. Biol. **51**, 2113-29 (2006)

[24] M.C. Lee, S. Jiang and C-M Ma, *Monte Carlo and experimental investigations of multileaf collimated electron beams for modulated electron radiation therapy* Med. Phys. **27**, No 12 (Dec 2000)

[25] D. D. Leavitt, J. R. Stewart, J. H. Moeller, W. L. Lee and G. H. Takach, *Electron arc therapy: design, implementation and evaluation of a dynamic multi-vane collimator system*, Int. J. Radiat. Oncol. Biol. Phys. **17** 1089-1094 (1989)

[26] C. M. Ma, T. Pawlicki, M. Lee, S. Jiang, J. Li, J. Deng, B. Yi, E. Mok and A. L. Boyer, *Energy- and intensity-modulated electron beams for radiotherapy* Phys. Med. Biol. **45** 2293-2311 (2000)

[27] B. P. Ravidran, I. R. R. Singh, S. Brinda and S. Sathyan, *Manual multi-leaf collimator for electron beam shaping-a feasibility study* Phys. Med. Biol. **47** 4389-4396 (2002)

[28] T. Gauer, D. Albers, F. Cremers, R. Harmansa, R. Pellegrini and R. Schmidt, *Design of a computer-controlled multileaf collimator for advanced electron radiotherapy* Phys. Med. Biol. **51** 5987-6003 (2006)

[29] K R. Hogstrom, R A. Boyd, J A. Antolak, M. M. Svatos, B. A. Faddegon, J. G. Rosenman, *Dosimetry of a prototype retractable eMLC for fixed-beam electron therapy* Med. Phys. **31** 5987-6003 (2004)

[30] M. Nassiri, H. Bouchard, S. Mercure and J. Carrier *Motorized multi-leaf collimator for electrons: measurements with a prototype and Monte Carlo simulations* Med. Phys. **34** 2627 (2007)

[31] L. Jin, C. Ma, A. Eldib, I. Fan, T. Lin and J. Li *Characteristics of electron beams collimated by an electron multileaf collimator* Med. Phys. **34** 2643 (2007)

[32] A. A. R. Eldib, M. I. ELGohary, J. Fan, L. Jin, J. Li, C. Ma, N. A. Elsherbini *Dosimetric characteristics of an electron multileaf collimator for modulated electron radiation therapy*Appl. Clin. Med. Phys., Vol 11, No 2 (2010)

[33] T. Vatanen, E. Traneus and T. Lahtinen *A new add-on electron multi-leaf collimator (eMLC): dosimetry and dose calculation using a new beam model with Voxel Monte Carlo* Radioth. Oncol. 81 S166 (2006)

[34] T. Gauer, J. Sokoll, F. Cremers, R. Harmansa, M. Luzzara and R. Schmidt, *Characterization of an add-on multileaf collimator for electron beam therapy* Phys. Med. Biol. **53**, No 3, 443 (2008)

[35] K. Al Yahya, D. Hristov, F. Verhaegen and J. Seuntjens, *Monte Carlo based modulated electron beam treatment planning using a few-leaf electron collimator–feasibility study* Phys. Med. Biol. **50** 847-857 (2005)

[36] K. Al Yahya, M. Schwartz, G. Shenouda, F. Verhaegen and J. Seuntjens, *Energy modulated electron therapy using a few leaf electron collimator in combination with IMRT and 3D-CRT: Monte Carlo-based planning and dosimetric evaluation* Med. Phys. **32** 2976-2986 (2005)

[37] K. Al Yahya, F. Verhaegen and J. Seuntjens, *Design and dosimetry of a few leaf electron collimator* Med. Phys. **34** 4782-4791 (2007)

[38] A. Alexander, F. Deblois, G. Stroian, K. Al Yahya, E. Heath and J. Seuntjens, *MMCTP: a radiotherapy research environment for Monte Carlo and patient-specific treatment planning* Phys. Med. Biol. **52** N297-308 (2007)

[39] A. Alexander, F. Deblois and J. Seuntjens, *Toward automatic field selection and planning using Monte Carlo-based direct aperture optimization in modulated electron radiotherapy* Phys. Med. Biol. **55** 4563-4576 (2010)

[40] M. Decreton, *Position sensing in nuclear remote operation* Measurement **15** 43-51 (1995)

[41] J.B. Burr, Z. Chen and B.M. Bass, *Stanford's Ultra-Low-Power CMOS Technology and Applications - Chap. 3 in Low Power HF Microelectronics: A Unified Approach*, (EDITOR) G.A.S. Machado, Instit. Elect. Eng., UK, (1996).

[42] I. Chetty, B. Curran, J. Cygler, J. DeMarco, G. Ezzell, B. Faddegon, I. Kawrakow, P. J. Keall, H. Liu, C-M C Ma, D.W.O Rogers, J. Seuntjens, D. S. Bagheri, J. Siebers, *Report of the AAPM Task Group No 105: Issues associated with clinical implementation of Monte Carlo-based photon and electron external beam treatment planning*, Med. Phys. **34**,Issue 12 (2007)

[43] M. A. Ebert and P. W. Hoban, *A Monte Carlo investigation of electron beam applicator scatter*, Med. Phys. **22**, 1431-35 (1995)

[44] M. A. Ebert and P. W. Hoban, *A model for electron-beam applicator scatter*, Med. Phys. **22**, 1419-29 (1995)

[45] C-M Ma, B. A. Faddegon, D.W.O. Rogers and T.R. Mackie, *Accurate characterization of Monte Carlo calculated electron beams for radiotherapy*, Med. Phys. **24**, 401-416 (1997)

[46] C-M Ma and D.W.O. Rogers, *BEAM characterization: A Multiple-Source Model*, NRC Report PIRS-0509(C) (1995)

[47] S. B. Jiang, J. Deng, J. Li, P. Pawlicki, A. Boyer and C-M Ma, *Electron beam modeling for Monte Carlo treatment planning*, Med. Phys. **27**, 2739-2747 (2000)

[48] J. J. Jansen, E. W. Korevaar, L. J. Van Battum, P.R. Storchi, and H. Huizenga, *A model to determine the initial phase space of a clinical electron beam from measured beam data*, Phys. Med. Biol. **46**, 269-286 (2001)

[49] T. Vatanen, E. Traneus and T. Lahtinen, *Dosimetric verification of a Monte Carlo electron beam model for an add-on eMLC*, Phys. Med. Biol. **53**, 391-404 (2008)